Quantum Simulation of Strongly Correlated Phases in Low-Dimensional Solid-State Systems

Doctoral Thesis

Author: **Weronika Pasek**
Supervisor: **Dr hab. Paweł Potasz**
Auxiliary supervisor: **Dr hab. Michał Zieliński**

A thesis presented for the degree of
Doctor of Philosophy

Faculty of Physics, Astronomy and Informatics
Nicolaus Copernicus University in Toruń
Poland
September 30, 2025

To my beloved family and cats,
my companions and support.

Acknowledgments

I would like to express my sincere gratitude to my supervisor, Prof. Paweł Potasz, and my auxiliary supervisor, Dr. Michał Zieliński, for their guidance and support throughout this work. I am also grateful for the fruitful collaborations during my PhD studies, especially with Prof. Moritz Cygorek, Prof. Marek Korkusinski, Dr. Michał Kupczyński, and Dr. Yasser Saleem. The numerical calculations were partially performed at the Wrocław Center for Networking and Supercomputing.

Abstract

Understanding strongly correlated quantum phases remains a central challenge in condensed matter physics, as many exotic states, like superconductors, spin liquids, and topological effects, emerge from interactions beyond the reach of perturbative methods. This thesis explores solid-state quantum simulators as an alternative platform for investigating such phases, providing strong electronic correlations, high tunability, and direct access to spin Hamiltonians.

We first analyze moiré transition metal dichalcogenides heterostructures, where the effective moiré potential results in arrays of localized quantum dots with interactions controlled by the relative twist between monolayers and the dielectric environment. Using exact diagonalization and effective Hubbard modeling, we show that these systems host a rich set of correlated ground states, including generalized Wigner crystals and signatures of spin polarization driven by the Nagaoka mechanism. By projecting onto the single-occupied, low-energy spectrum, we obtain an effective spin model with ring exchange interaction, which, for moderate dielectric screening, favors a quantum spin liquid. A nematic valence bond solid is favored for stronger screening as a ground state.

In the second part, we focus on graphene nanostructures as building blocks for quantum spin chains. We design mixed-size nanographene chains that realize the Haldane phase with short correlation length by combining spin-1 triangulene units with spin-$\frac{1}{2}$ phenalenyls. Density matrix renormalization group simulations reveal a finite Haldane gap, localized edge states, nonlocal string order, and an entanglement spectrum with even degeneracies characteristic of symmetry-protected topological order. By tuning the number of spin-$\frac{1}{2}$ buffer sites, the correlation length can be continuously adjusted toward the Affleck–Kennedy–Lieb–Tasaki limit, offering a route to engineer short-range topological phases.

These results establish moiré heterostructures and nanographene chains as versatile solid-state quantum simulators of correlated and topological matter. They highlight the potential of nanoscale electronic systems to complement ultracold atom platforms, extending quantum simulation into regimes of strong interactions and experimentally accessible energy scales.

Contents

List of Figures

List of Tables

List of Acronyms

SPT Symmetry Protected Topology
VBS Valence Bond Solid
BLBQ Bilinear Biquadratic Hamiltonian
TEFR Tensor Entanglement Filter- ing Renormalization Group
AKLT Affleck-Kennedy-Tasaki-Lieb
FCI Fractional Chern Insulator
FQHE Fractional Quantum Hall Effect
QGT Quantum Geometry Tensor
BCS Bardeen-Cooper-Schrieffer
MATTG Magic- Angle Twisted Trilayer Graphene
MATBG Magic- Angle Twisted Bilayer Graphene
QSL Quantum Spin Liquid
QMC Quantum Monte Carlo
TMD Transition Metal Dichalcogenides
TBG Twisted Bilayer Graphene
hBN hexagonal Boron Nitride
DFT Density Functional Theory
TGQD Triangular Graphene Quantum Dot
STM Scanning Tunneling Microscope
LDOS Local Density of Electronic States
ED Exact Diagonalization
DMRG Density Matrix Rnormalization Group
RSRG Real-space Renormalization Group
MPS Matrix Product State
MPO Matrix Product Operator
SVD Singular Value Decomposition
TEBD Time-evolving Block Decimation
RVB Resonating Valence Bond

DQCP Deconfined Quantum Critical Point
HF Hartree-Fock
CI Configuration Interaction
CAS Complete Active Space
SOP String Order Parameter

Chapter 1

Introduction I: Strongly correlated phases of matter

In common metals, the kinetic energy of mobile electrons far exceeds their mutual Coulomb interaction. As a result, it is appropriate to use perturbation theory, treating electron-electron interactions as small perturbations within a single-particle model [4, 5]. However, in systems where Coulomb interactions dominate over kinetic energy, the perturbative approach fails to capture the essential phenomena. These systems, where interactions are strong enough to affect the behavior of electrons significantly, are known as strongly correlated systems [6–8].

One of the earliest realizations of correlation-driven phenomena was the Mott insulator, where electron-electron interaction may prevent conductivity despite partially filled energy bands [9–11]. Then, this discovery was followed by the formulation of the Hubbard model [12] and the Anderson impurity model [13], which introduced settings for localization, magnetism, and charge fluctuations [14–16].

Another step in the development of strongly correlated systems was the experimental observation of the Kondo effect, which revealed an unexpected resistance minimum at low temperatures in metals with dilute magnetic impurities [17]. This anomaly was explained by Kondo, and then the extension of his idea to periodic arrays of impurities gave rise to the concept of heavy fermions [18]. The central role of strong correlations in condensed matter physics was consolidated by the discoveries of unconventional superconductors and quantum spin liquids [19–25]. In 1980, Laughlin proposed the concept of spin-charge separation and fractional quasiparticles in correlated

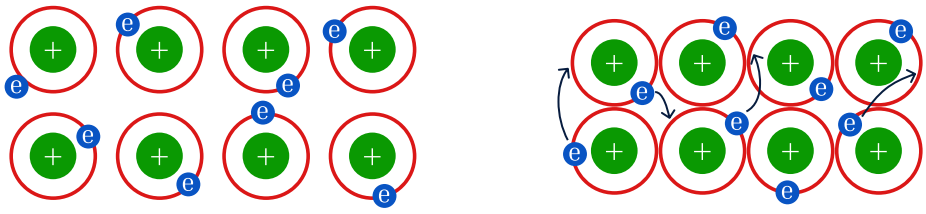

Figure 1.1: Schematic representation of the Mott insulator and metallic phase.

phases [26]. At the same time, Haldane's conjecture on spin chains revealed topological distinctions between integer and half-integer spin systems [27]. In recent decades, new experimental platforms such as ultracold atoms in optical lattices and moiré materials have allowed one experimental realizations of strongly correlated phases described by various Hamiltonians [28,29]. The quantum simulators enable direct exploration of Mott transition, quantum magnetism, or topological effects in engineered settings.

In the following sections, we will discuss some examples of strongly correlated phases of matter, like Mott insulators, superconductivity, and spin liquids.

1.1 Mott insulators

The hallmark of strongly correlated electron systems is the Mott insulating phase. This phenomenon occurs in specific groups of materials, which behave as insulators despite having a partially filled energy band. In general, the analysis of the band structures allows researchers to explain many electronic properties of crystals. Still, such a description does not include electronic interactions, which are crucial for strongly correlated systems. According to the Bloch theorem, the partial filling of the band should lead to metallic conductivity. However, it may not be true when a strong Coulomb repulsive interaction is considered.

Historically, this effect was first reported in 1937 by Jan Hendrik de Boer and Evert Johannes Willem Verwey [9], who pointed out that many transition metal oxides are insulators, even if their d-bands are partially filled by electrons. The problem was then considered by Nevill Mott and Rudolf

Peierls, who predicted that such a phenomenon could be explained by including interaction between electrons in band models [10].

In his later work, Mott analyzed the case of nickel(II) oxide (NiO), which consists of Ni^{++} and O^{--} ions [30]. As Mott pointed out, for NiO to be conductive, it should possess Ni^{+++} and Ni^{+} ion pairs, but this requires energy E to remove an electron from one nickel ion Ni^{++} and put it on a distant one. Such a situation is possible only if the whole NiO crystal is in a higher energy state, for example, at a high temperature. The energy cost of moving electrons between ions comes from the Coulomb repulsion, which was omitted by the band theory.

In 1963, John Hubbard, inspired by Mott's work, created the simplest lattice model capturing the essential physics of Mott insulators [12]. The model describes fermions (electrons) hopping between single-orbital lattice sites and interacting with each other. Due to the Pauli exclusion principle, each orbital can be occupied by at most two fermions with opposite spins. The Mott-Hubbard Hamiltonian has the form:

$$H_{Hubb} = -t \sum_{<i,j>,\sigma} a^{\dagger}_{i\sigma} a_{j\sigma} + U \sum_{i} n_{i\uparrow} n_{i\downarrow}. \tag{1.1}$$

where $a_{i\sigma}$ ($a^{\dagger}_{i\sigma}$) is a fermionic operator annihilating (creating) an electron with spin σ on the i-th lattice site, and $n_{i\sigma} = a^{\dagger}_{i\sigma} a_{i\sigma}$ is the particle number operator. The first term is kinetic energy with electron hoppings between nearest neighbors and constant amplitude t, and the second term introduces the on-site repulsive Coulomb interaction when two electrons occupy one site. Amplitudes t and U are competing; the on-site interaction restricts the motion of electrons and favors insulating behaviors. This competition results in the transition between conducting and insulating phases. Assume that the system is half-filled: the number of particles equals the number of orbitals. In the limit of $U \gg t$, the energy cost of double occupancy of the orbital is too high, and electrons are "frozen" on single-occupied orbitals, which results in the system resolving into a set of isolated magnetic moments. In such cases, the kinetic term of the Hamiltonian still gives corrections to the total energy by introducing the exchange of antiparallel spins on neighboring sites, which leads to magnetic correlations in the system. Electrons with opposite spins are able to perform virtual hopping between neighboring spins, which is explained by second-order perturbation theory. First-order process is a single hop, which creates double occupancy and then is forbidden in the low-

energy subspace. However, at the second order, an electron can virtually hop to another site and hop back, which lowers the energy of the state with total spin $S = 0$ [31]. Nowadays, Mott insulating phases have been theoretically predicted and experimentally observed in various novel materials, such as transition metal dichalcogenides (TMDs) monolayers [32–34], twisted bilayer graphene [35, 36], and even organic layered structures [37].

1.2 Topological phases

In strongly correlated systems, the interplay between electronic interactions and quantum entanglement results in topological phases that go beyond the traditional Landau symmetry-breaking paradigm. In Landau's classification, phases are distinguished by spontaneous symmetry breaking and characterized by a local order parameter that changes across the phase transition [38]. For example, in a ferromagnet the order parameter is the uniform magnetization, which vanishes in the high-temperature paramagnetic phase but acquires a finite value below the Curie temperature. Unlike conventional phases, topological phases are not characterized by a local order parameter, but by nonlocal properties such as topological invariants, protected edge states, or entanglement structure [39].

Two broad categories are usually distinguished within classification introduced by Wen [40]. Symmetry-protected topological (SPT) phases, such as the Haldane phase in spin-1 chains [41] or topological Mott insulators [42], are stable only in the presence of certain symmetries like time-reversal or inversion. If the symmetry is broken, these phases can be smoothly deformed into the trivial product state by adiabatic evolution. SPT phases are characterized by short-range entanglement, and their distinction comes from a nonlocal order parameter [43]. Symmetries are protected by an open gap, which has to close on the boundary between the topological and trivial phases, resulting in robust edge states. Modern classification of SPT phases uses quantum entanglement structure (e.g. projective representations, group cohomology) [44–46]. For example, the Haldane phase is classified within the group cohomology as $\mathbb{Z}_2$ phase, while in general 1D bosonic SPT phases with a symmetry group G are classified by the second cohomology group $H^2(G, U(1))$ [47].

By contrast, intrinsic topological order does not require symmetry and remains robust even when all symmetries are broken [48]. These phases,

described by Wen's framework of topological order [49], are characterized by long-range entanglement, topological ground-state degeneracy on manifolds of nontrivial topology, and the presence of fractional or anyonic excitations. Unlike SPT phases, such phases cannot be adiabatically connected to a trivial state, even in the absence of symmetries. Examples of such states are those of the fractional quantum Hall effect (FQHE) and their lattice analogs known as fractional Chern insulators (FCIs) [50].

1.3 Spin chains

A spin chain is a one-dimensional model of quantum spins located at fixed sites on the lattice. Interactions between spins are modeled by pairs of operators acting on two, usually neighboring, sites [51–53]. The most common Hamiltonian for the spin chain consists of two terms:

$$H = \sum_i \mathcal{H}_i + \sum_{i,j} \mathcal{J}_{ij} \vec{\mathbf{S}}_i \cdot \vec{\mathbf{S}}_j, \tag{1.2}$$

$\mathcal{H}_i$ is a single-site term, acting on the one spin (e.g., local magnetic field), and $\mathcal{J}_{ij}$ represents the coupling strength between spins at sites i and j.

The quantum Heisenberg model was first proposed by Werner Heisenberg in the 1920s [54]. It is represented by the Hamiltonian, which includes exchange interaction terms between neighboring sites:

$$H = -J \sum_i \vec{\mathbf{S}}_i \cdot \vec{\mathbf{S}}_{i+1}, \tag{1.3}$$

where J is an exchange coupling constant, and $\vec{\mathbf{S}}_i$ is a spin operator acting on the site "i".

When $J < 0$, the energy of the system is the lowest for the state with all pairs of spins aligned parallel in one direction simultaneously, which is the *ferromagnetic* arrangement. Such a state is the eigenstate of the Hamiltonian Eq.1.3, so it is the actual solution of the Schrödinger equation with the lowest energy. The energy of such a ground state is $E = S^2 PJ$, where P is the number of pairs of spins [55]. If $J > 0$, two spins minimize their energy when they are antiparallel. The one-dimensional system is bipartite so that all spins can align in directions other than both their neighbors without

frustration. It is a classical *antiferromagnetic* order. In contrast to the ferromagnetic ground state, such a state is not the eigenstate of the Heisenberg Hamiltonian [56, 57].

The most general rotationally invariant coupling between two spins S can be written as: $U_{ij} = \sum_{k=0}^{2S} A_k (\mathbf{S}_i \cdot \mathbf{S}_j)^k$. For $S = \frac{1}{2}$, it reduces to a bilinear form, equivalent to the Heisenberg Hamiltonian (up to a constant shift). However, for integer spin $S = 1$, this relation allows additional biquadratic term.

1.3.1 Half-integer spin chains

Despite its simple formulation, the antiferromagnetic Heisenberg model exhibits strong correlations, which means that spins are highly interdependent, leading to complex collective behavior. One of the most extensively studied spin models is a chain of spin-1/2 particles with antiferromagnetic coupling. In such systems, the excitation spectrum is gapless, and spin-spin correlation functions of the ground state decay according to a power law [53, 58]. Although the classical antiferromagnetic Neél state is not the eigenstate of the Hamiltonian, strong quantum fluctuations in 1D systems, even at temperatures close to zero, lead to a ground state with quasi-long-range order. This behavior is a direct consequence of the low dimensionality of the system, which enhances quantum fluctuations and suppresses the development of true long-range order.

The dynamic of this system is governed by low-energy excitations, which are often described in terms of fractionalized collective modes known as spinons [59,60]. In most magnetic systems, low-energy excitations are bosonic quasiparticles with integer spin—such as magnons in a ferromagnet, where a spin flip creates a collective mode carrying spin-1. A single spin flip in the antiferromagnetic chain fractionalizes into a pair of spinons, which carry spin-1/2 each. Exact eigenstates can be obtained directly from the algebraic Bethe ansatz [56], which reveals that the excitation spectrum consists of a continuum of spinon states rather than conventional magnons [61]. A spinon can be interpreted as a domain wall in the local antiferromagnetic order, or equivalently as a hole-like excitation in the sea of interacting spins. Recent works in this subject suggest an alternative picture, a single spinon behaves like one spin moving in a frozen valence bond solid (VBS) [62]. The presence and interaction of spinons show the non-trivial nature of the ground state in these systems, suggesting that the system's low-energy physics is governed

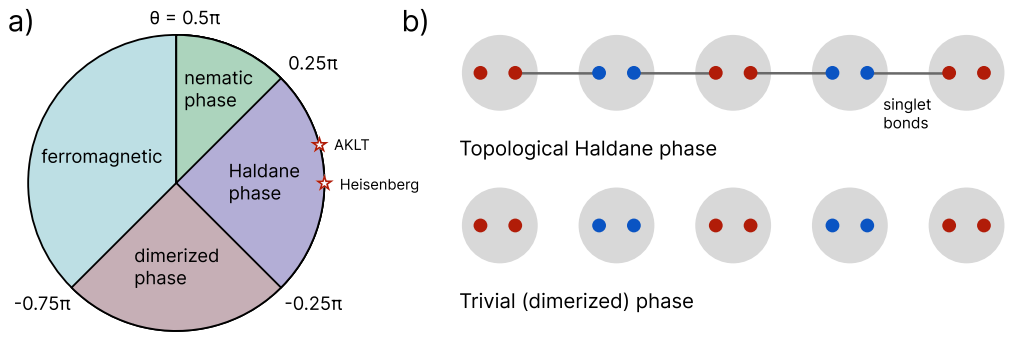

Figure 1.2: (a) Phase diagram of the bilinear-biquadratic spin-1 Hamiltonian. (b) Schematic illustration of the topological AKLT phase and the trivial dimerized state. Each spin-1 site (grey dot) is represented as a pair of spin-$\frac{1}{2}$ objects (blue and red dots) coupled ferromagnetically, while solid lines indicate singlet bonds.

by highly entangled quantum states. Experimentally, such excitations can be probed by inelastic neutron scattering at low temperatures [63, 64]. Among the systems analyzed with this technique are nanographene chains, which will be discussed in the following sections [65].

Another manifestation of strong correlations in spin-1/2 chains is the appearance of spin polarons. A polaron, in general, is a quasiparticle formed when a charge carrier moves through the system, causing local distortion of the lattice, effectively dressing itself with a cloud of phonons [66, 67]. This phenomenon is well established in two-dimensional systems, but an analogous effect also appears in one-dimensional antiferromagnetic chains doped with a single hole [68–70]. In these cases, the polaron can become unstable and split into a spinon and a spinless hole, known as a holon [71]. This process, known as spin-charge separation [72, 73], provides further insight into the interplay between spin and charge degrees of freedom in these systems. The phenomenon of spin-charge separation has profound implications for understanding strongly correlated electron systems, such as those found in high-temperature superconductors and other low-dimensional materials.

1.3.2 Integer spin chains

In the case of integer spins $S = 1, 2, 3, \ldots$ in the antiferromagnetic phase, the Heisenberg chain has a gap in the excitation spectrum predicted by Haldane's conjecture. Specifically for $S = 1$, the ground state is gapped, and the system exhibits long-range entanglement, which is a hallmark of strong correlations [27, 74]. For spin-1 systems, keeping only the $k = 1, 2$ terms in general formula mentioned before section 1.3.1 yields the bilinear–biquadratic (BLBQ) Hamiltonian. To explore its rich phase diagram (Fig.1.2 (a)), one often studies the one-parameter family of the BLBQ model [75, 76]:

$$H_\theta = \cos\theta \sum_i \vec{\mathbf{S}}_i \cdot \vec{\mathbf{S}}_{i+1} + \sin\theta (\vec{\mathbf{S}}_i \cdot \vec{\mathbf{S}}_{i+1})^2. \tag{1.4}$$

Starting from $\theta = \pi$, one finds a ferromagnetic, gapless phase with long-range order. In accordance with Coleman's theorem, it is the only ordered phase in a 1D spin-1 chain due to the conservation of its S_z order parameter. Then, at $\theta = -0.75\pi$, a continuous phase transition occurs, leading to the dimerized phase, in which the ground state is a doubly degenerated singlet. The phase is characterized by the order parameter given as c_2 in the singlet-singlet correlation function: $\langle (\vec{S}_i \vec{S}_{i+1})(\vec{S}_j \vec{S}_{j+1} \rangle \to (-1)^{i-j} c_2 + A$ for $|i - j| \to \infty$. The dimerized phase is topologically trivial, and after a smooth change of the parameter θ to the point -0.25π, the system moves to the topological Haldane phase. The Haldane phase is a symmetry-protected topological (SPT) phase with a unique disordered ground state [77], a gap in the excitation spectrum, and robust edge states. As Gu and Wen show [78], it can be distinguished from a topologically trivial one in the presence of three symmetries: translation, complex conjugation, and inversion symmetry. Some topological phases can be characterized by their entanglement properties. For this purpose, we partition the system into two subsystems and calculate their density matrices as $\rho_A = \mathrm{Tr}_B(\rho_{AB})$. The eigenvalues of this reduced density matrix, usually expressed as "entanglement energies," provide the spectrum. Pollman noticed that, as long as the condition of the presence of three symmetries is met, the topological Haldane phase is stable, which is reflected by non-trivial, even-fold degeneracies in the entanglement spectrum [79]. The SPT phase lacks a local order parameter but, in some instances, can be characterized by the existence of fractionalized edge excitations or a non-zero value of the non-local string order parameter defined

as:

$$\mathcal{O}^{\alpha} = -\lim_{|j-i|\to\infty} \langle S_i^{\alpha} \exp\left(i\pi \sum_{i<k<j} S_k^{\alpha}\right) S_j^{\alpha} \rangle. \tag{1.5}$$

However, as Gu and Wen showed, based on the Tensor Entanglement Filtering Renormalization Group (TEFR), the string order parameter can vanish in the presence of some perturbation [78]. Yet, it does not imply the instability of the Haldane phase, which can be confirmed by the double degeneracies of the entanglement spectrum.

The special case of the state belonging to the Haldane phase is one proposed by Affleck, Kennedy, Lieb, and Tasaki (AKLT) in 1987 [80, 81]. The AKLT state is a ground state of the Hamiltonian (1.4) for $\tan(\theta) = 1/3$ and can be solved exactly. The AKLT Hamiltonian can also be written as a sum of projectors onto the $S = 2$ subspace for neighboring spins:

$$H_{AKLT} = 2\sum_i \left(P_{i,i+1}^{S=2} - \frac{1}{3} \right).$$

The Hamiltonian is bounded from below and it is semipositive, so its lowest eigenvalue is $E = 0$ and the corresponding ground state is the valence bond solid with a single valence bond connecting every neighboring pair of sites. The simplest way to understand that is to decompose the spin-1 site onto a singlet of two spins-1/2 (Fig.1.2 (b)). The valence bond connects spins-1/2 from two different sites. For the periodic boundary conditions, such a ground state is unique. However, in the case of an open chain, two sites at the ends have only one neighbor, so one spin-1/2 from each pair remains without a partner. It creates fractionalized spin-1/2 edge states and yields a ground state manifold that is four-fold degenerate. Besides the occurrence of the edge states, the AKLT ground state is characterized by purely exponential spin correlations with correlation length $\xi = \ln(3)^{-1} \approx 0.91$ and a finite value of the string order parameter $\mathcal{O}^z_{AKLT} = -0.444(4)$. The AKLT state is a special case, but the ground state of the isotropic Heisenberg model ($\theta = 0$) also belongs to the Haldane phase. It also has a gapped spectrum and exponentially decaying spin correlations obeying a law $\langle \vec{S}_0 \cdot \vec{S}_n \rangle \approx (-1)^n \exp(-\frac{n}{\xi})/\sqrt{n}$, although the correlation length tends to be much bigger than for the AKLT state.

The third phase transition occurs at the point $\theta = 0.25\pi$ when the system shifts from the Haldane phase to the critical one with a gapless excitation spectrum. And at $\theta = 0.5\pi$ the ferromagnetic phase is established again.

Due to the richness of the phase diagrams and the occurrence of strongly correlated and topological phases, spin chains are important platforms to study the interplay between interactions, entanglement, symmetries, and topology in low dimensions.

1.4 Kondo effect

The Kondo effect was first explained by Jun Kondo in 1964 [17]. This phenomenon involves the appearance of a minimum in the resistivity of certain dilute alloys containing magnetic impurities, followed by a logarithmic increase in resistivity (ρ) as the temperature decreases [82]. In contrast, the usual behavior in other metals is that resistivity decreases with temperature due to reduced electron scattering [83]. Kondo's explanation for this unusual behavior was that the magnetic moment of the impurity is screened by the conduction electrons, forming a Kondo singlet state. In this state, the localized magnetic impurity is effectively "quenched" by the conduction electron spins, leading to the characteristic low-temperature behavior of the system. This interaction between the localized magnetic moment and the delocalized conduction electrons is strong enough to influence the electronic properties of the material, especially at low temperatures [84]. To model this interaction, Kondo formulated the Kondo model, which describes the coupling between a single magnetic impurity and a sea of conduction electrons. This model became the foundation of many-body studies in condensed matter physics [85, 86]. It demonstrated how strong electron-electron interactions could give rise to complex behavior, including the formation of a collective spin-singlet state at low temperatures. The insights gained from the Kondo effect and its model served as a precursor to the development of more general concepts in strongly correlated systems, such as heavy-fermion systems, quantum criticality, and non-Fermi liquid behavior [87–93].

Over the decades, the study of the Kondo effect expanded to systems with many impurities, leading to the study of Kondo lattices and heavy fermion compounds, where interactions between multiple impurities and the conduction electrons result in novel states of matter, such as quantum spin liquids and unconventional superconductivity [94–97].

1.5 Fractional Chern insulators, superconductivity, spin liquids

Strong correlations between electrons lead to many exotic phases of matter, which have recently attracted considerable attention from researchers. One particularly intriguing example of the interplay between strong interactions and topology is the fractional Chern insulator (FCI), which emerges in lattice systems with topological flat bands [98–101]. FCIs are lattice counterparts of the well-known fractional quantum Hall effect (FQHE) [102–104], but notably, they do not require an external magnetic field [105]. These phases form when strongly interacting electrons partially fill a flat Bloch band with a nonzero Chern number. The flatness of the band suppresses kinetic energy, allowing electron-electron interactions to dominate and lift the degeneracy in the band, similar to interactions stabilizing FQHE states in Landau levels. As a result, FCIs exhibit hallmark features of the FQHE, such as fractionalized quasiparticles and quantized Hall conductance.

Fractional Chern insulating states have been demonstrated in semiconducting moiré materials, such as twisted bilayer $MoTe_2$, which support tunable topological flat bands [106–109]. In such structures, the twist angle between monolayers alters the moiré potential confining the electrons and can amplify or suppress interactions between them [29]. Due to this property, the phase diagrams of moiré materials are rich in strongly correlated states. In addition to FCIs, other exotic phases, such as quantum spin liquids and unconventional superconductivity, are expected to be seen [110–114].

In recent works, a new important factor stabilizing correlated phases in flat-band systems has been identified: the quantum geometry of Bloch wavefunctions [115]. Quantum geometry is captured by the quantum geometric tensor (QGT), which consists of two complementary parts. Its imaginary component, the Berry curvature, captures the topology of a band and underlies phenomena such as the quantized Hall response in FCIs. Its real component, the quantum metric, measures the distance between neighboring Bloch states in momentum space. The quantum metric gives a geometric contribution to the superfluid weight, suggesting its contribution to superconductivity emerging in flat-band materials even in the absence of kinetic energy [116–118].

In conventional bulk superconductors, electron correlations do not play a crucial role. Bosonic Cooper pairs, bound pairs of electrons, are formed due

to an attractive interaction mediated by lattice vibrations (phonons), as described by the Bardeen-Cooper-Schrieffer (BCS) theory [119–121]. The pairing symmetry is typically isotropic (s-wave), and the critical temperature usually remains below 30 K [122,123]. In contrast, unconventional superconductivity requires strong electron correlations. The pairing mechanism behind unconventional superconductors is still an active area of research [124, 125]. In materials such as cuprates, heavy-fermion compounds, and certain moiré systems like magic-angle twisted trilayer graphene (MATTG) [111,126–129], attractive interactions—believed to arise from antiferromagnetic spin fluctuations - are considered responsible for Cooper pair formation. The resulting superconducting phases often exhibit p-wave or d-wave symmetry and can persist at elevated temperatures, up to 150 K [130]. On the other hand, it has been speculated that superconductivity in magic-angle twisted bilayer graphene (MATBG) may originate from the non-trivial topology of its flat bands. In this scenario, the primary charge carriers may be skyrmions—solitonic spin textures that carry an electric charge. These stable, nanoscale structures behave like quasiparticles, and theoretical studies suggest that under specific conditions, skyrmions can pair up, forming bound states with charge $2e$, similar to Cooper pairs in conventional superconductors [131, 132]. Unconventional superconductivity is also closely related to another class of strongly correlated states: quantum spin liquids (QSLs). QSLs emerge in strongly interacting spin systems where conventional magnetic ordering is suppressed by quantum fluctuations and geometric frustration. Unlike classical magnets, a QSL state is a quantum superposition of many spin configurations, with persistent spin fluctuations even at zero temperature, resulting in a disordered yet highly entangled ground state. This long-range entanglement characterizes the QSL, along with the absence of symmetry breaking, the presence of fractionalized excitations, and emergent gauge fields [133]. In gapped, time-reversal symmetric QSLs, slight doping can induce superconductivity. From the perspective of superconductivity theory, the QSL ground state can be interpreted as a state with preexisting Cooper pairs but vanishing superfluid stiffness. This parameter becomes nonzero when the system exhibits a coherent macroscopic quantum state; in superconductors, it determines how easily supercurrents flow and how effectively the material expels magnetic fields (via the Meissner effect). Numerical studies have shown that even small levels of doping in QSLs on triangular lattices can enhance the superfluid stiffness, leading to a superconducting ground state [134, 135].

Chapter 2

Introduction II: Quantum simulators

Strongly correlated systems are fascinating and essential in today's research, yet they remain challenging to study. When the correlations between electrons are weak, the interactions can be treated as small perturbations, allowing ones to describe the system using mean-field or perturbative methods [136]. These approaches are computationally efficient and often provide valuable insight into the system's behavior. However, the range of physical systems for which these methods offer an accurate description is limited.

To capture strong correlation effects, the model must include electron-electron interactions explicitly. The main challenge with this approach is scalability. The size of the Hilbert space increases exponentially as it must account for all possible configurations of particles across orbitals or lattice sites. Even in the case of the fermionic Hubbard Hamiltonian, which is the simplest model including interactions between fermions, and assuming that the number of sites L is equal to the number of particles N, the Hilbert space at the half-filling (one particle per site) already has a dimension of $\dim\mathcal{H} = 2^L$. Away from the half-filling, when $N \neq L$, each site has four possible local states: empty $|0\rangle$, spin up $|\uparrow\rangle$, spin down $|\downarrow\rangle$, and double occupancy $|\uparrow\downarrow\rangle$, giving a maximal Hilbert space dimension of 4^L [137].

For electron systems with Coulomb interactions, the particle number operator $\hat{n}$ commutes with the Hamiltonian $\hat{H}$, and the full Hilbert space $\mathcal{H}$ can be decomposed into a direct sum of subspaces with fixed particle number: $\mathcal{H} = \bigoplus_{i=1}^{N} \mathcal{H}_i$. Exploiting symmetries, such as total spin, momentum, or lattice point group symmetries, can further reduce the size of the corresponding

matrix form of the Hamiltonian. Despite these optimizations, doing the numerical diagonalization of a matrix of size D $\times$ D demands memory space on the order of $\mathcal{O}(D^2)$ and takes time on the order of $\mathcal{O}(D^3)$, which makes it impossible for large systems due to the hardware limitation. In practice, obtaining all eigenvectors and eigenvalues of the Hamiltonian is not necessary since physical properties at low temperatures are often governed by the ground state and a few low-lying excited states. For this reason, algorithms that perform partial diagonalization, such as Lanczos or Davidson methods, are widely used [138,139]. These methods can efficiently find extremal eigenvalues but still face limitations due to the exponential growth of the Hilbert space.

Additional complications arise depending on the chosen numerical method. For instance, Quantum Monte Carlo (QMC) [140], one of the most powerful techniques for studying many-body systems, struggles with fermions on frustrated lattices due to the sign problem [141]. In these cases, probability amplitudes can be negative or complex, leading to huge cancellations during statistical sampling and making simulations extremely noisy or even infeasible. Variational methods, on the other hand, rely on optimizing a trial wavefunction within a constrained ansatz [142,143], which can be effective in some cases—but they often struggle to resolve systems with nearly degenerate ground states accurately. In such situations, small differences in energy can be masked by the limitations of the ansatz or the optimization algorithm, making it difficult to distinguish between competing phases or capture the correct low-energy physics. Additionally, the accuracy of variational methods strictly depends on the quality of the chosen trial wavefunction. Recently density matrix renormalization group (DMRG) have become a main tool to study strongly correlated systems at low dimensions [144, 145]. It will be discussed in more details in Methodology chapter.

Due to these computational limitations, there has been growing interest in an alternative solution to the many-body quantum problem: condensed matter quantum simulators, which were proposed by Feynman as a way to approach the issue from the opposite side [146]. Instead of solving the many-body problem numerically, the idea is to build a physical system that naturally emulates the target Hamiltonian in a controllable setting [147, 148]. There have been several proposals for quantum simulators that include ultracold atoms, in optical lattices [149] or moiré materials in van der Waals heterostructures [150,151], allowing to directly probe the behavior of strongly correlated electrons in regimes that are inaccessible to classical computation.

They can capture many subtle many-body effects, such as entanglement, topological order, and competing ground states, without the approximations and constraints inherent to variational techniques. Quantum simulators may allow us to discover novel quantum phases and conduct controlled studies of quantum criticality or unconventional phase transitions.

2.1 Semiconducting van der Waals nanostructures

A promising platform for the realization of condensed matter quantum simulators is found in van der Waals heterostructures [152–154]. These unique nanoscale systems are built by stacking different monolayers on top of each other. Layers are held together by weak van der Waals forces, while atoms inside one monolayer are bonded covalently. A monolayer is a two-dimensional crystal with a thickness of just one unit cell. The most well-known example is graphene — a single layer of carbon atoms extracted from bulk graphite [155, 156].

Monolayers can exhibit physical properties that differ significantly from those of their bulk counterparts. Next to the graphene, one of the most profound examples is the transition metal dichalcogenides (TMD) monolayer, which follows the general chemical formula MX_2, where M denotes a transition metal, and X represents a chalcogen element. Their crystal structure consists of one atomic layer of metal atoms sandwiched between two layers of chalcogen atoms, forming a hexagonal (honeycomb) lattice when viewed from above. The bulk TMDs possess an indirect band gap, due to the interaction between layers, modifying the momentum conservation rules for interband scattering [157]. Besides that, the presence of interlayer interactions in the bulk also leads to broadening and splitting of energy bands, which do not occur in monolayers. In contrast, in their monolayer forms, quantum confinement dominates electronic properties, which results in a direct band gap [158]. The conduction and valence band extrema are aligned at the K points of the Brillouin zone, which enhances the light-matter interactions and excitonic effects. This property makes TMD monolayers excellent candidates for use in transistors, photodetectors, and light-emitting devices [159–162].

The most widely used method for producing monolayers is mechanical exfoliation [163, 164]. This "top-down" approach reduces the thickness of

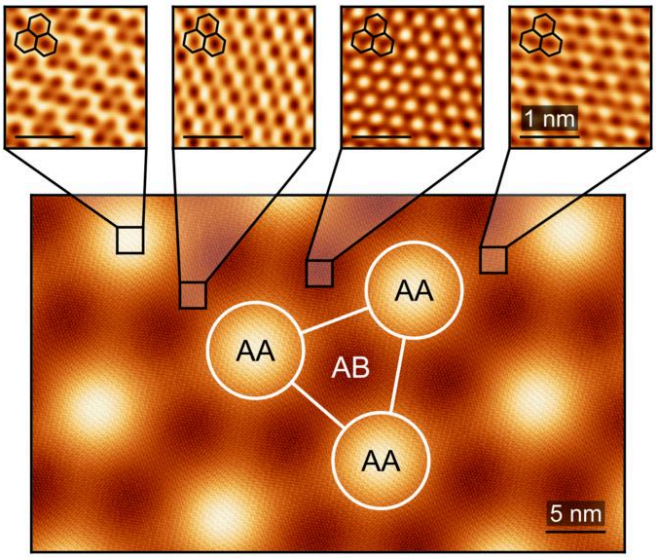

Figure 2.1: High-resolution image showing quantum interference in the MATBG with the scanning tunneling microscope. Image Credit: Kevin Nuckolls, Yazdani Group [1].

a bulk crystal by peeling off individual layers, overcoming the weak interlayer van der Waals forces. The process can be optimized by analyzing the crystal structure and aligning the exfoliation direction appropriately. Its key advantage lies in its simplicity and potential scalability for industrial applications. In contrast, epitaxial growth represents a "bottom-up" technique, where atoms condense from a gas phase to form a thin crystal layer on a substrate [165]. This method yields monolayers of exceptionally high quality with minimal defects, making them ideal for electronic applications. However, its main limitations are the high cost of production and limited scalability.

Recent advancements in the mentioned methods allow us to obtain a broad family of TMD monolayer crystals, which serve as building blocks for more complex van der Waals heterostructures with new electronic and optical properties.

2.1.1 Moiré van der Waals structures

The main issue in realizing quantum simulators in conventional chemical compounds is the lack of tunability. Usually, available control knobs to tune electronic properties of the sample are pressure, strain, and doping, which may be insufficient for the experimental exploration of wide phase diagrams. Due to this, researchers are looking for novel condensed matter platforms characterized by high tunability.

Moiré van der Waals materials [166, 167] provide researchers with new possibilities for controlling system properties by exploiting quantum interference. When the layers forming the heterostructure have different lattice constants or are twisted relative to each other, a new periodicity emerges in the system (Fig. 2.1) [168]. This process is analogous to its classical counterpart: a large-scale interference pattern that appears when a partially opaque material with transparent gaps is overlaid on another, with a displacement or rotation between them. Such effects are common in everyday life, for example, in printing, graphic design, or photography. On the atomic scale, for each heterostructure consisting of two or more monolayers, one can identify a set of commensurate twist angles [169]. Twisting the monolayers by these angles preserves spatial periodicity in the system, but with a much larger moiré unit cell. The resulting moiré superlattice defines a new crystal structure, characterized by a much smaller moiré Brillouin zone. The energy bands are folded into this reduced zone, leading to multiple band crossings. Simultaneously, interlayer hybridization splits these crossings. For certain values of the twist angle, this process leads to the formation of nearly dispersionless energy bands [170–173].

The quantum interference in the moiré structures quenches the effective kinetic energy scales and can enhance interaction between electrons. This effect can be understood from the perspective of an electron localized in a moiré band. In a real space, such an electron can be viewed as occupying a virtual moiré orbital, which extends over hundreds of atoms in the new moiré unit cell, and its shape depends on the twist angle. Due to this, the interaction between electrons also depends on the twist angle. Since these moiré bands form the low-energy electronic structure near the Fermi level, the suppression of kinetic energy directly governs the many-body states accessible in experiments. For smaller angles, the kinetic energy scales decrease at a higher rate than the interaction strength, which allows tuning the system into a strong correlation regime, even if it consists of weakly correlated monolayers

[171].

Impressive possibilities of the moiré superlattices were already demonstrated for twisted bilayer graphene (TBG). For certain values of commensurate angles, known as "magic angles", moiré bands near charge neutrality become nearly flat, greatly enhancing the effects of electron-electron interactions [174]. This results in the rich diagram of strongly correlated phases like correlated insulators, unconventional superconductivity, or topological quantum anomalous Hall effect, which are highly tunable and experimentally accessible [175–180].

In Figure 2.2, fragments of the moiré superlattice for the TBG are demonstrated in real space. To describe the geometry of graphene monolayers stacked and twisted, one must define moiré superlattice basis vectors. The honeycomb lattice of one graphene sheet has two sublattices A and B. Positions of carbon atoms in a sublattice α are given by $\mathbf{r} + \tau_\alpha$, where $\mathbf{r}$ are vectors from the triangular Bravais lattice spanned by the primitive vectors $\mathbf{a}_1 = a_0\sqrt{3}\hat{\mathbf{x}}$ and $\mathbf{a}_2 = R_{-\pi/3}\mathbf{a}_1$. One can choose constant vectors τ_α as $\tau_A = a_0\hat{\mathbf{y}}$ and $\tau_B = R_{-\pi/3}\tau_A$. For the twist angle θ, those positions are transformed as $\tau'_A = R_{+\theta/2}\tau_A$ and $\tau'_B = R_{-\theta/2}\tau_B$. If θ is a commensurate angle, it can be defined by one integer number i according to the relation [170]:

$$\cos\theta_i = \frac{3i^2 + 3i + 1/2}{3i^2 + 3i + 1}, \tag{2.1}$$

so for $i = 2$ the twist angle is $\theta = 13.17^\circ$ and the magic angle $\theta = 1.05$ is obtained for $i = 31$. The lattice vectors of the moiré unit cell are defined as:

$$\mathbf{L}_1^M = i\mathbf{a}_1 - (i+1)\mathbf{a}_2, \tag{2.2}$$

$$\mathbf{L}_2^M = -(i+1)\mathbf{a}_1 - (2i+1)\mathbf{a}_2. \tag{2.3}$$

The number of carbon atoms in moiré unit cell is increasing for smaller twist angles. In case of $\theta = 38.2^\circ$ (Fig.2.2b), it consists of 28 atoms, whereas for the magic angle it is already 11,908. This rapid growth makes it challenging to analyze small-angle moiré materials using a fully atomistic approach.

One of the main advantages of moiré heterostructures lies in the diversity of possible moiré superlattice types [181]. Depending on the choice of monolayers, for commensurate twist angles, one can observe the formation of honeycomb, triangular, or rectangular superlattices. Furthermore, at incommensurate angles, twisted heterostructures may give rise to quasicrystals —

structures that exhibit high rotational symmetry but lack translational symmetry. Quasicrystals are particularly interesting because they host unconventional electronic states that do not arise in periodic crystals. A notable example is twisted bilayer graphene at 30°, which forms a quasicrystal with 12-fold rotational symmetry, known as a dodecagonal quasicrystal [182].

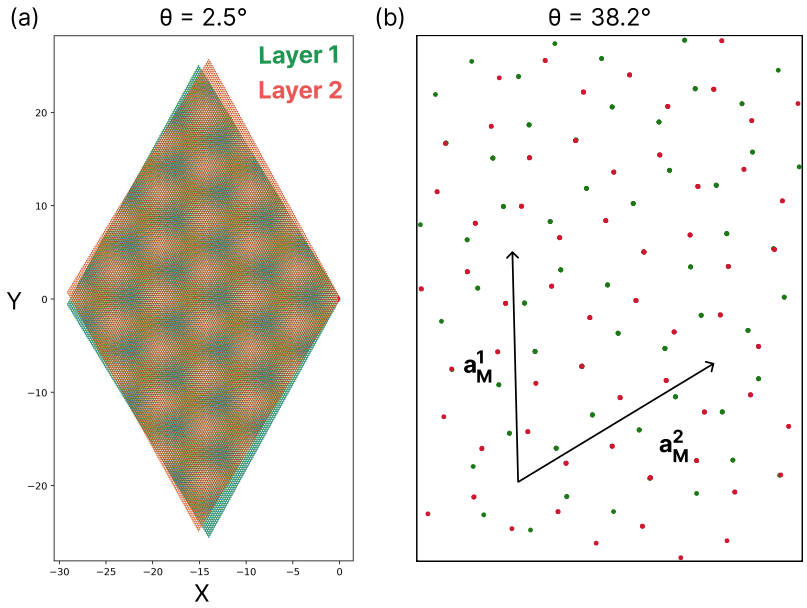

Figure 2.2: Fragments of TBG moiré superlattices in real space for twist angle $\theta = 2.5°$ (a) and $\theta = 38.2°$ (b). Green dots denote positions of atoms from the first layer, and red ones from the second layer.

2.1.2 Homobilayers

Inside the family of TMD moiré structures, one possessing a honeycomb superlattice, similarly to the TBG, is the MoS_2 bilayer. In those structures, two sets of flat bands are observed, from which the first one realizes the single orbital Hubbard model, and the second one a highly anisotropic p_x-p_y Hubbard Hamiltonian [183]. This gives an interesting opportunity for experimental realization and analysis of nemetic magnetism.

The effective triangular lattice can be obtained by twisting two sheets of hexagonal boron nitride (hBN), which is sometimes called a "white graphene"

due to its similar hexagonal geometry [184]. However, in contrast to graphene, the hBN lattice consists of two different atoms in the unit cell, which results in a large band gap. A single hBN monolayer is widely used as a substrate for TBG and in other van der Waals heterostructures, because of its insulating properties. The density functional theory (DFT) calculations [185] reveal multiple flat bands, which emerge for small twists, but without the fine-tuning of angle required for TBG. Similar to the magic angle TBG, twisted bilayer hBN possibly supports topological superconductivity upon doping and spin density waves. The physics of its flat bands separated from the valence and conduction bands can be described with the multi-orbital Kanamori models.

A similar effect can be obtained with TMD materials. The low-energy flat bands with Wannier functions forming a triangular lattice have been reported in twisted bilayer WSe_2 [186]. The signatures of correlated insulating phases occur in the system for twist angles that range from 4° to 5.1°. As a quantum simulator, bilayer WSe_2 gives access to such phases as Stoner ferromagnetism and Chern insulators, controlled with external electric and magnetic fields [187]. Other research shows that topological flat bands emerging in TMD homobilayers may result in fractional Chern insulator states [188].

2.1.3 Heterobilayers

An alternative route to simulate models on a triangular lattice with moiré materials is provided by TMD heterobilayers. When two monolayers with different lattice constants are stacked to form a heterostructure, a moiré pattern can emerge even in the perfectly aligned case. The combination of lattice mismatch and twist angle produces a tunable superlattice potential that acts on the carriers. This potential creates narrow bands with triangular symmetry, where Coulomb interactions dominate over kinetic energy. In this strongly interacting regime, moiré TMD heterobilayers serve as solid-state quantum simulators of Hubbard-like physics, enabling the realization of correlated insulators at integer fillings, charge-ordered phases at fractional fillings [189–191]. Theory also predicts other exotic many-body phenomena like quantum spin liquids and Wigner crystals [192–194].

Moreover, a periodic potential significantly modifies exciton states emerging in those systems. One of the unique features of moiré heterobilayers is the formation of interlayer excitons. Experimental and theoretical studies of TMD heterobilayers show that their conduction band minimum and valence

band maximum are separated between monolayers, which causes interlayer charge transfer [195–199]. With the addition of strong Coulomb interaction due to electron confinement, such a situation favors the production of spatially separated, bounded electron-hole pairs with long lifetimes [200–202].

Recent experiments using moiré TMD heterostructures have achieved concrete realizations of Hubbard-like and related physics [203]. The angle-aligned WSe_2/WS_2 bilayers show a Mott insulating state at half-filling of the first hole moiré superlattice band, with optical and magnetic measurements revealing antiferromagnetic Curie–Weiss behavior and a possible transition to weak ferromagnetism at higher hole densities [189]. WSe_2/WS_2 devices also exhibit stripe-ordered insulating phases at fractional fillings, with strong spatial anisotropy, which match extended Hubbard model predictions on triangular moiré lattices [204]. Researchers using moiré quantum simulators are also able to get insight into the tunable quantum criticality [205] and Wigner crystal physics [190, 206, 207]. More complicated lattice systems, like the ionic Hubbard model on the honeycomb lattice, are simulated by introducing interference between moiré patterns in structures with more than two twisted monolayers [208, 209].

Another route for realizing strongly correlated models with moiré heterostructures involves twisted bilayer GeSe, a material with a rectangular lattice structure. In contrast to the two-dimensional moiré patterns observed in hexagonal systems, small twist angles between GeSe monolayers lead to the formation of highly anisotropic, quasi-one-dimensional moiré patterns. The resulting flat bands can be effectively described by an ionic Hubbard model, capturing the interplay between strong electron correlations and a staggered potential [210]. This system provides an opportunity to simulate one-dimensional physics, including Mott insulating phases, Luttinger liquids, and bond density waves, and to explore quantum phase transitions such as Ising and Kosterlitz-Thouless transitions in a controllable solid-state platform [211].

In summary, moiré engineering in twisted bilayers and heterostructures offers a framework for simulating a wide range of strongly correlated phases, from two-dimensional Hubbard systems to one-dimensional ionic Hubbard chains. By carefully selecting materials and tuning the twist angle, it becomes possible to design artificial lattices with flat bands, enhanced correlations, and rich phase diagrams, providing a platform for exploring quantum phases in a highly controllable environment.

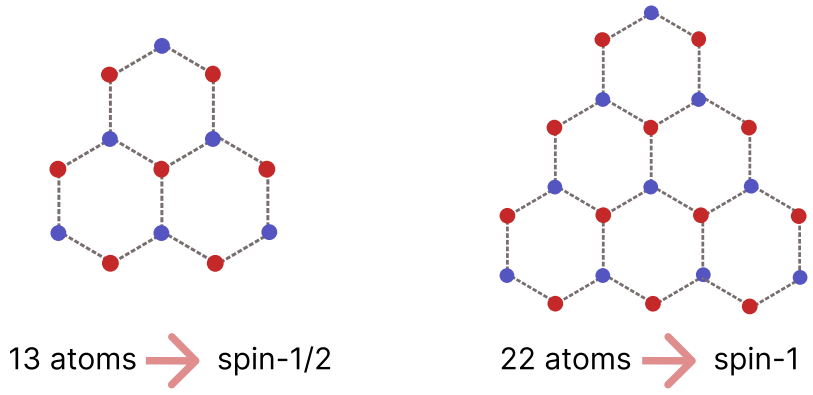

Figure 2.3: The two smallest triangular graphene quantum dots.

2.2 Graphene nanostructures

The other class of promising quantum simulators consists of graphene nanostructures, which come in various shapes and sizes, such as quantum dots and their arrays, antidot lattices, nanoribbons, nanotubes, and nanospheres. Their low dimensionality and Dirac-like dispersion enable the emulation of strongly correlated systems and topological phases, especially when engineered at the nanoscale, controlling their geometry and edge structure. For instance, nanoribbons with armchair edge geometries can host topological edge modes and correlated insulating behavior [212, 213], while zigzag-edged ribbons have been shown to realize localized spin-polarized states. On the other hand, antidot lattices — created by carving out regularly spaced holes in graphene sheets — enable the design and control of defect states that can simulate electron spin qubits [214], and more generally allow for the engineering of artificial lattice potentials where collective excitations and flat-band physics emerge. Furthermore, graphene nanostructures coupled to superconductors or ferromagnets offer opportunities to realize Majorana modes and other exotic correlated phases.

Among these diverse architectures, triangular graphene quantum dots (TGQDs) with zigzag edges stand out due to their robust zero-energy states [215]. TGQDs are nanoscale graphene flakes shaped into equilateral triangles. The graphene lattice structure consists of two sublattices, with N_A and N_B carbon atoms. In triangular flakes, a sublattice imbalance occurs such that $N_A \neq N_B$. Flakes of different sizes can be characterized by the number of

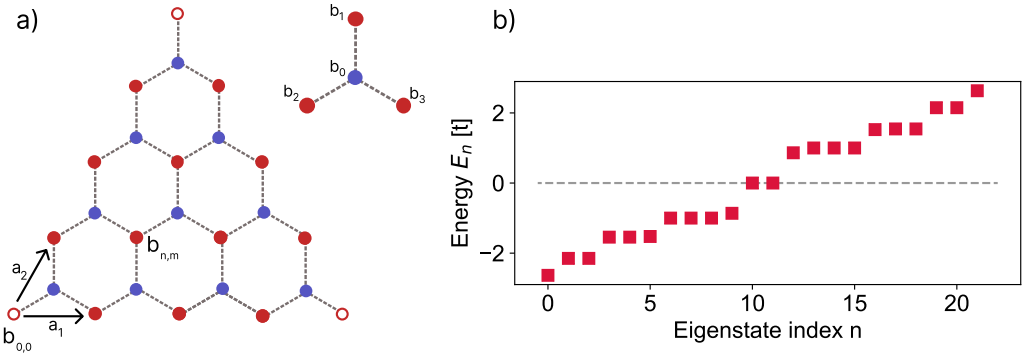

Figure 2.4: (a) Triangulene structure divided into two sublattices with site indices $b_{n,m}$. Empty circles denote auxiliary carbon atoms. (b) Single-particle energy states of the triangulene, dashed line indicates the Fermi energy.

atoms on one edge, denoted by N_{edge}. The total number of carbon atoms is then given by $N = N_{\text{edge}}^2 + 4N_{\text{edge}} + 1$, while the sublattice imbalance is $|N_A - N_B| = N_{\text{edge}} - 1$. Figure 2.3 shows the two smallest TGQDs with $N = 13$ (phenalenyl) and $N = 22$ (triangulene).

Tight-binding calculations of single-particle energy levels within nearest-neighbor approximation reveal a degenerate shell at the Fermi level (Fig. 2.4 b). These degenerate states are localized along the edges of the quantum dot. Importantly, the degeneracy level is directly related to the flake size and scales as $N_0 = N_{\text{edge}} - 1$. To establish this result, we consider the tight-binding Hamiltonian within the nearest-neighbor approximation:

$$H_{\text{TB}} = t \sum_{<i,j>,\sigma} c_{i,\sigma}^{\dagger} c_{j,\sigma}. \tag{2.4}$$

The eigenstates at energy $E = 0$ are solutions of the equation:

$$H_{TB} \left|\psi\right\rangle = 0. \tag{2.5}$$

We begin by examining a fragment of the honeycomb lattice consisting of a single atom from the B sublattice adjacent to three atoms from the A sublattice (Fig. 2.4a). The wavefunction in the p_z basis takes the form:

$$\left|\psi\right\rangle = b_0\phi_z^0 + b_1\phi_z^1 + b_2\phi_z^2 + b_3\phi_z^3. \tag{2.6}$$

Applying the Hamiltonian and projecting onto ϕ_z^0 with b_i as expansion coefficients gives:

$$\langle \phi_z^0 | \, H_{\mathrm{TB}} \, | \psi \rangle = t(b_1 + b_2 + b_3), \tag{2.7}$$

since $\langle \phi_z^0 | \, H_{\mathrm{TB}} \, | \phi_z^i \rangle = t$ for $i = 1, 2, 3$ and vanishes otherwise. Imposing Eq. 2.5 yields $b_1 + b_2 + b_3 = 0$, thus, the sum of coefficients around a given site must vanish for zero-energy states.

We now turn to the 22-atom TGQD. Each A-sublattice site is labeled by integer indices (n, m) corresponding to primitive lattice vectors $\mathbf{a}_1$ and $\mathbf{a}_2$: $R = n\mathbf{a}_1 + m\mathbf{a}_2$. To facilitate recursion, we introduce three auxiliary atoms at the corners (open circles in Fig. 2.4a). Labeling the auxiliary site at the bottom-left as $(0, 0)$, the nearest A sites have coordinates $(0, 1)$ and $(1, 0)$. From the previous result, we express the coefficient $b_{0,1}$ using bottom edge values:

$$b_{0,1} = -b_{0,0} - b_{1,0}. \tag{2.8}$$

Similarly, $b_{1,1} = -(b_{1,0} + b_{2,0})$, leading to a general recurrence:

$$b_{n,1} = -(b_{n,0} + b_{n+1,0}). \tag{2.9}$$

Coefficients on the left edge follow a similar structure, e.g., $b_{0,2} = -(b_{0,1} + b_{1,1}) = -(b_{0,0} + 2b_{1,0} + b_{2,0})$. Potasz et al. showed that all A-sublattice coefficients can be recursively written using only those along the bottom edge [216]. The general expression involves binomial coefficients:

$$b_{n,m} = (-1)^m \sum_{k=0}^{m} \binom{m}{k} b_{n+k,0}. \tag{2.10}$$

To ensure the wavefunction vanishes on all three auxiliary atoms, we set $b_{0,0} = b_{4,0} = b_{0,4} = 0$, reducing the number of independent coefficients to $N_{\mathrm{edge}} - 1$. All other coefficients are linear combinations of these. Applying the same method to the B sublattice shows that its coefficients are determined by $b_{0,0}$, implying that only A-sublattice sites contribute to the zero-energy manifold. Thus, the maximum number of linearly independent eigenstates with $E = 0$ is $N_{\mathrm{deg}} = N_{\mathrm{edge}} - 1$. According to Lieb's theorem [217], for a bipartite lattice at half-filling, the ground-state total spin is determined by the sublattice imbalance $S = \frac{1}{2}|N_A - N_B|$, which in TGQDs leads to a finite spin polarization of the zero-energy manifold [218, 219]. As a result, TGQDs provide a natural setting for realizing localized spin states with tunable total

spin. For example, a 22-atom TGQD possesses $N_{\text{deg}} = 2$ spin-polarized zero-energy states, and its low-energy spectrum effectively simulates an isolated spin-1 object. This makes TGQDs promising building blocks for quantum simulators of spin-n systems.

Modern bottom-up fabrication techniques allow researchers to synthesize graphene flakes with well-defined shapes and atomically precise numbers of carbon atoms [220, 221]. In particular, short chains of connected triangular graphene quantum dots (TGQDs) containing 13 and 22 carbon atoms have been successfully realized on metallic substrates. These structures provide a platform for quantum simulation of one-dimensional spin systems with tunable spin magnitude and coupling geometry. Chains composed of 13-atom TGQDs exhibit a single unpaired zero-energy state per dot, which allows them to simulate spin-1/2 Heisenberg chains. Experimental and theoretical studies have revealed clear signatures of antiferromagnetic coupling between neighboring dots and gapless excitations [222]. Chains constructed from 22-atoms TGQDs simulate antiferromagnetic spin-1 Heisenberg chains and exhibit signatures of Haldane physics, including gapped excitation spectra and emergent spin-1/2 edge states localized at the chain ends, which have been observed experimentally. Local spin excitations can be probed with scanning tunneling microscopy (STM) and spectroscopy (STS) with atomic-scale resolution. Moreover, the STM technique allows coherent spin manipulation in TGQDs, which makes them good candidates for carbon qubits [223].

2.3 Artifcial lattices

Another step toward controlling electronic properties in solid-state physics is the creation of artificial lattices, which can now be engineered with atomic precision using a scanning tunneling microscope (STM) [224]. Originally developed as a tool for high-resolution imaging of metallic surfaces and two-dimensional materials, the STM operates by bringing a sharp metallic tip within a few angstroms of the sample. When a bias voltage is applied, a tunneling current flows between the tip and the surface, with an exponential dependence on their separation. This sensitivity enables precise mapping of atomic positions and the local density of electronic states (LDOS), with energy resolution limited only by thermal broadening and the modulation technique.

Beyond passive imaging, STM offers an active mode of operation, allow-

ing the creation of artificial atoms, molecules, and two-dimensional lattices through atom-by-atom manipulation of adsorbates (adatoms) or vacancies on conducting substrates. This is achieved either by applying voltage pulses that locally modify the potential landscape, or by physically repositioning atoms via mechanical interaction with the tip. A historical demonstration of this capability was performed by Don Eigler in 1989, who famously arranged xenon atoms on a nickel surface to spell the IBM logo [225]. The concept of constructing matter "atom by atom," originally envisioned by Richard Feynman, has thus become a practical reality.

Artificial lattices constructed via STM provide a unique quantum simulation platform, bridging condensed matter physics and quantum engineering. They allow direct and local control over lattice geometry, on-site potential, orbital composition, and inter-site tunneling—parameters that are otherwise fixed in natural materials. By tuning these elements independently, researchers can emulate specific Hamiltonians and study their spectral and spatial properties with unparalleled precision.

The potential of this approach has been exemplified by artificial realizations of tight-binding models with nontrivial band topology. For instance, the Lieb lattice—a two-dimensional structure with a flat band at the Fermi energy—has been realized using two different strategies: chlorine vacancies in a Cl monolayer on Cu(100) [226] and carbon monoxide (CO) molecules placed on Cu(111) [227]. In both platforms, STM spectroscopy revealed Dirac cones and nearly flat bands, with local wavefunction imaging confirming the orbital character of the states. The CO-on-Cu(111) platform, in particular, provides higher tunability, allowing researchers to vary the number and placement of CO molecules at each lattice site. This control was used to implement a multiorbital honeycomb lattice with energy-separated s- and p-like bands [228], enabling orbital-selective probing of band structure and Berry curvature.

While most early STM-based simulations focused on periodic lattices, artificial lattices reveal their full power in exploring non-periodic and aperiodic geometries. Systems such as amorphous networks, quasicrystals with long-range rotational order but no translational symmetry, and fractal geometries can all be assembled site-by-site using STM [229–231]. These architectures are notoriously challenging for conventional band theory, due to the absence of Bloch's theorem and momentum-space analysis. STM quantum simulators thus offer a rare experimental handle on the interplay between electronic localization, symmetry, and topology in such non-crystalline systems.

Despite their versatility, STM-based simulators face important limita-

tions. The electron wavefunctions used to define artificial orbitals are based on surface-state electrons of the underlying metal, which are subject to decoherence from surface-to-bulk scattering [232, 233]. This limits the lifetime and resolution of spectroscopic features. Additionally, strong electronic correlations are typically absent due to the delocalized nature of the wavefunctions and metallic screening, and spin–orbit coupling is weak in conventional metallic substrates [234]. To address these challenges, current efforts focus on integrating substrates with reduced electronic screening, such as ultrathin insulating layers or superconductors, and on engineering artificial spin–orbit coupling via tailored lattice designs and magnetic adatoms [235–237]. These developments aim to extend the range of quantum phases accessible with artificial lattices, including topological superconductors, Mott insulators, and quantum spin liquids.

Chapter 3

Methodology

3.1 Exact diagonalization method

Analyzing strongly correlated quantum systems requires explicit treatment of electron–electron interactions. The most straightforward approach is to calculate the eigenstates of the full Hamiltonian. Exact diagonalization provides precise access to ground-state properties, excitation spectra, correlation functions, and entanglement measures [238, 239]. However, the dimension of the Hilbert space grows exponentially with system size, which quickly limits the applicability of this method. To manage this exponential growth, symmetries such as particle number conservation, spin, or momentum are typically exploited to block-diagonalize the Hamiltonian and reduce its effective size. In practice, the Hamiltonian matrix is extremely sparse, with most elements equal to zero, allowing for efficient storage and numerical manipulation using sparse matrix techniques. When such optimization is insufficient for larger problems, iterative algorithms like the Lanczos or Davidson methods are employed to find a few low-energy eigenstates without computing the full spectrum [138, 139].

3.1.1 Construction of the basis

The first step toward the exact diagonalization method is to write the many-body Hamiltonian given in the second quantization formalism as a sparse Hermitian matrix. Let's consider the fermionic Hubbard Hamiltonian:

$$H = -t \sum_{<i,j>,\sigma} \left(c^{\dagger}_{i\sigma} c_{j\sigma} + H.c. \right) + U \sum_{i} n_{i\uparrow} n_{i\downarrow}. \tag{3.1}$$

Assuming the system to be a chain with length L, the full Hilbert space has dimension 4^L. To simplify the problem, one can exploit symmetries of the Hamiltonian. When an operator A commutes with the Hamiltonian H, they share a common set of eigenstates. This allows the Hilbert space to be decomposed into invariant subspaces labeled by the quantum numbers associated with the symmetry. In such a basis, the Hamiltonian becomes block-diagonal and does not couple states from different subspaces. Each block can then be treated independently, which significantly reduces the effective dimensionality of the problem.

The Hubbard Hamiltonian possesses few intrinsic symmetries that can be used to simplify the numerical implementation of the exact diagonalization method:

- Conservation of the particle number: the Hamiltonian commutes with the total particle number operator $N_e = \sum_{i,\sigma} n_{i,\sigma}$.

$$[N_e, H] = N_e H - H N_e \tag{3.2}$$

$$N_e H = \sum_{k,\sigma'} \left(-t \sum_{<i,j>,\sigma} c^{\dagger}_{k\sigma'} c_{k\sigma'} c^{\dagger}_{i\sigma} c_{j\sigma} + c^{\dagger}_{k\sigma'} c_{k\sigma'} c^{\dagger}_{j\sigma} c_{i\sigma} \right)$$

$$+ \sum_{k,\sigma'} \left(U \sum_{i} c^{\dagger}_{k\sigma'} c_{k\sigma'} c^{\dagger}_{i\uparrow} c_{i\uparrow} c^{\dagger}_{i\downarrow} c_{i\downarrow} \right)$$

$$= \sum_{k,\sigma'} \left(-t \sum_{<i,j>,\sigma} c^{\dagger}_{i\sigma} c_{j\sigma} + c^{\dagger}_{j\sigma} c_{i\sigma} - c^{\dagger}_{k\sigma'} c^{\dagger}_{i\sigma} c_{k\sigma'} c_{j\sigma} - c^{\dagger}_{k\sigma'} c^{\dagger}_{j\sigma} c_{k\sigma'} c_{i\sigma} \right)$$

$$+ \sum_{k,\sigma'} \left(U \sum_{i} -c^{\dagger}_{i\uparrow} c^{\dagger}_{i\downarrow} c_{i\uparrow} c_{i\downarrow} + c^{\dagger}_{i\downarrow} c^{\dagger}_{i\uparrow} c_{i\uparrow} c_{i\downarrow} - c^{\dagger}_{k\sigma'} c^{\dagger}_{i\uparrow} c^{\dagger}_{i\downarrow} c_{k\sigma'} c_{i\uparrow} c_{i\downarrow} \right)$$

$$H N_e = \sum_{k,\sigma'} \left(-t \sum_{<i,j>,\sigma} c^{\dagger}_{i\sigma} c_{j\sigma} + c^{\dagger}_{j\sigma} c_{i\sigma} - c^{\dagger}_{i\sigma} c^{\dagger}_{k\sigma'} c_{j\sigma} c_{k\sigma'} - c^{\dagger}_{j\sigma} c^{\dagger}_{k\sigma'} c_{i\sigma} c_{k\sigma'} \right)$$

$$+ \sum_{k,\sigma'} \left(U \sum_{i} -c^{\dagger}_{i\uparrow} c^{\dagger}_{i\downarrow} c_{i\uparrow} c_{i\downarrow} + c^{\dagger}_{i\uparrow} c^{\dagger}_{i\downarrow} c_{i\downarrow} c_{i\uparrow} - c^{\dagger}_{i\uparrow} c^{\dagger}_{i\downarrow} c^{\dagger}_{k\sigma'} c_{i\uparrow} c_{i\downarrow} c_{k\sigma'} \right)$$

$$[N_e, H] = 0$$

- SU(2) spin symmetry: the Hamiltonian commutes with $\alpha = x, y, z$ components of the total spin operator $S^\alpha = \frac{1}{2}\sum_i \sum_{\mu,\nu} c^\dagger_{i\mu}\sigma^\alpha_{\mu\nu}c_{i\nu}$.
- For the periodic boundary condition, the model has translational symmetry.
- For an even number of lattice sites, the model has particle-hole symmetry.

From the numerical point of view, the most important are conservation of the total particle number N and the S^z component of spin, which is equivalent to the conservation of the number of particles with spin up and down separately since $S^z = \frac{1}{2}(N_\uparrow - N_\downarrow)$ and $N = N_\uparrow + N_\downarrow$.

Then the full problem of diagonalizing the Hubbard Hamiltonian can be divided into sectors with fixed numbers $N_\uparrow$ and $N_\downarrow$. As an example, we can focus on the chain with length $L = 4$, and the sector with fixed particle numbers $N = 4$. There are 74 possible basis states, but we can further reduce this number by treating subspaces with different S^z values separately, as shown in the Table 3.1.1. It is convenient to use integers in a bitstring form to encode basis states [240], where each site corresponds to a specific bit in an integer. A bit value of 1 indicates the presence of a fermion with a given spin at that site, while 0 denotes its absence. To do this, we need to order creation operators by spins first and then by lattice sites. Sites occupied by $\uparrow$-spins are denoted by one four-bit integer number (equal to index i) and sites with $\downarrow$-spins by a second (index j). For example:

$$c^\dagger_{1\uparrow}c^\dagger_{2\uparrow}c^\dagger_{2\downarrow}c^\dagger_{3\downarrow}\left|0\right\rangle \rightarrow [(1100)_2, (0110)_2] \rightarrow \left|(12, 6)\right\rangle \tag{3.3}$$

This state in the constructed basis has indices $i = 12$, $j = 6$. Such notation allows the use of binary operations, which enhance the performance of the code.

3.1.2 Hamiltonian matrix elements

The kinetic part of the Hamiltonian involves hopping of fermions between neighboring sites and must preserve the antisymmetric nature of fermionic wavefunctions. In the bitstring formalism, hopping corresponds to flipping occupation bits at two sites, removing a fermion from one site and adding it to another. However, because fermions anticommute, this process introduces

S^z	$N_\uparrow$	$N_\downarrow$	n
0	2	2	36
1	3	1	18
-1	1	3	18
2	4	0	1
-2	0	4	1

Table 3.1: Number of basis vectors n in subspaces with different S^z for N=4 fermions on L=4 sites.

a phase determined by the parity of the number of fermions passed during the hopping operation. This parity is computed by counting the number of occupied sites between the origin and destination of the hop, which mimics the string of Jordan–Wigner phase factors in one-dimensional systems. In practice, this is implemented efficiently by bitwise operations that count the number of ones in specific ranges of the bitstring. This ensures correct antisymmetry of the fermionic wavefunction and allows efficient construction of the Hamiltonian matrix elements without explicitly working in a second-quantized operator algebra. The same procedure is independently applied to spin-up and spin-down sectors, preserving total particle number and taking into consideration the Pauli exclusion principle for fermions.

For example, applying the kinetic part of the Hubbard Hamiltonian $\hat{T} = -t \sum_{<i,j>,\sigma} \left(c^\dagger_{i\sigma} c_{j\sigma} + H.c \right)$ to the state $|(12,6)\rangle$ results in 4 possible hoppings:

$$\begin{aligned} \hat{T}\left[(1100)_2,(0110)_2\right] &= t\left[(0101)_2,(0110)_2\right] - t\left[(1010)_2,(0110)_2\right] \\ &\quad - t\left[(1100)_2,(1010)_2\right] - t\left[(1100)_2,(0101)_@\right] \\ &= t\,|(5,6)\rangle - t\,|(10,6)\rangle - t\,|(12,10)\rangle - t\,|(12,5)\rangle \end{aligned} \tag{3.4}$$

Each term corresponds to a single fermion hopping between neighboring sites, with signs determined by the parity counting. Depending on the system size, matrix indices for these resulting states can be found either by scanning the full basis list or using hash maps or binary search to improve performance.

The interaction term of the Hubbard Hamiltonian is more straightforward to implement, as it acts diagonally in the occupation number basis. The interaction energy is given by $\hat{V} = \sum_i n_{i\uparrow} n_{i\downarrow}$ and for each basis state, the number of doubly occupied sites (sites where both spin-up and spin-down bits are set) can be found with a bitwise AND logic operation of the two

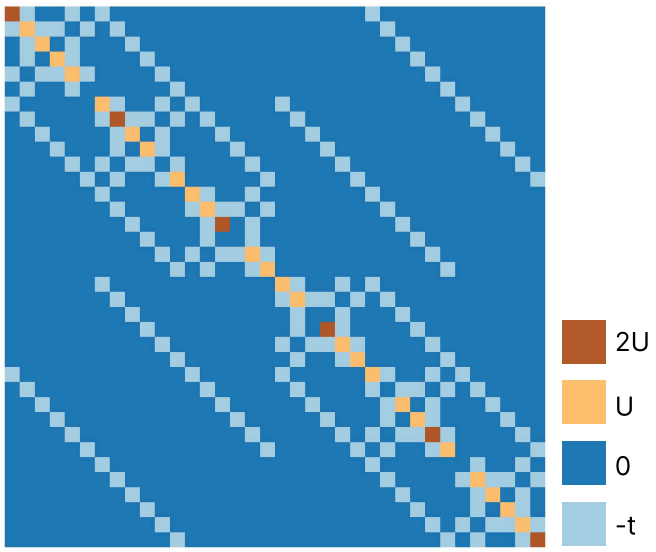

Figure 3.1: Matrix elements of Hubbard Hamiltonian for L = 4, $N_\uparrow = N_\downarrow = 2$.

bitstrings. For our example state $|(12, 6)\rangle$, this yields one site with double occupancy, contributing a diagonal matrix element:

$$\hat{V}\left[(1100)_2, (0110)_2\right] = U\left[(1100)_2, (0110)_2\right] = U\,|(12, 6)\rangle \tag{3.5}$$

Altogether, the Hamiltonian matrix can be efficiently constructed using bit-level operations for both hopping and interaction terms.

3.1.3 Translation symmetry

When the system has periodic boundary conditions and translational invariance, the Hamiltonian $\hat{H}$ commutes with the translation operator $\hat{\mathcal{T}}$. As a result, crystal momentum is conserved, and the lattice quasi-momentum k becomes a good quantum number. The Hilbert space can then be decomposed into invariant subspaces labeled by k, and the Hamiltonian takes block-diagonal form. Each block corresponds to a fixed momentum sector, and the full Hamiltonian is a direct sum of these symmetry-reduced blocks [241].

The basis vectors from each translational symmetry block are eigenstates of the translational symmetry operator $\hat{\mathcal{T}}$, which can be constructed using

	Bitstring state	Integer index
0	1100	12
1	1010	10
2	1001	9
3	0011	3
4	0101	5
5	0110	6

Table 3.2: Spin-↑ configurations with two particles on L=4 sites.

the momentum-space projection operator:

$$P_k = \frac{1}{N}\sum_{j=0}^{L-1} e^{2\pi ijk/L}\mathcal{T}^j. \tag{3.6}$$

The operator P_k project an arbitrary basis state $|n\rangle$ onto a k-momentum eigenstate. Applying $\hat{\mathcal{T}}$ to the projected state yields:

$$\hat{\mathcal{T}}P_k\,|n\rangle = \frac{1}{N}\sum_{j=0}^{L-1} e^{2\pi ij/L}\mathcal{T}^{j+1}\,|n\rangle = e^{-2\pi ik/L}P_k\,|n\rangle\,. \tag{3.7}$$

showing that $P_k\,|n\rangle$ is indeed an eigenstate of $\hat{\mathcal{T}}$ with eigenvalue $e^{-2\pi ik/L}$, corresponding to momentum $2\pi k/L$. On the ring with L sites, repeating translation by one site L times results in returning to the origin, so $\mathcal{T}^L = 1$, which also implies $e^{-2\pi ik} = 1$. From this property, we find a closed set of k values to be integers modulo L: $k = 0, 1, \ldots, (L-1)$.

To illustrate this, we first examine the spin-↑ sector of two particles on four lattice sites. Each bitstring representing occupied sites is indexed in Table 3.2. We can identify all translationally equivalent states by generating the set $\{|n\rangle\,, \mathcal{T}^1\,|n\rangle\,, \mathcal{T}^2\,|n\rangle\,, \mathcal{T}^3\,|n\rangle\}$. For example, consider the state $|12\rangle = |1100\rangle$:

$$\begin{aligned}\mathcal{T}^1\,|12\rangle &= |6\rangle \\ \mathcal{T}^2\,|12\rangle &= |3\rangle \\ \mathcal{T}^3\,|12\rangle &= |9\rangle\end{aligned} \tag{3.8}$$

This collection of states $\mathcal{O}_1^{\uparrow} = \{|12\rangle\,, |9\rangle\,, |6\rangle\,|3\rangle\}$ forms a translational orbit, representing a class of states that will contribute to a single momentum

eigenstate. Each orbit is uniquely described by a canonical representative, chosen arbitrarily from its elements. We can immediately notice that two states $|5\rangle$ and $|10\rangle$ are not included in this orbit. They are connected by translation $\hat{T}^1 |10\rangle = |5\rangle$ and form second orbit $\mathcal{O}_2^{\uparrow}\{|10\rangle, |5\rangle\}$.

Science $\mathrm{N}_{\uparrow} = \mathrm{N}_{\downarrow}$, the orbits for spin-$\downarrow$ states are the same as for spin-$\uparrow$ particles. To build the basis for the full Hubbard model, we consider pairs $(n_{\uparrow}, m_{\downarrow})$, and apply simultaneous translation to both components. This yields 10 inequivalent orbits in the combined Hilbert space:

$$
\begin{aligned}
\mathcal{O}_1 &= \{|(12,12)\rangle, |(9,9)\rangle, |(3,3)\rangle, |(6,6)\rangle\} \\
\mathcal{O}_2 &= \{|(6,5)\rangle, |(3,10)\rangle, |(9,5)\rangle, |(12,10)\rangle\} \\
\mathcal{O}_3 &= \{|(6,12)\rangle, |(3,6)\rangle, |(9,3)\rangle, |(12,9)\rangle\} \\
\mathcal{O}_4 &= \{|(6,9)\rangle, |(3,12)\rangle, |(9,6)\rangle, |(12,3)\rangle\} \\
\mathcal{O}_5 &= \{|(12,5)\rangle, |(6,10)\rangle, |(3,5)\rangle, |(9,10)\rangle\} \\
\mathcal{O}_6 &= \{|(12,6)\rangle, |(6,3)\rangle, |(3,9)\rangle, |(9,6)\rangle\} \\
\mathcal{O}_7 &= \{|(10,12)\rangle, |(5,9)\rangle, |(10,3)\rangle, |(5,6)\rangle\} \\
\mathcal{O}_8 &= \{|(5,12)\rangle, |(10,6)\rangle, |(5,3)\rangle, |(10,9)\rangle\} \\
\mathcal{O}_9 &= \{|(10,10)\rangle, |(12,12)\rangle\} \\
\mathcal{O}_{10} &= \{|(10,12)\rangle, |(12,10)\rangle\}
\end{aligned}
$$

During the construction of orbits and applying translations, we need to take into consideration the change of fermionic sign, particularly when the translation operator permutes fermionic operators across boundaries. For each canonical representative of orbit $\mathcal{O}_n$, we can construct a momentum eigenstate Ψ_1^k using the projection operator Eq. 3.6. For example, for $k = 0$ and orbit $\mathcal{O}_1$ we obtain :

$$
\Psi_1^{k=0} = \frac{1}{2}\left(|(12,12)\rangle + |(9,9)\rangle + |(3,3)\rangle + |(6,6)\rangle\right) \tag{3.9}
$$

Note that the projected states $|\Psi_n^k\rangle$ must be orthonormalized, since distinct orbits may overlap after projection. This is typically done via the Gram–Schmidt process or by constructing the overlap matrix.

After projecting the orbit representatives into fixed-k sectors, we obtain a symmetry-adapted basis in which the Hamiltonian becomes block-diagonal. Beyond computational speed-up, resolving the Hamiltonian in momentum sectors allows direct access to dispersion relations $E(k)$, identification of symmetry-protected states, and classification of excitations by momentum.

3.1.4 The Lanchos algorithm

One of the simplest and most effective methods for computing extremal eigenvalues of large, sparse matrices, typically the ground-state energy and low-lying excitations, is the Lanczos algorithm [242]. It is an iterative procedure that operates in Krylov subspaces and avoids explicit construction and storage of the full Hamiltonian matrix.

In general, the ground state Ψ_{GS} and its energy can be found from the variational principle. For any Hermitian Hamiltonian H, one can define the energy functional:

$$E\left[\Psi\right] = \frac{\langle\Psi| H |\Psi\rangle}{\langle\Psi|\Psi\rangle}, \tag{3.10}$$

which is minimized when $\Psi = \Psi_{GS}$. The steepest ascent direction of this functional, starting from the random state or physically motivated initial state $|\Psi\rangle$, is given by its functional derivative:

$$\frac{\delta E\left[\Psi\right]}{\delta |\Psi\rangle} = \frac{H |\Psi\rangle - E\left[\Psi\right] |\Psi\rangle}{\langle\Psi|\Psi\rangle} = |\Psi_\alpha\rangle \tag{3.11}$$

By moving in the opposite direction, one obtains the state with lower energy $E\left[\Psi - \gamma\Psi_\alpha\right] < E\left[\Psi\right]$ for any small $\gamma > 0$.

The minimum energy can be approximated by diagonalizing the Hamiltonian in the two-dimensional subspace spanned by vectors $|\Psi\rangle$ and $|\Psi_\alpha\rangle = H |\Psi\rangle$. First, the initial state is normalized:

$$|a_0\rangle = \frac{|\Psi\rangle}{\langle\Psi|\Psi\rangle}. \tag{3.12}$$

Next, one orthogonalizes the vector $H |\Psi\rangle$ with respect to $|a_0\rangle$:

$$|\tilde{a}_1\rangle = H |a_0\rangle - |a_0\rangle \langle a_0| H |a_0\rangle , \tag{3.13}$$

and normalizes it to obtain $|a_1\rangle = |\tilde{a}_1\rangle / \langle\tilde{a}_1|\tilde{a}_1\rangle$. This yields the recurrence relation:

$$H |a_0\rangle = \beta_1 |a_1\rangle + \alpha_0 |a_0\rangle \tag{3.14}$$

where $\alpha_n = \langle a_n| H |a_n\rangle$ and $\beta_1^2 = \langle\tilde{a}_1|\tilde{a}_1\rangle$. The Hamiltonian in this subspace is represented by a 2×2 matrix:

$$H_{|a_0\rangle,|a_1\rangle} = \begin{pmatrix} \alpha_0 & \beta_1 \\ \beta_1 & \alpha_1 \end{pmatrix} \tag{3.15}$$

This procedure can be repeated iteratively, using the lowest eigenstate of each 2×2 subspace as the new starting vector. This is the so-called steepest descent method.

In general optimization problems, a known drawback of steepest descent methods is the possibility of converging to a local minimum. However, for quantum systems described by Hermitian Hamiltonians, the variational energy functional has a unique global minimum at the ground state, ensuring efficient convergence.

Repeating the steepest descent method $N-1$ times is equivalent to repeatedly applying the Hamiltonian to the initial state. Rather than diagonalizing 2×2 matrices in each iteration, it is more convenient to first construct a sequence of vectors $H^n |\Psi_0\rangle$. After orthogonalization of those states against each other, they span a Krylov subspace:

$$\mathcal{K}_N = \text{span}\{|\psi_0\rangle, H|\psi_0\rangle, H^2|\psi_0\rangle, \ldots, H^{(N-1)}|\psi_0\rangle\}.$$

In this subspace, the Hamiltonian is represented by a real symmetric tridiagonal matrix:

$$\tilde{H}_{K_N} = \begin{pmatrix} \alpha_0 & \beta_1 & 0 & \ldots & \ldots & 0 \\ \beta_1 & \alpha_1 & \beta_2 & 0 & \ldots & 0 \\ \vdots & \vdots & \vdots & \vdots & \ddots & \vdots \\ 0 & 0 & \ldots & \beta_{N-1} & \alpha_{N-2} & \beta_{N-1} \\ 0 & \ldots & \ldots & 0 & \beta_{N-1} & \alpha_{N-1} \end{pmatrix} \tag{3.16}$$

After a relatively small number of iterations, the lowest eigenvalues of this matrix give us a good approximation to the ground-state energy. The ground-state wavefunction is given by:

$$|\tilde{\Psi}_{GS}\rangle = \sum_{j=0}^{N-1} u_j |\alpha_j\rangle . \tag{3.17}$$

where u_j are components of the lowest eigenvector of $\tilde{H}_{K_N}$.

When the Lanczos algorithm is applied within a fixed symmetry sector, such as a definite momentum k, spin S^z, or particle number, the resulting eigenstates inherit those symmetries. This not only reduces the computational cost (by lowering the Hilbert space dimension) but also ensures that observables and eigenstates respect the physical symmetries of the system.

3.2 Density Matrix Renormalization Group

The density matrix renormalization group (DMRG) is one of the most widely used numerical methods for determining ground states of low-dimensional, strongly correlated quantum systems. It originated as an improvement over the real-space renormalization group (RSRG), which aimed to reduce the degrees of freedom by projecting onto effective low-energy subspaces [243, 244]. However, in contrast to RSRG, which suffers from poor accuracy and boundary artifacts, DMRG makes use of density matrices to retain the most relevant states, leading to significantly improved results.

In the RSRG approach, one begins with an initial subsystem (or "block") of length l, described by Hamiltonian H_S acting on an M-dimensional Hilbert space. The block is then doubled in size, resulting in a new compound block of length $2l$ with a Hilbert space of dimension M^2. After diagonalizing the Hamiltonian of the enlarged block, the lowest-energy M eigenstates are selected to define a reduced Hilbert space. This procedure is repeated iteratively to grow the system [245]. However, such an approach performs poorly even for simple test cases, such as a single particle in a box, due to incorrect boundary conditions and the accumulation of truncation errors.

As an alternative, White in 1992 [144] introduced the DMRG algorithm for one-dimensional systems, which reformulates the truncation process using the reduced density matrix of a subsystem. Unlike the RSRG method, which has exponentially fast growth, the DMRG procedure grows linearly (for gapped 1D Hamiltonians) and, what is more critical, solves the problem of false boundary conditions by embedding the system in an environment of the same size, mimicking the thermodynamic limit.

In its original form (the infinite-system DMRG), the algorithm consists of the following steps:

0. The algorithm starts with a small lattice system (block) S consisting of $\mathcal{N}$ sites. The Hilbert space of the block has dimension M_S and contains states $\{|m_S\rangle\}$. The matrix elements of the Hamiltonian $H_{\mathcal{N}}$ are defined as $\langle m_S| H |m'_S\rangle$. Block S is embedded in environment E of the same size to mimic the thermodynamic limit.

1. Now, a single site with local basis $\{|\sigma_S\rangle\}$ is added to block S, forming the new system S', which lives in the Hilbert space with dimension $N_S = M_S N_\sigma$. The merged basis contains product states $\{|m_S\sigma\rangle\} =$

$\{|m_S\rangle |\sigma_S\rangle\}$. The same procedure is performed with the environment, so the final result is the superblock with $2\mathcal{N}+2$ sites. Its Hilbert space has dimension $N^S N^E$.

2. Find the ground state $|\psi_0\rangle$ of the superblock Hamiltonian $H_{2\mathcal{N}+2}$ by the sparse-matrix diagonalization method, for example, the Lanczos algorithm.

3. The reduced density matrix $\hat{\rho} = \mathrm{Tr}_E |\phi_0\rangle \langle\phi_0|$ has N^S eigenvalues p_α and orthonormal eigenstates $|p_\alpha\rangle$, which satisfy conditions $\sum_\alpha p_\alpha = 1$ and $p_\alpha \geq 0$. The basis S' can be obtained by keeping the M^S number of eigenstates associated with the largest eigenvalues p_α.

4. Define the rectangular matrix T of size $N_S \times M_S$ as $T_{ij} = \langle m_S \sigma | p_\alpha^{tr} \rangle$. Next, perform the transformation of the Hamiltonian to the reduced M_S-state basis $H_{\mathcal{N}+1}^{tr} = T^\dagger H_{\mathcal{N}+1} T$. Assign $H_{\mathcal{N}+1}^{tr}$ as $H_{\mathcal{N}+1}$ for the S' system and repeat the procedure for the environment.

5. Restart from step 1 and proceed until the desired length is reached.

In later studies, this procedure was improved for better performance by incorporating Abelian symmetries and changing the truncation basis mechanism.

While the infinite-system DMRG is effective for gapped systems near half-filling, it can become unreliable near critical points or in systems with open boundary conditions. In those cases, better results are obtained with the finite-system DMRG. In this variant, the system is first grown to a fixed length L, after which the DMRG iterations proceed by *sweeping*: one block grows while the other shrinks, until the minimal size is reached, then the direction is reversed. Repeated sweeps refine the approximation of the ground state.

In modern implementations, the DMRG algorithm integrates tensor network methods by representing quantum states and operators as matrix product states (MPS) and matrix product operators (MPO) [246, 247]. In such formulation, the DMRG is a variational method, which iteratively optimizes the physical state in the form of the MPS. This approach takes advantage of the compact representation of quantum states offered by MPS, which allows the algorithm to capture the essential degrees of freedom efficiently. By employing MPS for states and MPO for operators, DMRG can effectively exploit the system's locality and entanglement characteristics, thus significantly reducing computational complexity while preserving high accuracy.

3.2.1 Matrix Product States

The exact representation of many-body wavefunctions in quantum systems requires storing exponentially many coefficients. However, in low-dimensional systems with limited entanglement (e.g., gapped 1D systems), ground states often obey the area law for entanglement entropy. Matrix Product States (MPS) provide a compact representation for such states, making them a foundational tool in modern DMRG [248, 249].

We consider a 1D quantum system with N sites, each with local Hilbert space spanned by $\{|j_n\rangle\}_{j_n=1}^{d}$. Any pure state can be written as

$$|\psi\rangle = \sum_{j_1,\ldots,j_N} \psi_{j_1,\ldots,j_N} |j_1,\ldots,j_N\rangle . \tag{3.18}$$

The main concept behind the MPS is an ansatz that amplitudes $\psi_{j_1,\ldots,j_N}$ of the wave function can be decomposed into a product of matrices by iterative singular value decomposition (SVD) [145]. The SVD method decomposes an arbitrary rectangular matrix M with size $N_A \times N_B$ into:

$$M = USV^{\dagger}, \tag{3.19}$$

where U is a unitary matrix with orthonormal columns and dimension $N_A \times \min(N_A, N_B)$, matrix S of size $\min(N_A, N_B) \times \min(N_A, N_B)$ and its diagonal non-negative values are so-called singular values $S_{aa} = s_a$, and $V^{\dagger}$ is unitary matrix with dimensions $\min(N_A, N_B) \times N_B$ and orthonormal rows. Coefficients of the many-body state $|\Psi\rangle$ can be reshaped into a matrix A of dimension $d \times d^{N-1}$:

$$A_{j_1,(j_2\ldots j_N)} = \psi_{j_1\ldots j_N}. \tag{3.20}$$

The next step is performing the SVD of A, which gives us:

$$\psi_{j_1\ldots j_N} = A_{j_1,(j_2\ldots j_N)} = \sum_{\alpha_1}^{r_1} U_{j_1,\alpha_1} S_{\alpha_1,\alpha_1} V^{\dagger}_{\alpha_1,(j_2\ldots j_N)}. \tag{3.21}$$

Matrices S and V can be multiplied, and the resulting matrix can be expressed in form analogous to Eq 3.20: $S_{\alpha_1,\alpha_1} V^{\dagger}_{\alpha_1,(j_2\ldots j_N)} = A_{(\alpha_1 j_2),(j_3\ldots j_N)}$ with size $r_1 d \times d^{N-1}$. The unitary matrix U is then decomposed into a set of row vectors M^{j_1} of size d. In the result:

$$\psi_{j_1\ldots j_N} = \sum_{\alpha_1}^{r_1} M^{j_1}_{\alpha_1} A_{(\alpha_1 j_2),(j_3\ldots j_N)}. \tag{3.22}$$

The same procedure is carried again for $A_{(\alpha_1 j_2),(j_3 \ldots j_N)}$:

$$\psi_{j_1 \ldots j_N} = \sum_{\alpha_1}^{r_1} \sum_{\alpha_2}^{r_2} M^{j_1}_{\alpha_1} U_{(\alpha_1 j_2),\alpha_2} S_{\alpha_2,\alpha_2} V^{\dagger}_{\alpha_2,(j_3 \ldots j_N)} = \sum_{\alpha_1}^{r_1} \sum_{\alpha_2}^{r_2} M^{j_1}_{\alpha_1} M^{j_2}_{\alpha_1,\alpha_2} \psi_{(\alpha_2,j_3)(j_4 \ldots j_N)}. \tag{3.23}$$

where $M^{j_2}_{\alpha_1,\alpha_2}$ is a set of matrices M^{j_2} of dimension $r_1 \times r_2$. Further iterative SVD procedures give:

$$\psi_{j_1 \ldots j_{N-1}} \sum_{\alpha_1,\ldots,\alpha_{N-1}} M^{j_1}_{\alpha_1} M^{j_2}_{\alpha_1,\alpha_2} \ldots M^{j_{N-1}}_{\alpha_{N-2},\alpha_{N-1}}. \tag{3.24}$$

The corresponding matrix product state is then:

$$|\psi\rangle = \sum_{i_1,\ldots,i_N} \sum_{\alpha_1,\ldots,\alpha_{N+1}} M^{i_1}_{\alpha_1 \alpha_2} M^{i_2}_{\alpha_2 \alpha_3} \ldots M^{i_N}_{\alpha_N \alpha_{N+1}} |i_1, i_2, \ldots, i_N\rangle \,, \tag{3.25}$$

where $i_n = 1, \ldots, d$ label local basis states, and $\alpha_n = 1, \ldots, \chi_n$ are virtual bond indices connecting neighboring sites. The matrices M^{i_n} have dimensions $\chi_n \times \chi_{n+1}$, with χ_n referred to as the bond dimension at site n. For the generic state, we have different sets of matrices on each site. The graphical representation of the MPS is shown in Fig. 3.2(a).

In the trivial case, where the wavefunction is a product state $|\psi\rangle = |\phi^1\rangle \otimes |\phi^2\rangle \otimes \cdots \otimes |\phi^N\rangle$, it can be easily represented as the MPS with bond dimension $\chi_n = 1$ and 1×1 matrices $M^{i_n} = \phi^n_{i_n}$. Such a simple form of the MPS results from the absence of entanglement.

3.2.2 The AKLT state in the MPS representation

A non-trivial example is provided by the Affleck-Kennedy-Lieb-Tasaki (AKLT) model [80], defined by the spin-1 Hamiltonian:

$$H_{AKLT} = \sum_i \bar{S}_i \bar{S}_{i+1} + \frac{1}{3} (\bar{S}_i \bar{S}_{i+1})^2 \tag{3.26}$$

Its ground state is a valence bond solid (VBS), in which spins form an ordered pattern of singlet pairs (valence bonds). It can be obtained by decomposing the spin-1 at each site into two spin-1/2, which are then connected by a single valence bond S_0 with neighboring sites [250]. To construct such a

ground state for a chain of L spin-1 sites, we start with a product of singlet pairs on the $2L$ spin-$\frac{1}{2}$ chain:

$$|\Phi_S\rangle = \bigotimes_{x=1}^{L} \frac{1}{\sqrt{2}}(|\uparrow_{x,R}\rangle |\downarrow_{x+1,L}\rangle - |\downarrow_{x,R}\rangle |\uparrow_{x+1,L}\rangle), \tag{3.27}$$

where x are indices of the physical spin-1 site, and L/R denotes left/right spin-$\frac{1}{2}$ at site x. Local states in such a tensor product are not correlated. To obtain a correlated ground state of the AKLT Hamiltonian, we need to apply the symmetrization operator, which projects singlet bonds back onto the triplet subspace:

$$|\Phi_{VBS}\rangle = (\bigotimes_{x=1}^{L} \mathrm{S}_x) |\Phi_S\rangle . \tag{3.28}$$

The symmetrization operator $\mathbb{S}$ is defined as:

$$\begin{aligned}
\mathbb{S}|\downarrow\uparrow\rangle &= \frac{1}{2}(|\uparrow\downarrow\rangle + |\downarrow\uparrow\rangle) = \frac{1}{\sqrt{2}}|T_0\rangle , \\
\mathbb{S}|\uparrow\downarrow\rangle &= \frac{1}{2}(|\uparrow\downarrow\rangle + |\downarrow\uparrow\rangle) = \frac{1}{\sqrt{2}}|T_0\rangle , \\
\mathbb{S}|\uparrow\uparrow\rangle &= |\uparrow\uparrow\rangle = |T_+\rangle , \\
\mathbb{S}|\downarrow\downarrow\rangle &= |\downarrow\downarrow\rangle = |T_-\rangle .
\end{aligned} \tag{3.29}$$

For example, for two spin-1 sites with open boundary conditions, we have four degenerate VBS ground states:

$$\begin{aligned}
|VBS_{\downarrow\downarrow}\rangle &= \mathbb{S}|\downarrow, S_0, \downarrow\rangle , \\
|VBS_{\uparrow\downarrow}\rangle &= \mathbb{S}|\uparrow, S_0, \downarrow\rangle , \\
|VBS_{\downarrow\uparrow}\rangle &= \mathbb{S}|\downarrow, S_0, \uparrow\rangle , \\
|VBS_{\uparrow\uparrow}\rangle &= \mathbb{S}|\uparrow, S_0, \uparrow\rangle ,
\end{aligned} \tag{3.30}$$

where $S_0 = \frac{1}{\sqrt{2}}(|\uparrow_{1,R}\rangle |\downarrow_{2,L}\rangle - |\downarrow_{1,R}\rangle |\uparrow_{2,L}\rangle)$ is a valence bond between sites $x = 1$ and $x = 2$. After symmetrization, our VBS states are:

$$\begin{aligned} |VBS_{\downarrow\downarrow}\rangle &= \frac{1}{2}(|T_0 T_-\rangle - |T_- T_0\rangle), \\ |VBS_{\uparrow\downarrow}\rangle &= \frac{1}{2}(|T_0 T_0\rangle - |T_- T_+\rangle), \\ |VBS_{\downarrow\uparrow}\rangle &= \frac{1}{2}(|T_+ T_-\rangle - |T_0 T_0\rangle), \\ |VBS_{\uparrow\uparrow}\rangle &= \frac{1}{2}(|T_+ T_0\rangle - |T_0 T_+\rangle). \end{aligned} \tag{3.31}$$

Those states are the lowest eigenvalues of the AKLT Hamiltonian for $L = 2$.

When the ends of the chain are glued together (periodic boundary conditions), the ground state is unique and can be written as the MPS in the form:

$$|\Psi\rangle_{AKLT} = \sum_{\sigma_1,\sigma_2,\ldots,\sigma_N} \mathrm{Tr}(M^{\sigma_1} \ldots M^{\sigma_N}) |\sigma_1, \ldots, \sigma_N\rangle . \tag{3.32}$$

The explicit form of the M matrices follows directly from the valence bond construction. In the VBS state, the bond between sites x and $x + 1$ can be denoted with the index α_{x+1}, which is equal to $\alpha_{x+1} = 1$, when in expansion of the product Eq.3.27 we choose on the bond $\frac{1}{\sqrt{2}} |\uparrow_{x,R}\downarrow_{x+1,L}\rangle$, and $\alpha_{x+1} = 1$ for $-\frac{1}{\sqrt{2}} |\downarrow_{x,R}\uparrow_{x+1,L}\rangle$. The configuration of spin-1's $\sigma = (\sigma^1, \ldots, \sigma_L)$ is uniquely determined by the sequence of bond indices $\alpha_1, \ldots, \alpha_L$. For one site σ^x, three possible local states correspond to four choices of bond indices:

$$\begin{aligned} &\sigma^x = 1 \quad (|\uparrow_{x,L}\uparrow_{x,R}\rangle) \quad \text{for} \quad \alpha_x = 2, \alpha_{x+1} = 1, \\ &\sigma^x = 0 \quad (|\uparrow_{x,L}\downarrow_{x,R}\rangle , |\downarrow_{x,L}\uparrow_{x,R}\rangle) \quad \text{for} \quad \alpha_x = \alpha_{x+1} = 1 \quad \text{or} \quad \alpha_x = \alpha_{x+1} = 2, \\ &\sigma^x = -1 \quad (|\downarrow_{x,L}\downarrow_{x,R}\rangle) \quad \text{for} \quad \alpha_x = 1, \alpha_{x+1} = 2. \end{aligned} \tag{3.33}$$

To obtain matrices $M^{\sigma_x}_{\alpha,\alpha'}$ at each bond, we multiply the factor $\pm\frac{1}{\sqrt{2}}$ from the valence bond definition (Eq.3.27) by the factor from symmetrization rules

($\sigma^x = \pm 1 \Rightarrow 1$ and $\sigma^x = 0 \Rightarrow \frac{1}{\sqrt{2}}$) for each pair σ^x, α_x:

$$\begin{aligned} M_{2,1}^{\sigma^x=+1} &= -\frac{1}{\sqrt{2}} \cdot 1 = -\frac{1}{\sqrt{2}} \\ M_{1,1}^{\sigma^x=0} &= \frac{1}{\sqrt{2}} \cdot \frac{1}{\sqrt{2}} = \frac{1}{2} \\ M_{2,2}^{\sigma^x=0} &= -\frac{1}{\sqrt{2}} \cdot \frac{1}{\sqrt{2}} = -\frac{1}{2} \\ M_{1,2}^{\sigma^x=-1} &= \frac{1}{\sqrt{2}} \cdot 1 = \frac{1}{\sqrt{2}} \end{aligned} \tag{3.34}$$

This gives us three 2×2 matrices corresponding to the physical states $i = -1, 0, +1$, namely:

$$M^{+1} = \begin{pmatrix} 0 & 0 \\ -\sqrt{\frac{1}{2}} & 0 \end{pmatrix}, \quad M^{0} = \begin{pmatrix} \frac{1}{2} & 0 \\ 0 & -\frac{1}{2} \end{pmatrix}, \quad M^{-1} = \begin{pmatrix} 0 & \sqrt{\frac{1}{2}} \\ 0 & 0 \end{pmatrix}. \tag{3.35}$$

We can check the correctness of our new representation by constructing the VBS state for two spin-1 sites and periodic boundary conditions. In such a case, we have two valence bonds, which, after symmetrization, give:

$$\begin{aligned} |\Phi_{VBS}\rangle = \mathbb{S}\,|S_0, S_0\rangle &= \frac{1}{2}\mathbb{S}\left((|\uparrow_{1R}\downarrow_{2L}\rangle - |\downarrow_{1R}\uparrow_{2L}\rangle)(|\uparrow_{2R}\downarrow_{1L}\rangle - |\downarrow_{2R}\uparrow_{1L}\rangle)\right) \\ &= \frac{1}{2}(|\downarrow_{1L}\uparrow_{1R}\downarrow_{2L}\uparrow_{2R}\rangle - |\uparrow_{1L}\uparrow_{1R}\downarrow_{2L}\downarrow_{2R}\rangle \\ &- |\downarrow_{1L}\downarrow_{1R}\uparrow_{2L}\uparrow_{2R}\rangle + |\uparrow_{1L}\downarrow_{1R}\uparrow_{2L}\downarrow_{2R}\rangle) \\ &= \frac{1}{2}\,|T_0 T_0\rangle - \frac{1}{2}\,|T_+ T_-\rangle - \frac{1}{2}\,|T_- T_+\rangle + \frac{1}{2}\,|T_0 T_0\rangle\,. \end{aligned} \tag{3.36}$$

Now, we calculate the AKLT MPS:

$$|\Psi\rangle = \mathrm{Tr}(M^0 M^0)\,|T_0 T_0\rangle + \mathrm{Tr}(M^+ M^-)\,|T_+ T_-\rangle + \mathrm{Tr}(M^+ M^+)\,|T_- T_+\rangle\,. \tag{3.37}$$

From simple matrix multiplication and trace operation, we obtain:

$$|\Psi\rangle = \frac{1}{2}\,|T_0 T_0\rangle - \frac{1}{2}\,|T_+ T_-\rangle - \frac{1}{2}\,|T_- T_+\rangle + \frac{1}{2}\,|T_0 T_0\rangle\,. \tag{3.38}$$

Thus, constructing the VBS state using the singlet product and symmetrization gives the same result as our MPS state.

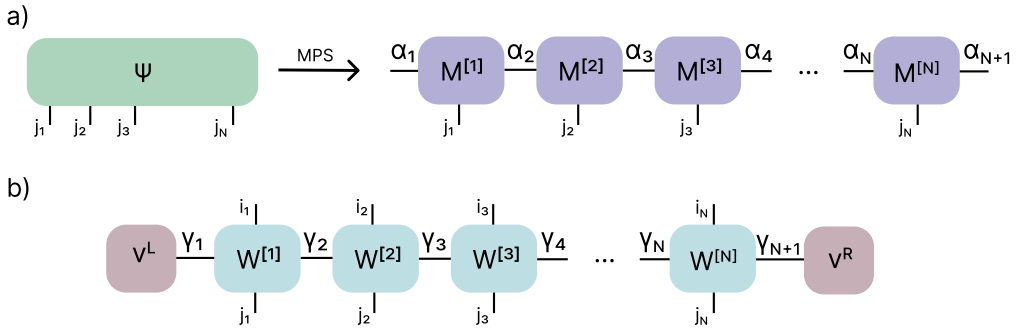

Figure 3.2: Schematic representation of tensor networks used in DMRG algorithm: matrix product state (a) and matrix product operator (b).

3.2.3 Canonical form of the MPS

The form of the MPS obtained from SVD procedure is called left-cannonical [145], because matrices M^{j_n} are left-normalized, obeying condition:

$$\sum_{j_n} (M^{j_n})^\dagger M^{j_n} = \mathbb{I}. \tag{3.39}$$

In general $\sum_{j_n} M^{j_n}(M^{j_n})^\dagger \neq \mathbb{I}$, which has crucial consequences, when we try to divide our MPS into two parts, left A and right B. Such procedure is demanded during DMRG procedure. Let's assume, we cut our system on the bond between n and $n+1$ site. This way we can write our MPS in the form:

$$|\Psi\rangle = \sum_{\alpha_n} |\alpha_n\rangle_A \otimes |\alpha_n\rangle_B \,, \tag{3.40}$$

where we introduce states:

$$|\alpha_n\rangle_A = \sum_{j_1,\dots j_n} M^{j_1} M^{j_2} \dots M^{j_n} \, |j_1, \dots, j_n\rangle \,, \tag{3.41}$$

$$|\alpha_n\rangle_B = \sum_{j_{n+1},\dots j_N} M^{j_{n+1}} M^{j_{n+2}} \dots M^{j_N} \, |j_{n+1}, \dots, j_N\rangle \,. \tag{3.42}$$

This form of the MPS (Eq. 3.40) resembles the Schmidt decomposition of state $|\Psi\rangle$. However, due to the left-normalization of matrices M^{j_n}, states

$|\alpha_n\rangle_A$ are orthogonal $\langle\alpha'_n|\alpha_n\rangle_A = \delta_{\alpha'_n\alpha_n}$, but states from B side are not:

$$\begin{aligned}\langle\alpha'_n|\alpha_n\rangle_B &= \sum_{j_{n+1},\dots,j_N} (M^{j_{n+1}}\dots M^{j_N})^*(M^{j_{n+1}}\dots M^{j_N}) \\ &= \left((M^{j_N})^\dagger\dots(M^{j_{n+1}})^\dagger\right)(M^{j_{n+1}}\dots M^{j_N}) \\ &= \sum_{j_{n+1},\dots,j_N} M^{j_{n+1}}\dots M^{j_N}(M^{j_N})^\dagger\dots(M^{j_{n+1}})^\dagger \neq \delta_{\alpha'_n\alpha_n}.\end{aligned} \tag{3.43}$$

Set of $|\alpha_n\rangle_B$ states are orthogonal, when in SVD procedure we start our decomposition from the left side, instead of the right side. This way we obtain right-cannonical MPS:

$$|\Psi\rangle = \sum_{j_n\dots j_N} N^{j_1}N^{j_2}\dots N^{j_N}\,|j_1\dots j_N\rangle\,, \tag{3.44}$$

where matrices N are right-normalized $\sum_{j_n} N^{j_n}(N^{j_n})^\dagger = \mathbb{I}$.

In order to obtain a true Schmidt decomposition, in which both sets of states $|\alpha_n\rangle_A$ and $|\alpha_n\rangle_B$ form orthonormal bases, we bring the MPS into its canonical form. The key idea is to exploit the gauge freedom of the MPS [247]. We start by inserting an invertible matrix X on the virtual bond between sites n and $n+1$:

$$M^{j_n} \;\to\; \tilde{M}^{j_n} = M^{j_n}X^{-1}, \qquad M^{j_{n+1}} \;\to\; \tilde{M}^{j_{n+1}} = XM^{j_{n+1}}. \tag{3.45}$$

This gauge transformation leaves the physical state $|\Psi\rangle$ invariant but changes its local representation. So the MPS state is now:

$$\begin{aligned}|\Psi\rangle &= \sum_{j_n\dots j_N} M^{j_1}\dots M^{j_n}X^{-1}XM^{j_{n+1}}\dots M^{j_N}\,|j_1\dots j_N\rangle \\ &= \sum_{j_n\dots j_N} M^{j_1}\dots \tilde{M}^{j_n}\tilde{M}^{j_{n+1}}\dots M^{j_N}\,|j_1\dots j_N\rangle\end{aligned} \tag{3.46}$$

From the SVD decomposition we have factorization:

$$\tilde{M}^{i_n} = \Gamma^{i_n}\Lambda^{[n+1]}, \tag{3.47}$$

where $\Lambda^{[n+1]}$ is a diagonal matrix with non-negative entries and Γ^{i_n} is an isometric tensor. After inserting new matrices into equation (3.25) we get:

$$|\Psi\rangle = \sum_{i_1,\dots,i_N} M^{i_1}\cdots\Gamma^{i_n}\Lambda^{[n+1]}\tilde{M}^{i_{n+1}}\cdots M^{i_N}\,|i_1,\dots,i_N\rangle \tag{3.48}$$

By contracting all tensors on the left and right of the diagonal matrix $\Lambda^{[n+1]}$:

$$|\tilde{\alpha}_{n+1}\rangle_L = \sum_{j_1,\ldots,j_n} M^{j_1} \ldots \Gamma^{j_n} |j_1, \ldots, j_n\rangle \tag{3.49}$$
$$|\tilde{\alpha}_{n+1}\rangle_R = \sum_{j_{n+1},\ldots,j_N} \tilde{M}^{j_{n+1}} \ldots M^{j_N} |j_{n+1}, \ldots, j_N\rangle .$$

Using these definitions we can rearrange the full sum: every term in the original expansion contracts into a product of a left-block and right-block:

$$|\Psi\rangle = \sum_{\tilde{\alpha}_{n+1},\tilde{\beta}_{n+1}} \Lambda^{[n+1]}_{\tilde{\alpha}_{n+1},\tilde{\beta}_{n+1}} |\tilde{\alpha}_{n+1}\rangle_L \otimes |\tilde{\alpha}_{n+1}\rangle_R . \tag{3.50}$$

Finally, because Λ^{n+1} is diagonal, $\Lambda^{[n+1]}_{\tilde{\alpha}_{n+1},\tilde{\beta}_{n+1}} = 0$ for $\tilde{\alpha} \neq \tilde{\beta}$, so we can neglect one sum:

$$|\Psi\rangle = \sum_{\tilde{\alpha}_{n+1}} \Lambda^{[n+1]}_{\tilde{\alpha}_{n+1}} |\tilde{\alpha}_{n+1}\rangle_L \otimes |\tilde{\alpha}_{n+1}\rangle_R . \tag{3.51}$$

This expression already resembles the Schmidt decomposition, with the diagonal entries of $\Lambda^{[n+1]}$ playing the role of Schmidt coefficients. By choosing the matrix X appropriately, one can ensure that $|\alpha_{n+1}\rangle_L$ and $|\alpha_{n+1}\rangle_R$ are orthonormal. Thus the spectrum of $\Lambda^{[n+1]}$ corresponds exactly to the entanglement spectrum across the bond n. The complete canonical form of the MPS is obtained by iterating this procedure at each bond of the system:

$$|\psi\rangle = \sum_{i_1,\ldots,i_N} \Lambda^{[1]}\Gamma^{[1]i_1}\Lambda^{[2]}\Gamma^{[2]i_2}\Lambda^{[3]} \ldots \Lambda^{[N]}\Gamma^{[N]i_N} |i_1, \ldots i_N\rangle \tag{3.52}$$

In numerical implementations, it is convenient to group each Γ matrix with one of Λ, obtaining two new sets of tensors:

$$A^{i_n} = \Lambda^{[n]}\Gamma^{i_n}, \quad B^{i_n} = \Gamma^{i_n}\Lambda^{[n+1]}, \tag{3.53}$$

corresponding to left- and right-normalized MPS forms, respectively.

3.2.4 Matrix Product Operators

In modern implementations of the MPS-based DMRG algorithm, not only quantum states but also operators, such as Hamiltonians, observables, or

time-evolution generators, are efficiently represented using Matrix Product Operators (MPO). The MPO formalism generalizes the concept of MPS to linear operators acting on many-body Hilbert spaces and enables efficient contractions and updates during simulations.

An MPO for an operator $\hat{O}$ acting on a 1D lattice with N sites is defined as:

$$O = \sum_{\substack{i_1,\ldots,i_N \\ j_1,\ldots j_N}} v^L W^{[1]i_1 j_1} W^{[2]i_2 j_2} \ldots W^{[N]i_N j_N} v^R \left|i_1, \ldots i_N\right\rangle \left\langle j_1, \ldots j_N\right| \tag{3.54}$$

where $W^{[n]i_n j_n}$ are $D \times D$ matrices associated with site n, indexed by the local input and output basis states $|j_n\rangle$ and $|i_n\rangle$, respectively. The boundary vectors v^L and v^R (dimension D) ensure that the operator is properly terminated at the ends of the chain. The dimension D is called the bond dimension of the MPO.

This form of operator allows the update of the MPS ansatz site after site by contracting the local matrix $M^{[n]i_n}$ of the MPS with the corresponding tensor W^n of the MPO. This operation results in a new MPS, typically with an increased bond dimension. If the MPS has bond dimension χ and the MPO has bond dimension D, then the resulting MPS after application of the operator has bond dimension at most $\chi \cdot D$.

One of the key advantages of the MPO formalism is that all local Hamiltonians with short-range interactions can be encoded as MPOs with small, fixed bond dimensions. For example, a nearest-neighbor spin-1/2 Heisenberg Hamiltonian,

$$H = \sum_i J_x S_i^x S_{i+1}^x + J_y S_i^y S_{i+1}^y + J_z S_i^z S_{i+1}^z, \tag{3.55}$$

can be written as an MPO with $D = 5$, independent of the system size. In order to obtain the MPO form of the Heisenberg Hamiltonian, we aim to represent it as:

$$H = \sum_{\{i_n, j_n\}} \left\langle i_n, \ldots, i_N\right| W^{[1]i_1 j_1} \ldots W^{[N]i_N j_N} \left|j_1, \ldots j_N\right\rangle \tag{3.56}$$

The local operator basis is defined as: $\{\mathbb{I}, S^x, S^y, S^z\}$. Each site has an MPO

tensor $W^{[n]}$ given by:

$$W^{[n]} = \begin{pmatrix} \mathbb{I} & 0 & 0 & 0 & 0 \\ S^x & 0 & 0 & 0 & 0 \\ S^y & 0 & 0 & 0 & 0 \\ S^z & 0 & 0 & 0 & 0 \\ h\mathbb{I} & J_x S^x & J_y S^y & J_z S^z & \mathbb{I} \end{pmatrix} \tag{3.57}$$

For open chain with $L = 2$ spin-$\frac{1}{2}$ sites one can obtain the Hamiltonian by contracting the MPO with left boundary vector $v_L^T = (1, 0, 0, 0, 0)$ and right boundary vector $v_R = (0, 0, 0, 0, 1)^T$:

$$H = v_L^T W^{[1]} W^{[2]} v_R. \tag{3.58}$$

The only nonzero element of the left vector is $v_L^1 = 1$ and the right vector $v_R^5 = 1$, thus:

$$H = \left(W^{[1]} W^{[2]}\right)_{1,5} = \sum_{k=1}^{5} W_{1,k}^{[1]} W_{k,5}^{[2]}. \tag{3.59}$$

Using the nonzero entries of matrices W we get:

$$\begin{aligned} H &= W_{1,1}^{[1]} W_{1,5}^{[2]} + W_{1,2}^{[1]} W_{2,5}^{[2]} + W_{1,3}^{[1]} W_{3,5}^{[2]} + W_{1,4}^{[1]} W_{4,5}^{[2]} W_{1,5}^{[1]} W_{5,5}^{[2]} \\ &= h(\mathbb{I}_1 + \mathbb{I}_2) + J_x S_1^x S_2^x + J_y S_1^y S_2^y + J_z S_1^z S_2^z. \end{aligned} \tag{3.60}$$

From this, we obtain the two-site Hamiltonian produced by the MPO:

$$H_{1,2} = h(\mathbb{I}_1 + \mathbb{I}_2) + \sum_{\alpha=x,y,z} J_\alpha S_1^\alpha S_2^\alpha. \tag{3.61}$$

For longer-range interactions, such as power-law decaying terms or exponentially decaying couplings, MPO representations are still possible, though with moderately increased bond dimensions.

3.2.5 Finite-system DMRG procedure in terms of the MPS

The DMRG procedure, in its modern form, is a variational approach used to optimize the Matrix Product State (MPS). The only required assumption is that the Hamiltonian can be written in the Matrix Product Operator (MPO)

form. The variational space consists of all possible MPS representations with a maximum bond dimension $\chi_{\mathrm{BD}}^{\max}$ for the state $|\psi\rangle$ of the N-site system.

The initial MPS is updated locally at two neighboring sites, n and $n+1$. The goal is to find new matrices $A^{[n]}, \Lambda^{[n]}, B^{[n+1]} \rightarrow A'^{[n]}, \Lambda'^{[n]}, B'^{[n+1]}$ as defined in equation (3.53), while all other tensors in the MPS remain fixed.

The first step involves contracting the tensors for sites n and $n+1$ to obtain the initial wavefunction for these two sites:

$$\Theta^{i_n,i_{n+1}}_{\alpha_n,\alpha_{n+2}} = \sum_{\alpha_{n+1}} \Lambda^{[n]}_{\alpha_n\alpha_n} B^{i_n}_{\alpha_n\alpha_{n+1}} B^{i_{n+1}}_{\alpha_{n+1}\alpha_{n+2}}. \tag{3.62}$$

The variational space for the two-site update is spanned by the orthonormal basis $\{|\alpha_n\rangle_L \otimes |i_n\rangle \otimes |i_{n+1}\rangle \otimes |\alpha_{n+2}\rangle_R\}$. The wavefunction can then be written as:

$$|\tilde{\psi}\rangle = \sum_{\alpha_n,i_n,i_{n+1},\alpha_{n+2}} \tilde{\Theta}^{i_n,i_{n+1}}_{\alpha_n,\alpha_{n+2}} |\alpha_n, i_n, i_{n+1}, \alpha_{n+2}\rangle . \tag{3.63}$$

This wavefunction must minimize the energy $E = \langle\tilde{\psi}| H^{\mathrm{eff}} |\tilde{\psi}\rangle$, where H^{eff} represents the Hamiltonian projected onto the variational space.

The sites to the left of site n are contracted to form the environment $L^{[n]}$, while those to the right of site $n+1$ form the environment $R^{[n+1]}$.

The most computationally expensive step in the DMRG procedure is finding the ground-state vector $\tilde{\Theta}$ of the effective Hamiltonian. This can be achieved by methods such as the Lanczos procedure, which does not require full diagonalization of the Hamiltonian.

After optimizing the two-site tensor $\tilde{\Theta}$, it is reshaped into a matrix and subjected to singular value decomposition (SVD):

$$\tilde{\Theta}^{(i_n,\alpha_n),(i_{n+1},\alpha_{n+2})} = \sum_{\alpha_{n+1}} U_{\alpha_n,i_n,\alpha_{n+1}} \Lambda_{\alpha_{n+1}} V^{\dagger}_{\alpha_{n+1},i_{n+1},\alpha_{n+2}}. \tag{3.64}$$

The singular values $\Lambda_{\alpha_{n+1}}$ are truncated to retain only the largest $\chi_{\mathrm{BD}}^{\max}$ values, controlling the bond dimension and truncation error. The matrices U, Λ, and V are then used to update the MPS tensors at sites n and $n+1$, maintaining the canonical form.

After this update, the algorithm moves on to the next pair of sites, selecting new environments. This process resembles the *sweep* described previously. By sweeping back and forth through the system and repeating this optimization, the algorithm converges to an MPS that minimizes the energy within the variational manifold of fixed bond dimension.

While originally designed for ground-state calculations, DMRG can be extended to compute excited states by targeting multiple orthogonal states or using correction vectors. Time-dependent generalizations such as time-evolving block decimation (TEBD) and time-dependent DMRG (tDMRG) allow the simulation of real-time dynamics in 1D systems [251].

Chapter 4

Moiré quantum dot arrays

Twisted TMD heterobilayers form moiré superlattices that can be used as tunable quantum simulators of the Hubbard model on a triangular lattice. The twist angle acts as a continuous tuning knob for the effective moiré lattice spacing and the depth of the moiré potential, enabling access to both weakly and strongly correlated regimes. Unlike the idealized Hubbard model with purely on-site interactions, moiré systems naturally host strong long-range Coulomb interactions. These arise from non-negligible scattering terms whenever the periodic potential has finite amplitude, with their strength determined by the overlap of localized moiré wavefunctions. In the unphysical limit of infinite potential depth, such overlaps vanish, and only on-site terms remain. Consequently, moiré heterobilayers offer a suitable platform for simulating strongly correlated phenomena beyond the standard Hubbard physics.

The shape of the moiré potential closely resembles that of semiconductor quantum dots. State-of-the-art implementations of the Hubbard model in real-space use STM-based lithography to fabricate artificial quantum dot lattices [252–255]. However, in such setups, control of such systems is limited to external fields or applied strain. In contrast, moiré bilayers offer a more flexible alternative, where electronic properties can be modified intrinsically via twist angle or dielectric environment, leading to various correlated states.

Continuum models of interacting moiré TMDs have predicted a variety of correlated phenomena. These include Mott insulating behavior at integer fillings, spin- and charge-density wave formation, topological flat bands, and Wigner crystallization in the dilute limit [256–259]. Moreover, the interaction strength is strongly influenced by dielectric screening, which can be effectively

included via an effective dielectric constant ϵ. At the half-filling, a phase diagram contains a Mott transition between metallic and insulating states and another one between antiferromagnetic and ferromagnetic phases [260]. Notably, these works typically focus exclusively on bulk properties, neglecting edge effects and finite-size corrections that may be crucial for experiments on small flakes or arrays with non-periodic geometries.

In this chapter, we extend these ideas to finite-size moiré systems modeled as flakes of twisted TMD heterobilayers. We treat the moiré potential as a smooth periodic confinement, effectively forming a triangular array of quantum dots. Using numerical diagonalization methods, we investigate how boundary effects influence the electronic and magnetic properties of the system.

4.1 Continuum model for twisted TMD heterostructures

In twisted TMD heterobilayers, the intrinsic layer asymmetry causes charge carriers (electrons or holes) in the valence band to localize only in one layer, while the other layer acts as an effective potential with the periodicity of a moiré superlattice. Due to strong spin–orbit coupling and spin-valley locking, the low-energy physics near a single valley can be accurately described by a spinless continuum model. The results for spin-↑ and spin-↓ states are related by time-reversal symmetry and are thus equivalent up to a reversal of momentum.

The effective single-valley continuum Hamiltonian takes the form [261]:

$$\mathcal{H}^{\mathbf{K}} = -\frac{\hbar^2}{2m^*}\mathbf{k}^2 + \Delta(\mathbf{r}), \tag{4.1}$$

where the first term represents the kinetic energy, and $m^* = 0.35m_0$ is the effective mass of valence band carriers in $WSe_2/MoSe_2$ heterobilayer.

The moiré potential $\Delta(\mathbf{r})$ is a smooth, periodic function. It can be expanded in terms of the moiré reciprocal lattice vectors $\mathbf{b}_i$:

$$\Delta(\mathbf{r}) = \sum_{\mathbf{b}} V(\mathbf{b}) e^{i\mathbf{b}\cdot\mathbf{r}}, \tag{4.2}$$

where $V(\mathbf{b})$ are the complex Fourier amplitudes. In practice, it is common to approximate this sum by retaining only the first harmonic shell, leading

to:

$$\Delta(\mathbf{r}) = 2V_m \sum_{j=1,3,5} \cos\left(\mathbf{b}_j \cdot \mathbf{r} + \psi\right), \tag{4.3}$$

with $\mathbf{b}_j = \frac{4\pi}{\sqrt{3}a_M}\left(\cos\frac{\pi j}{3}, \sin\frac{\pi j}{3}\right)$, where a_M is the moiré lattice constant, which is for small twist angles θ approximated as $a_M \approx a_0/\theta$, and a_0 is the lattice mismatch parameter, taken as $a_M = 19$ nm for a 1° twist in $WSe_2/MoSe_2$. The parameters V_m and ψ determine the amplitude and phase (i.e., position of minima) of the moiré potential and are typically extracted from ab initio calculations. For this work, we adopt values $(V_m, \psi) = (6.6\text{ meV}, -94°)$, as reported in Ref. [259].

Since the potential is periodic with the moiré lattice, we can apply Bloch's theorem, and the single-particle states can be expanded in the plane-wave basis:

$$|\mathbf{k}, n\rangle = \sum_{\mathbf{G}} z^n_{\mathbf{k}+\mathbf{G}} \left|\mathbf{k} + \mathbf{G}\right\rangle. \tag{4.4}$$

Here, $\mathbf{k}$ belongs to the first moiré Brillouin zone, $\mathbf{G}$ are reciprocal lattice vectors of the moiré lattice, and $z^n_{\mathbf{k}+\mathbf{G}}$ are the expansion coefficients for band index n. State $|\mathbf{k}+\mathbf{G}\rangle$ is a plane wave defined as $e^{i(\mathbf{k}+\mathbf{G})r}$. The Hamiltonian in this basis can be written in the matrix form:

$$H_{\mathbf{G},\mathbf{G}'}(\mathbf{k}) = \frac{\hbar^2}{2m^*}|\mathbf{k}+\mathbf{G}|^2\delta_{\mathbf{G},\mathbf{G}'} + \Delta_{\mathbf{G},\mathbf{G}'} \tag{4.5}$$

where the diagonal terms correspond to kinetic energy, and $\Delta_{\mathbf{G}-\mathbf{G}'}$ are the Fourier components of the moiré potential. Under the first-harmonic approximation, only six components are non-zero and due to the threefold-rotational symmetry, we require $\Delta_{\pm\mathbf{b}_1} = \Delta_{\pm\mathbf{b}_3} = \Delta_{\pm\mathbf{b}_5} = V_m e^{\pm i\psi}$, where $b_5 = b_3 - b_1$.

Figure 4.1(a,b) presents the low-energy moiré minibands computed for twist angles $\theta = 2.0°, 3.5°$, showing the six bands closest to the valence band maximum.

4.2 Wannier functions and Coulomb elements in real space

To analyze finite-size systems, we must describe the electronic properties of moiré quantum dots in a real space. This can be accomplished by constructing Wannier functions representing hole states localized at the sites of the moiré superlattice.

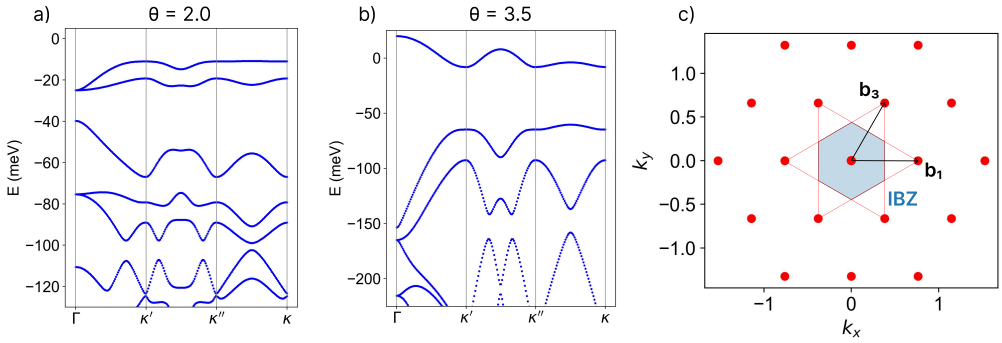

Figure 4.1: Moiré bands calculated from the continuum model for twist angles $\theta = 2.0$ (a) and $\theta = 3.5$ (b). Plane-wave vectors G form a triangular lattice in momentum space (c); the first Brillouin zone is marked in blue.

Starting from the continuum model diagonalized in a plane-wave basis, we obtain the energy spectrum $E_n(\mathbf{k})$ and Bloch eigenstates $|\Psi_n(\mathbf{k})\rangle$. For the topmost valence band, the eigenstate has the form:

$$|\Psi_{tVB}(\mathbf{k})\rangle = \sum_{\mathbf{G}} z^{tVB}_{\mathbf{k}+\mathbf{G}} e^{i(\mathbf{k}+\mathbf{G})\mathbf{r}}. \tag{4.6}$$

To construct real-space Wannier functions from these Bloch states, we employ the projection method [262, 263]. In this approach, we choose a real-space trial wavefunction $|t_i(\mathbf{r})\rangle$ centered at site i. This trial state is projected onto the Bloch state to obtain:

$$|\gamma_i(\mathbf{k})\rangle = P(\mathbf{k})\,|t_i(\mathbf{k})\rangle = |\Psi_{tVB}(\mathbf{k})\rangle\,\langle\Psi_{tVB}(\mathbf{k})|t_i(\mathbf{k})\rangle\,. \tag{4.7}$$

The overlap between a trial wavefunction and a Bloch state is given by:

$$S(\mathbf{k}) = \langle t_i(\mathbf{k})|\gamma_i(\mathbf{k})\rangle = |\langle\Psi_{tVB}(\mathbf{k})|t_i(\mathbf{k})\rangle|^2\,. \tag{4.8}$$

The projected state is then orthonormalized:

$$|\tilde{\Psi}_{tVB}(\mathbf{k})\rangle = \frac{1}{\sqrt{S(\mathbf{k})}}\,|\gamma_i(\mathbf{k})\rangle = |\Psi_{tVB}(\mathbf{k})\rangle\,\frac{\langle\Psi_{tVB}(\mathbf{k})|t_i(\mathbf{k})\rangle}{|\,\langle\Psi_{tVB}(\mathbf{k})|t_i(\mathbf{k})\rangle\,|} = |\Psi_{tVB}(\mathbf{k})\rangle\,e^{-i\theta_t(\mathbf{k})}, \tag{4.9}$$

where $\theta_t(\mathbf{k})$ is the phase of the overlap. This gauge-fixing procedure ensures that the resulting Wannier functions are exponentially localized.

To obtain maximally localized Wannier functions centered at the moiré cell centers, it is sufficient to use delta-like or Gaussian trial functions centered at $\boldsymbol{\tau}_i$. In this work, we use the delta function: $|t_i(\mathbf{r})\rangle = \delta(\mathbf{r} - \tau_i)$ and its Fourier transformation:

$$|t_i(\mathbf{k})\rangle = \frac{1}{\sqrt{N_G}} \sum_{\mathbf{G}} e^{i(\mathbf{k}+\mathbf{G})(\mathbf{r}-\tau_i)}, \tag{4.10}$$

where N_G is a number of plane-wave basis vectors $\mathbf{G}$. The overlap of the trial wavefunction with the Bloch state is:

$$\begin{aligned}\langle \Psi_{tVB}(\mathbf{k})|t(\mathbf{k})\rangle &= \frac{1}{\sqrt{N_G}} \sum_{\mathbf{G},\mathbf{G}'} z^*_{\mathbf{k}+\mathbf{G}} \int d\mathbf{r} e^{-i(\mathbf{k}+\mathbf{G}')\mathbf{r}} e^{i(\mathbf{k}+\mathbf{G})(\mathbf{r}-\tau_i)} \\ &= \frac{V_{cell}}{\sqrt{N_G}} \sum_{\mathbf{G}} z^*_{\mathbf{k}+\mathbf{G}} e^{-i(\mathbf{k}+\mathbf{G})\tau_i}\end{aligned} \tag{4.11}$$

where V_{cell} is the moiré unit cell area. After fixing the phase, the Wannier functions are exponentially localized in positions $\mathbf{R}$ of moiré superlattice cell centered:

$$|\mathbf{R}\rangle = \frac{1}{\sqrt{N}} \sum_{\mathbf{k}} e^{-i\mathbf{k}\cdot\mathbf{R}} \left|\tilde{\Psi_{tVB}}(\mathbf{k})\right\rangle, \tag{4.12}$$

where N is the number of unit cells.

The continuum model describes the single-particle electronic structure. To introduce electron-electron interactions in the many-body Hamiltonian, we evaluate Coulomb matrix elements in the Wannier basis. The general form of the four-center Coulomb integral is:

$$\begin{aligned}&\langle \mathbf{R}_i, \mathbf{R}_j | \, V \, | \mathbf{R}_k, \mathbf{R}_l \rangle = \\ &\frac{1}{N^2} \sum_{\substack{\mathbf{k}_i,\mathbf{k}_j \\ \mathbf{k}_k,\mathbf{k}_l}} e^{i(\mathbf{k}_i\cdot\mathbf{R}_i + \mathbf{k}_j\cdot\mathbf{R}_j - \mathbf{k}_k\cdot\mathbf{R}_k - \mathbf{k}_l\cdot\mathbf{R}_l)} \langle \tilde{\boldsymbol{\Psi}}^{\mathbf{k}_i}_{tVB}, \tilde{\boldsymbol{\Psi}}^{\mathbf{k}_j}_{tVB} | \, V \, | \tilde{\boldsymbol{\Psi}}^{\mathbf{k}_k}_{tVB}, \tilde{\boldsymbol{\Psi}}^{\mathbf{k}_l}_{tVB} \rangle\end{aligned} \tag{4.13}$$

Here, the Coulomb operator is:

$$V(\mathbf{r}_1 - \mathbf{r}_2) = \frac{e^2}{4\pi\varepsilon_0\varepsilon|\mathbf{r}_1 - \mathbf{r}_2|}, \tag{4.14}$$

where vectors $\mathbf{r}_1$, $\mathbf{r}_2$ are positions of electrons, e denotes electric charge, ε is the effective dielectric constant of the environment, and ε_0 is the vacuum permittivity. From general four-center integrals, we can define:

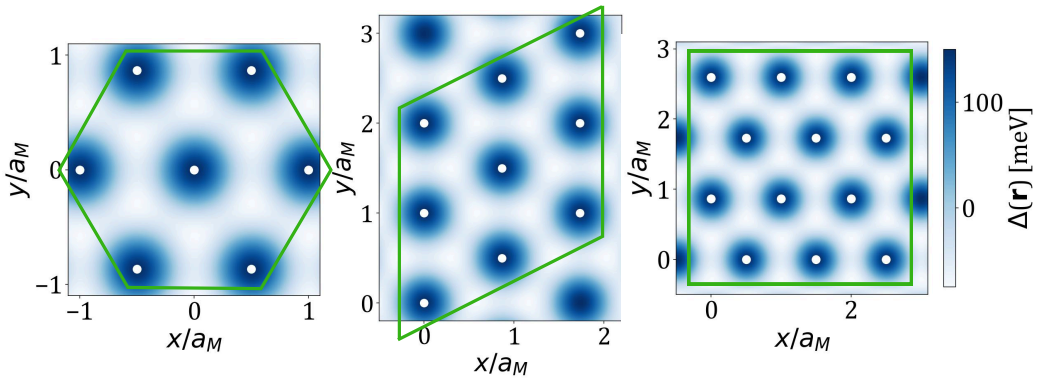

Figure 4.2: The effective moiré potential defines triangular lattice of moiré quantum dots. Exemplary structures analyzed in this work consist of N = 7,9,12 sites.

- U_0: on-site interaction ($i = j = k = l$),
- $U_n = U_1/r_n$: direct intersite interaction for $i = l$ and $j = k$, where i, j are n-th nearest neighbors,
- $X_n = X_1/r_n$: exchange interaction for $i = k$, $j = l$,
- $A_n = A_1/r_n$: assisted hopping interaction for $i = j = k$.

The kinetic part of the effective Hubbard Hamiltonian is derived from the Bloch band structure. Hopping amplitudes between n-th neighbors are given by:

$$t_n = \frac{1}{N} \sum_{\mathbf{k}} e^{-i\mathbf{k}(\mathbf{R}_i - \mathbf{R}_j)} E_{\mathbf{k}}. \tag{4.15}$$

The Coulomb interaction strength depends on the choice of dielectric constant ε, which contains screening from the surrounding material and internal polarization. Values of t_n, U_0, U_1, X_1, and A_1 computed for twist angles $2° \leq \theta \leq 5°$ are presented in Figure 4.3.

4.3 Generalized Hubbard Hamiltonian

Finite-size flakes of moiré TMD heterobilayers can be described within the generalized Hubbard Hamiltonian, including on-site and direct Coulomb, as

well as exchange and assisted hopping terms:

$$H = -\sum_{n=1}^{3} t_n \sum_{<i,j>_n,\sigma} a^{\dagger}_{i,\sigma} a_{j,\sigma} + U_0 \sum_i n_{i,\downarrow} n_{i,\uparrow} + \sum_{n=1}^{3} U_n \sum_{<i,j>_n,\sigma,\sigma'} n_{i,\sigma} n_{j,\sigma'} - X_1 \sum_{<i,j>,\sigma} n_{i,\sigma} n_{j,\sigma} + A_1 \sum_{<i,j>,\sigma} (n_{i,-\sigma} + n_{j,-\sigma}) a^{\dagger}_{i,\sigma} a_{j,\sigma}, \tag{4.16}$$

where $a^{\dagger}_{i,\sigma}$ ($a_{i,\sigma}$) denote the fermionic creation (annihilation) operator for an electron with spin σ at lattice site i. The notation $\langle i,j\rangle_n$ refers to a pair of n-th nearest-neighbor sites, with the condition $i > j$ imposed to avoid double counting in the summations. The interaction strength is controlled by the effective dielectric constant ϵ, which is estimated to lie in the range $10 < \epsilon < 20$. This estimate corresponds to a structure with hexagonal boron nitride (hBN) used as a substrate, leading to $\epsilon \approx 6$ [264], along with additional screening effects due to conducting gates and virtual transitions between the relevant and higher moiré bands. We focus our analysis on finite-size flakes consisting of $N = 7, 9, 12$ quantum dots, which are shown in Figure 4.2. Despite their small size, these clusters capture key features of the underlying many-body physics and allow for numerically exact treatment.

4.3.1 Magnetic phase diagrams

Firstly, we analyze the magnetic phase diagrams of the representative structure with $N = 9$ quantum dots. Our analysis is based on the computation of the total spin S of the many-body ground state across a broad range of twist angles $2.0^\circ \leq \theta \leq 5.0^\circ$, and electronic filling factors $0 \leq \nu \leq 2$, where the filling is defined as $\nu = N_p/N$, with N_p denoting the number of particles. For twist angles $\theta > 5^\circ$ the one-band approximation might be inaccurate. The resulting phase diagrams are presented in Figure 4.4, where color maps indicate the ground-state total spin for two values of the effective dielectric constant: $\epsilon = 10$ (a) and $\epsilon = 20$ (b). For the stronger interaction regime ($\epsilon = 10$), the system exhibits regions of maximal spin polarization at twist angles below $\theta = 4^\circ$. Notably, the phase diagram is asymmetric with respect to the half-filling, which is particularly evident at lower fillings. The asymmetry is a result of the fact that the triangular lattice is not bipartite.

The main mechanism behind spin polarization of the many-body ground state is the direct exchange interaction due to the overlap of Wannier func-

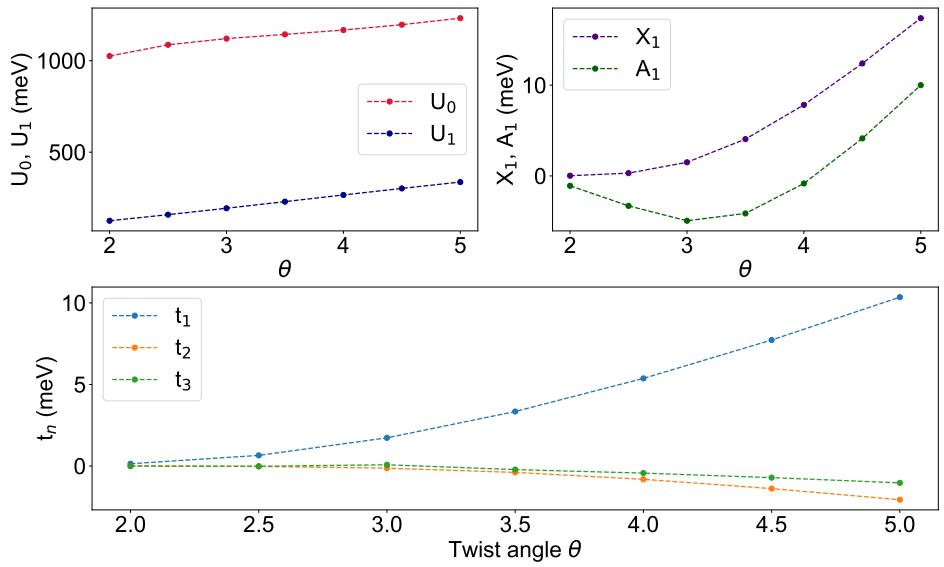

Figure 4.3: Dependence of Hubbard parameters on the twist angle θ.

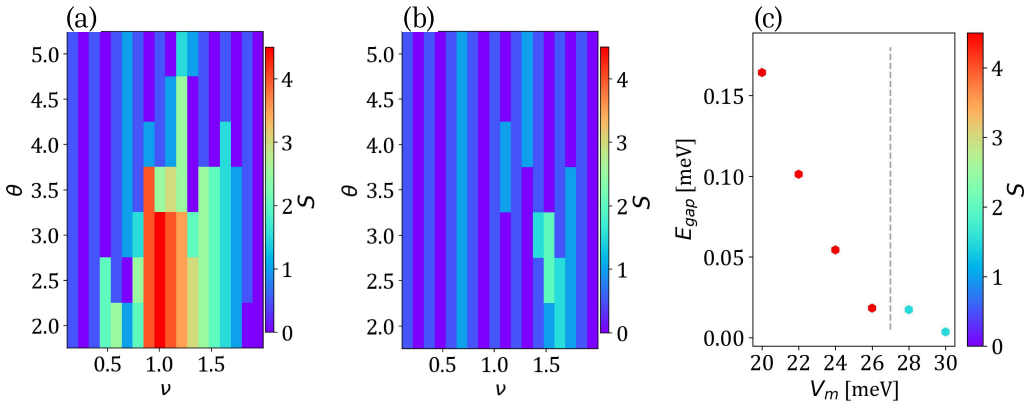

Figure 4.4: Total spin S of moiré TMD heterostructures consisting of $N = 9$ quantum dots as a function the filling factor ν and the twist angle θ for fixed values of the dielectric constant $\epsilon = 10$ (a), $\epsilon = 20$ (b). (c) The energy gap and total spin of the ground state depend on the potential depth. Figures adapted from Ref. [2].

tions. At larger twist angles ($\theta > 4°$), separations between single-particle levels increase and exceed the scale of the exchange interaction, which results in vanishing spin polarization. The magnetization can be suppressed externally by applying the displacement field, which changes the depth of a moiré potential. Without an additional electric field ($V_m = 25$ meV), the ground state at the half-filling $\nu = 1$, and $\theta = 3.0$ is fully polarized. Figure 4.4 (c) shows how the energy gap between the ground state with maximal total spin and the excited states with lower total spin decreases. At the point between $V_m = 26$ meV and $V_m = 28$ meV transition occurs and the total spin of the ground state is lowered. In the case of a weaker interaction regime for $\epsilon = 20$, the magnetic diagram reveals almost no spin polarization. This is due to the fact that the energy scale of Coulomb terms is too small in comparison to the separations of single-particle energy levels. As a result, particles mostly doubly occupy the lowest energy state without excitation above the Hubbard gap.

Besides the twist angle and external displacement field, in finite-size flakes, an important role is played by the shape of the structure and geometrical effects. To demonstrate it, we compare magnetic diagrams at fixed dielectric constant $\epsilon = 10$ and two twist angles $\theta = 2.5, 3.5$ for five structures consisting of $N = 7, 9, 10, 12$ (two structures) quantum dots. The results are summarized in Figure 4.5, where the total spin is normalized with respect to its maximal value at half-filling, $S_{\max} = N/2$. For $\theta = 2.5$, all investigated structures exhibit a fully polarized ground state at half-filling $\nu = 1$ and immediately above it $\nu = 1^+$, which is analyzed in more detail in the next section. Notably, the occurrence of finite spin polarization at half-filling, under conditions of small twist angle and strong interactions, appears to be largely independent of the array's shape or size. This observation is consistent with the expected behaviour in the thermodynamic limit. Above the half-filling, for $1 < \nu < 1.5$, partial spin polarization seems to be also robust against changes in system size or shape. However, below the half-filling, it becomes more sensitive to the system geometry. For example, in the N=12 triangular array, spin polarization oscillates as a function of filling, alternating between fully polarized and unpolarized states (Fig. 4.5 (e)).

4.3.2 Nagaoka ferromagnetism

One of the theoretical predictions for the Hubbard model on two-dimensional lattices is the occurrence of Nagaoka ferromagnetism, which is a mechanism

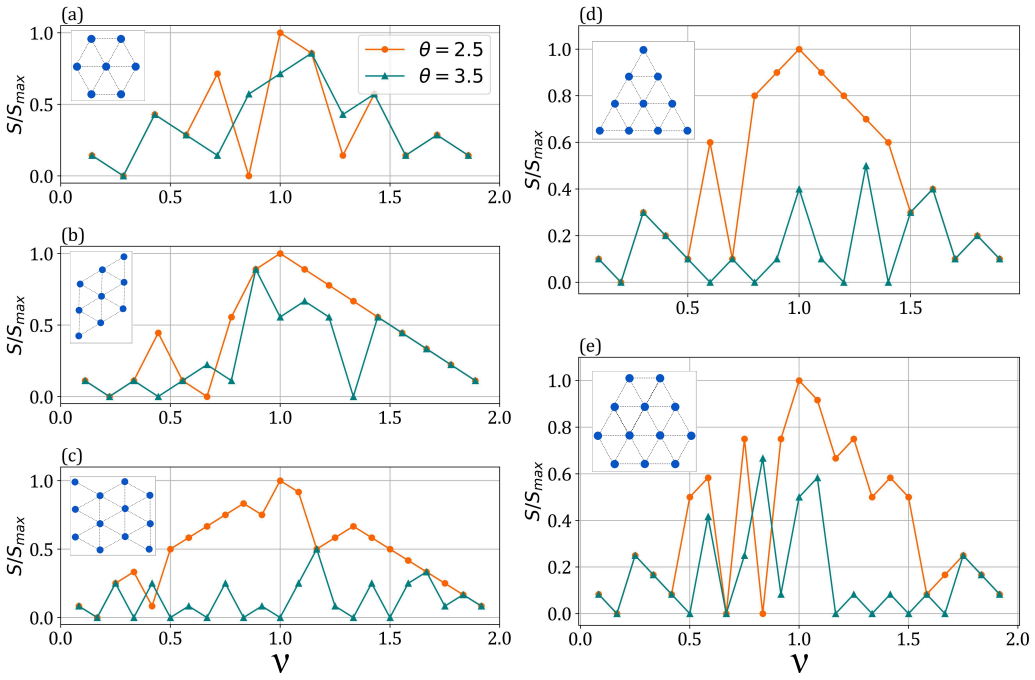

Figure 4.5: The total spin S for structures consisting of $N = 7, 9, 10, 12$ moiré quantum dots as a function of the filling ν for $\theta = 2.5, 3.5$. Geometries of structures are presented as insets. Figures adapted from Ref. [2].

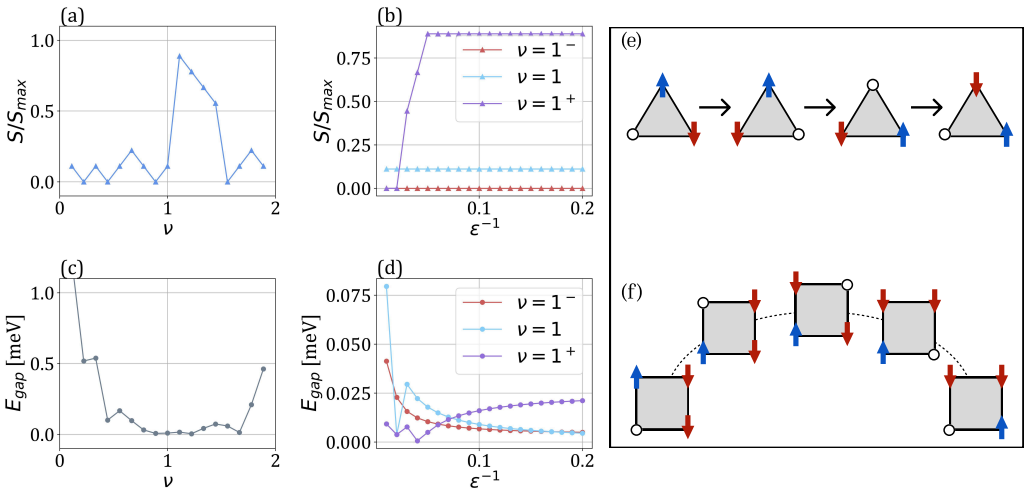

Figure 4.6: Results for the Hubbard model with nonzero amplitudes U_0 and t_1 in the $N = 9$ moiré quantum dot structure. Panel (a) and (c) show, respectively, the ground-state total spin and the corresponding energy gap as functions of the filling factor for $\epsilon = 10$ and $\theta = 2.5$. Panels (b) and (d) present the dependence of the total spin and the energy gap on the interaction strength for selected fillings $\nu = 1^-, 1, 1^+$ at a fixed twist angle $\theta = 2.5$. Panels (e) and (f) show how hopping of the single hole changes the spin configuration on the triangular and square lattices.

leading to a fully spin-polarized ground state in a strongly interacting electron system. In its idealized form, this effect occurs in the limit $U \to \infty$ and for doping by exactly one charge carrier away from half-filling [265]. The underlying mechanism is that the doped carrier moves through the lattice and, by visiting all sites, generates a linear combination of basis states that favors a spin-polarized ground state. Interference between different hopping paths is constructive in the fully polarized state, which effectively lowers the energy and stabilizes ferromagnetism.

A key requirement for the appearance of Nagaoka ferromagnetism is the connectivity condition of the lattice. This condition ensures that, for a given S_z, any spin configuration can be connected with others by nearest-neighbor hoppings. For example, in a triangle (Figure 4.6(e)) two spins are exchanged after one cycle of hole hops, and a second cycle restores the original configuration. In case of the square (Figure 4.6(f)), one cycle of hops exchanges spins on the diagonal, and three cycles are needed to return to the initial state. More formally, the connectivity condition is satisfied if the lattice remains connected (there is a path connecting any site to any other) if any single site is removed. Equivalently, for any two sites i and j, there must exist a loop of odd length containing both i and j. This requirement guarantees that the doped carrier can propagate across the lattice without restrictions.

The weak version of Nagaoka's theorem considers the Hubbard model in the limit $U \to \infty$ and assumes that the hopping amplitude satisfies $t_{i,j} \geq 0$ for any pair i, j. Under those conditions, for $N_e = N_s - 1$ (N_s denotes number of sites), there exist at least $(2S_{tot} + 1)$ degenerate ground states with total spin $S_{tot} = S_{max} = N/2$ [250]. This result alone is not sufficient for ferromagnetism, since the theorem does not exclude other competing ground states. To sketch the proof of this theorem [266,267], we project the Hubbard Hamiltonian Eq. 3.1 onto the subspace $\mathcal{H}^{\mathrm{s}}$ without double occupancy using the projector $\hat{P}_s$. The effective Hamiltonian acting on such a subspace is:

$$\hat{H}_{\mathrm{eff}} = \hat{P}_s \hat{H} \hat{P}_s. \tag{4.17}$$

In the $U \to \infty$ limit, the ferromagnetic ground states of $\hat{H}$ are also ground states of $\hat{H}_{\mathrm{eff}}$. The projection $\hat{P}_s$ guarantees that hoppings that would create double occupancy are forbidden, and in the one-hole sector every allowed nearest-neighbor hop corresponds to moving the hole by one site. Choosing a suitable local gauge for single-site orbitals ensures that every nonzero off-diagonal matrix element of $\hat{H}$eff is nonnegative $tij \geq 0$.

It is convenient to express $\hat{H}_{\text{eff}}$ in the basis states specified by the position i of the hole on the lattice and the spin configuration $\sigma = (\sigma_j)$, where j is the set of all lattice sites. Any state of the single hole in this basis can be written as:

$$|\psi^h_{i,\sigma_i}\rangle = c_{i,\sigma_i}\left(\prod_j c^\dagger_{j,\sigma_j}\right)|0\rangle \tag{4.18}$$

Acting on such a state with the $\hat{H}_{\text{eff}}$ operator, we can conclude that the nonvanishing contribution gives only hopping of an electron into the hole site x from the other site z connected by $t_{x,z} \neq 0$:

$$\begin{aligned}\hat{H}_{\text{eff}}\,|\psi^h_{i,\sigma}\rangle &= \sum_{k,l,\sigma} t_{k,l} c^\dagger_{k,\sigma} c_{l,\sigma} c_{i,\sigma_i}\left(\prod_j c^\dagger_{j,\sigma_j}\right)|0\rangle \\ &= -\sum_l t_{k,l} c_{l,\sigma_i} c^\dagger_{i,\sigma_i} c_{i,\sigma_i}\left(\prod_j c^\dagger_{j,\sigma_j}\right)|0\rangle \\ &= \sum_l (-t_{il})\,|\psi^h_{l,\sigma'}\rangle\,,\end{aligned} \tag{4.19}$$

where $n_i = c^\dagger_i c_i$ is the particle number operator, which gives 1 for site i. In this representation, the hopping term in the Hamiltonian connects a configuration where the hole resides on site i to a configuration in which the hole has moved to a site l. Now, we write the arbitrary normalized ground state of $\hat{H}_{\text{eff}}$ as:

$$|\Psi_{GS}\rangle = \sum_i \sum_\sigma \phi(i,\sigma)\,|\psi^h_{i,\sigma}\rangle\,, \tag{4.20}$$

where coefficients $\phi(i,\sigma)$ are real. Then, for each i we define:

$$C_i = \sqrt{\sum_\sigma \phi^2(i,\sigma)}, \tag{4.21}$$

and corresponding ferromagnetic state:

$$|\Psi_\uparrow\rangle = \sum_i C_i\,|\psi^h_{i,(\uparrow)}\rangle\,, \tag{4.22}$$

where $(\uparrow)$ denotes the fully spin-polarized configuration with $\uparrow$-spin at each

j site. The ground state energy is:

$$\langle\Psi_{GS}|\,\hat{H}_{\text{eff}}\,|\Psi_{GS}\rangle = \sum_{i,i'}\sum_{\sigma,\sigma'}\langle\Psi_{i',\sigma'}|\,\hat{H}_{\text{eff}}\,|\Psi_{i,\sigma}\rangle = -\sum_{i,i'}t_{i,i'}\sum_{\sigma}\phi(i',\sigma')\phi(i,\sigma), \tag{4.23}$$

assuming that σ and σ' are connected by hopping of the hole. A comparison of expectation values with Schwarz's inequality shows that this ferromagnetic state is also a ground state.

$$\begin{aligned}-\sum_{i,i'}t_{i,i'}\sum_{\sigma}\phi(i',\sigma')\phi(i,\sigma) &\geq -\sum_{i,i'}t_{i,i'}\sqrt{\sum_{\sigma'}\phi^2(i',\sigma')}\sqrt{\sum_{\sigma}\phi^2(i,\sigma)}\\ &= -\sum_{i,i'}t_{i,i'}C_iC_{i'} = \langle\Psi_{\uparrow}|\,\hat{H}_{\text{eff}}\,|\Psi_{\uparrow}\rangle\,.\end{aligned} \tag{4.24}$$

To prove that it is the unique ground state, one invokes the Perron–Frobenius theorem [250]. For a real symmetric matrix $\mathrm{M} = (m_{i,j})_{i,j=1,\ldots,N}$ with properties:

- $m_{i,j} \leq 0$ for any $i \neq j$,
- all $i \neq j$ are connected by nonvanishing matrix elements of the matrix,

that theorem ensures that the lowest eigenvalue of M is nondegenerate and the corresponding eigenvector $\mathbf{v} = (v_i)_{i,\ldots,N}$ can be taken to satisfy $v_i > 0$ for all i. Identifying M with the Hamiltonian matrix in the chosen basis shows that $\hat{H}_{\text{eff}}$ has a unique lowest-energy eigenstate in each S_z sector, and that this state is ferromagnetic.

For finite but large U, the theorem is also valid due to the continuity of eigenvalues and the presence of a finite energy gap. However, the U value must be sufficiently large. Figure 4.6 presents numerical results for the moiré TMD Hubbard Hamiltonian Eq. 4.16 ($N = 9$) with only the on-site interaction U_0 and nearest-neighbor hopping t_1 retained, while all scattering terms and longer-range U_n terms are neglected ($U_n = X_n = A_n = 0$, $t_2 = t_3 = 0$). The results are obtained for the twist angle $\theta = 2.5$, for which amplitudes U_0 and t_1 are significantly larger than other terms, so the approximation is justified. Subfigure (a) shows the normalized total spin S/S_{max} as a function of filling ν. For the triangular lattice, spin polarization is expected upon doping with one additional electron, since in our Hamiltonian [Eq. 4.16] the hopping amplitude is negative. While bipartite lattices possess particle-hole

symmetry that supports Nagaoka ferromagnetism for hole and electron doping ($\nu = 1^-$ and $\nu = 1^+$), the triangular lattice does not. Consistent with this, our results reveal a sudden spin polarization for electron doping at $\nu = 1^+$. Subfigure (b) shows that increasing the dielectric constant ϵ drives the transition into the fully polarized state around $\epsilon \approx 20$, accompanied by an increase in the energy gap (d).

In the complete model for moiré TMD flakes, the Nagaoka mechanism still contributes to spin polarization near $\nu = 1^+$ (Figure 4.5) by increasing the energy gap, which makes it more stable in comparison to other fillings.

4.3.3 Generalized Wigner crystal states

In addition to spin-polarized states, strongly interacting electrons in finite moiré TMD flakes can also form spatially ordered charge configurations. The original idea by Wigner predicts the formation of electronic crystals in the low-density limit of the electron gas, where minimizing the Coulomb repulsion leads to a regular lattice arrangement of charges [4]. In our system, the presence of an underlying moiré superlattice and a narrow electronic bandwidth allows similar charge ordering to occur at much higher carrier densities. Such states are referred to as generalized Wigner crystals, since the periodic potential and lattice geometry determine the specific arrangement of charges.

In the presence of the direct Coulomb interaction, it is energetically favorable for electrons to occupy sites that are maximally separated. As a result, in triangular arrays the charge tends to localize at the corners of the structures, forming so-called Wigner molecules. Figure 4.7 presents electronic density ρ_E and spin density ρ_S of the ground state $|\Psi_0\rangle$ defined as:

$$\rho_E = \sum_\sigma \langle\Psi_0| a^\dagger_{i\sigma} a_{i\sigma} |\Psi_0\rangle = \langle n_{i\uparrow}\rangle + \langle n_{i\downarrow}\rangle, \tag{4.25}$$

$$\rho_S = \langle n_{i\uparrow}\rangle - \langle n_{i\downarrow}\rangle, \tag{4.26}$$

for triangular arrays with $N = 10$ and $N = 12$ moiré quantum dots. The particle number operators for spin up and down are defined as $n_{i\uparrow} = c^\dagger_{i\uparrow} c_{i\uparrow}$ and $n_{i\downarrow} = c^\dagger_{i\downarrow} c_{i\downarrow}$. For $N = 10$ flake, charge localization is most pronounced for particle numbers $N_p = 3, 7, 13, 17$. The latter two correspond to fillings $\nu = 0.7$ and $\nu = 1.3$, the removal or addition of three particles relative to the charge-neutral configuration. Figures 4.7 (a,b) illustrate the charge and spin densities for the case $\nu = 1.3$: the three corner sites are doubly occupied,

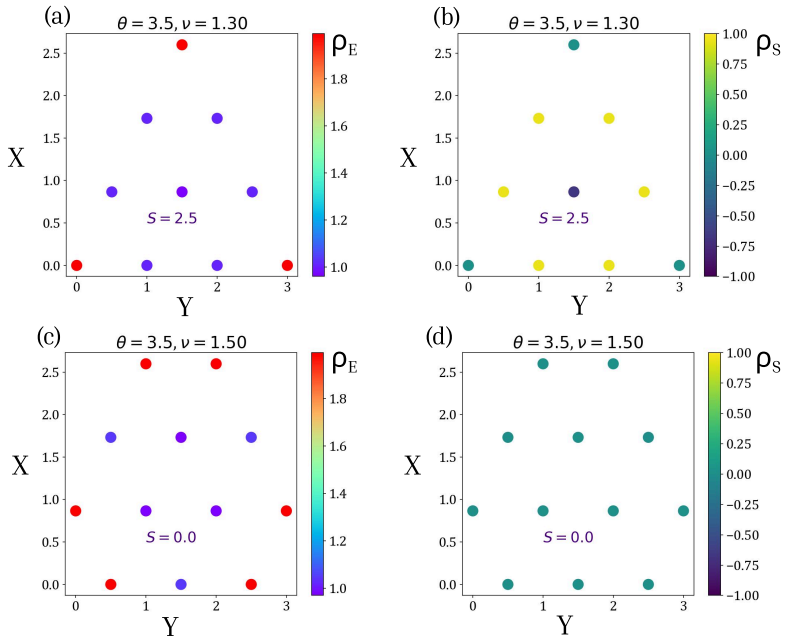

Figure 4.7: Charge (a,c) and spin (b,d) densities showing the formation of Wigner molecules in triangular arrays with $N = 10$ and $N = 12$ moiré quantum dots. Results are obtained for twist angle $\theta = 3.5$ and dielectric constant $\epsilon = 10$. Figures adapted from Ref. [2].

while the remaining quantum dots are singly occupied. The ground state has total spin $S = 2.5$, characterized by a single $\downarrow$-spin electron localized at the central site and surrounded by six $\uparrow$-spin electrons. A similar effect is observed in the $N = 12$ triangular array, where each corner is formed by a pair of quantum dots. In this case, Wigner molecules emerge when six particles are added or removed from half-filling. Figures 4.7 (c,d) show the charge and spin densities for $N_p = 18$. Unlike in the $N = 10$ case, the total spin is minimal, and the spin density is nearly uniform across the array. Worth noting is the fact that the appearance of Wigner molecules in both triangular geometries is robust against small changes of the twist angle, even though the spin configuration is sensitive to it. For example, in the $N = 12$ array at filling $\nu = 1.5$, changing the twist angle from $\theta = 2.5$ to $\theta = 3.5$ reduces the total spin of the ground state from the maximal value $S = 3$ to the minimal $S = 0$, while the Wigner molecules at the structure corners remain intact.

4.4 Flakes vs. continuum model

To conclude this section, we compare the results for finite moiré TMD flakes with those obtained for periodic models. At half-filling, the magnetic properties of the generalized Hubbard model on flakes closely mirror those of continuum models. Strong electron–electron interactions ($\epsilon = 10$) at small twist angles favor finite spin polarization, while weaker interactions or larger twist angles suppress it. In finite flakes, however, the restricted system size prevents the emergence of long-range 120° Néel antiferromagnetism predicted for extended systems. Similarly, the Nagaoka ferromagnetism expected at $\nu = 1^+$ in continuum models is suppressed by boundary effects. Away from half-filling, the two cases diverge more significantly. Periodic lattices can stabilize generalized Wigner crystal phases at fractional fillings, whereas geometric constraints in finite arrays inhibit such extended charge order. Instead, finite flakes develop localized Wigner molecules, typically concentrated at the corners, with spin configurations that are highly sensitive to the twist angle.

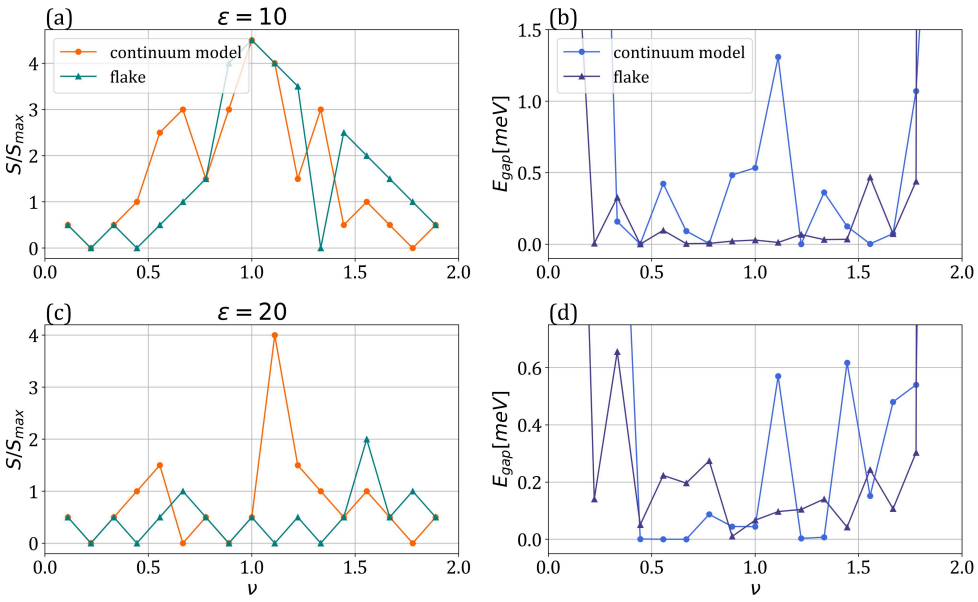

Figure 4.8: Comparison of the normalized total spin of the ground state S/S_{max} (a,c) and the energy gap E_{gap} (b,d) between a finite-size moiré TMD flake and a model with periodic boundary conditions representing bulk properties. Parameters are fixed to the twist angle $\theta = 3.0$ and two values of the dielectric constant $\epsilon = 10, 20$.

Chapter 5

Designing QSL states in moiré TMD heterostructures

As was presented in the previous chapter, moiré TMD flakes manifest different magnetic behaviour at the half-filling depending on the twist angle and influence of the environment or experimental setting, expressed as a change of the dielectric constant. To move beyond finite-size effects, we now extend our analysis toward the thermodynamic limit. This is achieved by studying the effective spin model at half-filling.

5.1 Spin model from the generalized Hubbard Hamiltonian

In order to approximate the low-energy spectrum of the generalized Hubbard Hamiltonian by the spin model, we have to project the fermionic Hamiltonian onto the subspace consisting of only singly occupied states. The energy spectrum of the Hubbard model in the limit of $t \ll U$ consists of two bands, the lower and upper Hubbard bands (Fig. 5.1b). States with singly occupied sites have lower energy, due to the lack of onsite interaction, and the hopping of the electron, which creates double occupancy (dublon), costs energy U. This results in a finite gap between bands with and without dublons. Such a finite gap is the requirement for the applicability of the effective spin Hamiltonian. In moiré TMD flakes, the ratio between onsite interaction strength and hopping amplitudes depends on the twist angle. Thus, to examine in what range of (θ, ϵ) the spin model can be used, we must analyze the energy

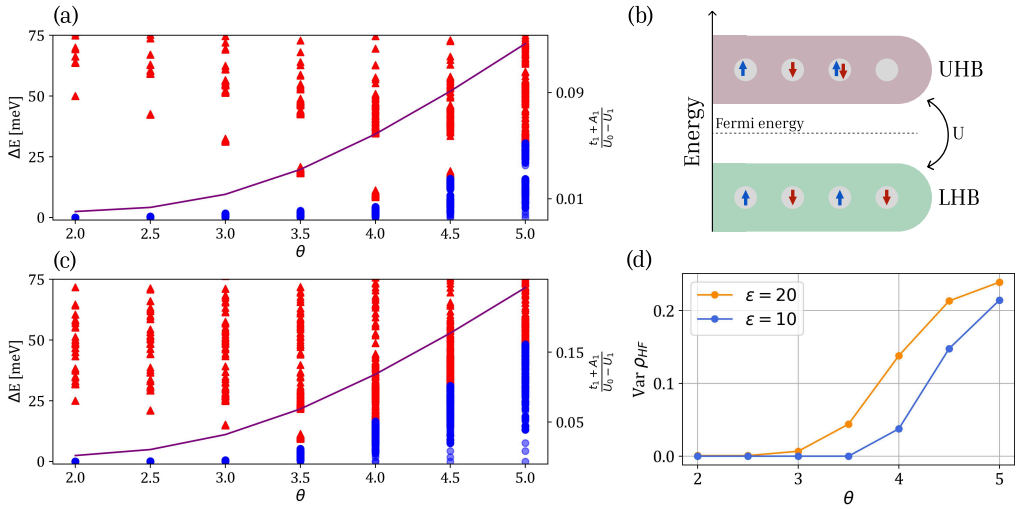

Figure 5.1: Energy spectrum of generalized Hubbard model as a function of the twist angle θ and dielectric constant $\epsilon = 10$ (a), $\epsilon = 20$ (c). First $2^9 = 512$ states of the lower Hubbard band are denoted by blue color. Schematic representation of the lower and upper Hubbard bands is presented in subfigure (b). Function Var $\rho_{HF}(\theta)$ shows how average occupancy at the half-filling vary away from $\rho_{HF} = 1$ (d).

spectrum and average site occupancy of the generalized Hubbard model. Figure 5.1 (a,c) shows the energy spectrum of N=9 moiré quantum dots as a function of the twist angle θ for the dielectric constant $\epsilon = 10, 20$, respectively. The lower Hubbard band consists in this case of $2^9 = 512$ states, which are indicated by the blue color. States from the upper Hubbard band are red. We see that the energy gap between those two bands remains finite up to $\theta = 4.0$ for $\epsilon = 10$ and $\theta = 3.5$ for $\epsilon = 20$. Thus, we can assume that at the range $10 \leq \epsilon \geq 20$ the spin model approximation is adequate for $\theta \leq 3.5$. In Ref. [268], the authors estimated the applicability of the spin model for $t/U < 0.15$. In the case of the generalized Hubbard model, we should examine the value $\frac{t_1+A_1}{U_0-U_1}$, which is presented in Fig. 5.1(a,c) as a purple line. For $\epsilon = 10$ gap closes at the ratio $\frac{t_1+A_1}{U_0-U_1} \simeq 0.09$ and $\frac{t_1+A_1}{U_0-U_1} \simeq 0.11$ for $\epsilon = 20$. This approximation doesn't take into account the exchange interaction, which usually moves Hubbard bands away from each other. Another way to confirm the correctness of the spin model approximation is to look into the average occupancy of moiré quantum dots at the half-filling. The

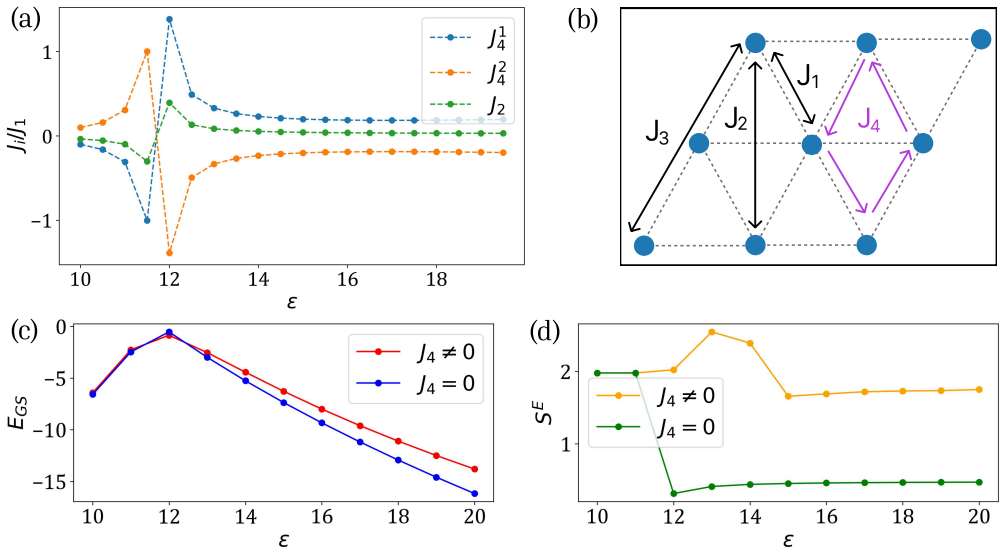

Figure 5.2: Details of the effective spin model for moiré TMD flakes: couplings J_2, J_4^1, and J_4^2 as a function of the dielectric constant ϵ for fixed twist angle $\theta = 3.5$ (a), geometry of the model and spin couplings (b). The ground state energy (c) and the bipartite entanglement entropy (d) in case with ($J_4 \neq 0$) and without ($J_4 = 0$) ring exchange interaction for the cylinder with dimensions $L_y = 4$, $L_x = 12$.

Figure 5.1(d) shows a variation from the single occupancy defined as:

$$\text{Var } \rho_{HF} = \frac{1}{N} \sum_{i}^{N} |\rho_i^E - 1|, \tag{5.1}$$

where where ρ_i^E is the electron density calculated for ith quantum dot. Value Var ρ_{HF} moves above zero at $\theta = 3.5$ for $\epsilon = 20$ and at $\theta = 4.0$ for $\epsilon = 10$, which is consistent with the energy spectrum analysis.

In our following analysis, we choose to fix the twist angle value to $\theta = 3.5$. At this twist, there is strong coupling between layers, yet the gap between Hubbard bands is finite for the whole range of dielectric constant $\epsilon = (10, 20)$. When this condition is met, we can obtain the effective spin Hamiltonian by applying the t/U expansion to the generalized Hubbard Hamiltonian (details

in the Appendix A). The obtained effective spin Hamiltonian has the form:

$$H = J_1 \sum_{<i,j>} (\bar{S}_i \cdot \bar{S}_j) + J_2 \sum_{\ll i,j \gg} (\bar{S}_i \cdot \bar{S}_j) + J_3 \sum_{\lll i,j \ggg} (\bar{S}_i \cdot \bar{S}_j) \\ + \sum_{\Diamond} J_4^1[(\bar{S}_i \cdot \bar{S}_j)(\bar{S}_k \cdot \bar{S}_l) + (\bar{S}_i \cdot \bar{S}_l)(\bar{S}_k \cdot \bar{S}_j)] + J_4^2(\bar{S}_i \cdot \bar{S}_k)(\bar{S}_j \cdot \bar{S}_l), \tag{5.2}$$

where J_1, J_2, J_3 are the couplings between the first, second, and third neighboring spins on the triangular lattice. Besides the two-spin interaction terms from the second-order perturbation theory, the fourth-order gives the four-spin ring exchange terms acting on rhombic plaquettes with couplings J_4^1, J_4^2 (Fig. 5.2(b)) [2, 256]. The J amplitudes are:

$$\begin{aligned}
J_1 &= -2X_1 + \frac{4\tilde{t}_1^2}{U_0 - U_1} - \frac{4(P_1 - X_1)\tilde{t}_1^2}{(U_0 - U_1)^2} + \frac{8\tilde{t}_1^4}{(U_0 - U_1)^3}\left(\frac{U_0 - U_1}{2U_0 - 3U_1 + U_2}\right. \\
&\quad \left. + \frac{4(U_0 - U_1)}{2U_0 - U_1 - U_2} + \frac{3(U_0 - U_1)}{U_0 - U_2} + \frac{2(U_0 - U_1)}{U_0 - U_3} - 11\right), \\
J_2 &= -2X_2 + \frac{4\tilde{t}_2^2}{U_0 - U_2} + \frac{8\tilde{t}_1^4}{(U_0 - U_1)^3}\left(1 - \frac{U_0 - U_1}{U_0 - U_2} + \frac{U_0 - U_1}{2U_0 - 3U_1 + U_2}\right), \\
J_3 &= -2X_3 + \frac{4\tilde{t}_3^2}{U_0 - U_3} - \frac{4\tilde{t}_1^4}{(U_0 - U_1)^3}\left(\frac{U_0 - U_1}{U_0 - U_3} - 2\right), \\
J_4^1 &= \frac{32\tilde{t}_1^4}{(U_0 - U_1)^3}\left(2 + \frac{U_0 - U_1}{U_0 - U_2} - \frac{U_0 - U_1}{2U_0 - U_1 - U_2}\right), \\
J_4^2 &= \frac{-32\tilde{t}_1^4}{(U_0 - U_1)^3}\left(1 + \frac{U_0 - U_1}{U_0 - U_2} - \frac{U_0 - U_1}{2U_0 - 3U_1 + U_2}\right).
\end{aligned} \tag{5.3}$$

Usually, ring exchange amplitudes J_4^1 and J_4^2 have the same absolute values and opposite signs. However, in the case of moiré TMD flakes, there is a small offset between them. Figure 5.2(a) shows that values of $J_4^{1,2}$ exceed the value of the next-nearest neighbors coupling in the whole range of parameter ϵ and even dominate over the first-neighbors coupling J_1 for $\epsilon = 12$. This suggests that the ring exchange interaction strongly influences the properties of the structure and ordering of spins.

5.2 Phase diagram

We consider a cylindrical geometry with periodic boundary conditions applied along the $\hat{y}$-direction and a fixed width of $L_y = 4$. Ground state and excited states are obtained with DMRG method implemented in TeNPy library [269]. The maximal bond dimension χ_{BD} from the convergence analysis is set to $\chi_{BD} = 2700$, for well converged ground state.

The initial analysis of the phase diagram as a function of the dielectric constant is presented in Fig. 5.2 (c). For $\epsilon \leq 11$, the J_1 amplitude is negative and the ground state is spin-polarized, as shown in Fig. 5.2 (a), where the ratios J_i/J_1 change sign near $\epsilon = 12$. When the ring-exchange amplitude is set to zero ($J_4 = 0$), the ground state energy E_{GS} reaches a maximum at $\epsilon = 12$, while the bipartite entanglement entropy $S_E = -\mathrm{tr}(\rho \ln \rho)$ drops significantly after the transition from the spin-polarized phase and then remains nearly constant over the entire range of ϵ values. In the full spin model with ring exchange included, the ground state energy behaves similarly, but the entanglement entropy shows a more interesting trend: it reaches its maximum at $\epsilon = 13$, and subsequently decreases and stabilizes for $\epsilon \geq 15$ (Fig. 5.2 (d)). The behavior of E_{GS} and S_E suggests that the spin ordering of the ground state may change in the vicinity of $\epsilon = 13$. In the following subsections, we characterize the antiferromagnetic phases of the model with ring-exchange interactions.

On the triangular lattice, geometric frustration gives rise to strong quantum fluctuations, which make the ground state distinctly different from the classical antiferromagnetic one and result in various correlated phases. To gain insight into the spin correlations of the ground state, we plot the real-space bond energies $\langle \mathbf{S}_i \cdot \mathbf{S}_j \rangle$ for three values of the dielectric constant $\epsilon = 12, 15, 17$ (Fig.5.3).The strength of each bond is represented by the line thickness between neighboring sites. In all three cases, the bonds along the short open boundaries in the $\hat{x}$-direction appear artificially enhanced due to edge effects; therefore, the interpretation should focus on the central region of the cylinder.

For $\epsilon = 12$ (Fig.5.3(a)), the bond energies are nearly uniform, with a maximal value $\langle \mathbf{S}_i \cdot \mathbf{S}_j \rangle_{MAX} = 0.116$. The absence of any clear modulation or long-wavelength periodicity suggests a quantum spin liquid–like state without broken lattice symmetries. By contrast, for $\epsilon = 15$ and $\epsilon = 17$ the maximal bond energies are significantly larger, $\langle \mathbf{S}_i \cdot \mathbf{S}_j \rangle_{MAX} = 0.451$ and $\langle \mathbf{S}_i \cdot \mathbf{S}_j \rangle_{MAX} = 0.453$ respectively, and the central region exhibits a distinct

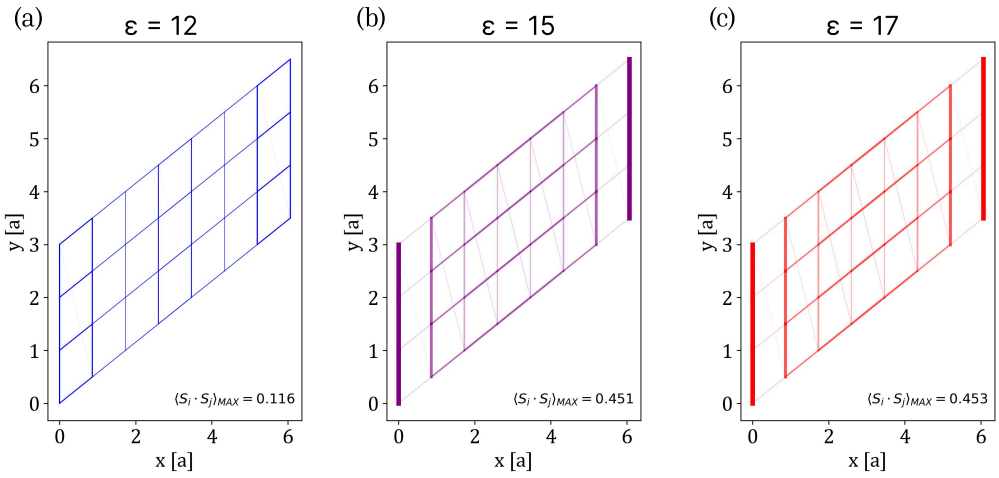

Figure 5.3: Comparison of real-space energy bonds $\langle \mathbf{S}_i \cdot \mathbf{S}_j \rangle$ between nearest-neighbors i, j for the dielectric constant $\epsilon = 12, 15, 17$ and system size $L_y = 4, L_x = 8$.

spatial modulation. The resulting pattern of alternating strong and weak bonds resembles a columnar or stripe-like arrangement, rather than a uniform distribution. The dominance of a single bond orientation points toward a nematic valence-bond solid (VBS) tendency, which will be analyzed in more detail in the following section.

5.2.1 Valence Bond Solid

The concept of a valence bond solid originates from Anderson's resonating valence bond (RVB) state, which was first proposed as a non-degenerate ground state for high-temperature superconductors [270]. In general, the non-magnetic ground state can be built entirely from valence bond states - pairs of spin-$\frac{1}{2}$ forming singlets. When all spins on the lattice are linked in pairs, the total spin of the ground state is also zero. The RVB state is constructed as a quantum position of all possible coverings of the lattice by singlets. In contrast to the liquid-like RVB state, a VBS is a static arrangement of singlets forming a crystalline pattern along certain bonds, which breaks the lattice symmetries while preserving spin-rotation invariance [271]. Such a ground state also lacks long-range entanglement. The VBS phase is a competing ground state in frustrated lattices to the Neél

ordering and spin liquids. In models, where quantum fluctuations destabilize Neél order, the VBS phase arises naturally [272]. Recent developments demonstrate that the continuous transition between Neél and VBS states can be described within a class of deconfined quantum criticality. In such cases, a transition occurs between two phases with distinct order parameters, and according to conventional Landau-Ginzburg-Wilson theory, it is predicted to be a first-order transition with a change in symmetry breaking. Instead, the transition is second-order and involves deconfined excitations coupled to the gauge field [273–276]. The VBS phase contains multiple competing ground states distinguished by the orientation and ordering of dimers, influenced by the underlying lattice geometry and the interaction range. On the triangular lattice, the most common patterns are the columnar (or stripe) order, where dimers align along a single lattice direction, thereby breaking the lattice rotational symmetry, and the plaquette ($\sqrt{3}\times\sqrt{3}$) order, where bonds exhibit a three-sublattice modulation. In the latter case, dimers tend to form around triangles or hexagons.

In general, breaking of the C_3 symmetry by the VBS ground state is signaled by a nonzero nematic parameter, which measures the preference for one bond orientation [277]. The nematic parameter is defined as

$$\Psi_{\text{nem}} = m_1 + e^{2\pi i/3} m_2 + e^{4\pi i/3} m_3, \tag{5.4}$$

with

$$m_\alpha = \frac{1}{N}\sum_i \left[D_\alpha(\mathbf{r}_i) - \frac{1}{3}\sum_{\beta=1}^{3} D_\beta(\mathbf{r}_i) \right], \qquad D_\alpha(\mathbf{r}_i) = \langle \mathbf{S}_i \cdot \mathbf{S}_{i+\mathbf{e}_\alpha} \rangle. \tag{5.5}$$

Here, $\mathbf{e}_\alpha$ with $\alpha = 1, 2, 3$ denote the three inequivalent nearest-neighbor directions,

$$\mathbf{e}_1 = (1, 0), \quad \mathbf{e}_2 = \left(\tfrac{1}{2}, \tfrac{\sqrt{3}}{2}\right), \quad \mathbf{e}_3 = \left(-\tfrac{1}{2}, \tfrac{\sqrt{3}}{2}\right). \tag{5.6}$$

In Fig. 5.4 (a), the nematic parameter is nonzero across the whole range of ϵ, which indicates that both QSL and VBS phases break the C_3 symmetry of the triangular lattice. To further investigate the long-range ordering pattern in the VBS phase, we compute the Fourier-resolved bond fields, defined as the momentum-space transform of the bond expectation values,

$$\Phi_\alpha(\mathbf{Q}) = \frac{1}{N}\sum_i e^{i\mathbf{Q}\cdot\mathbf{r}_i} D_\alpha(\mathbf{r}_i). \tag{5.7}$$

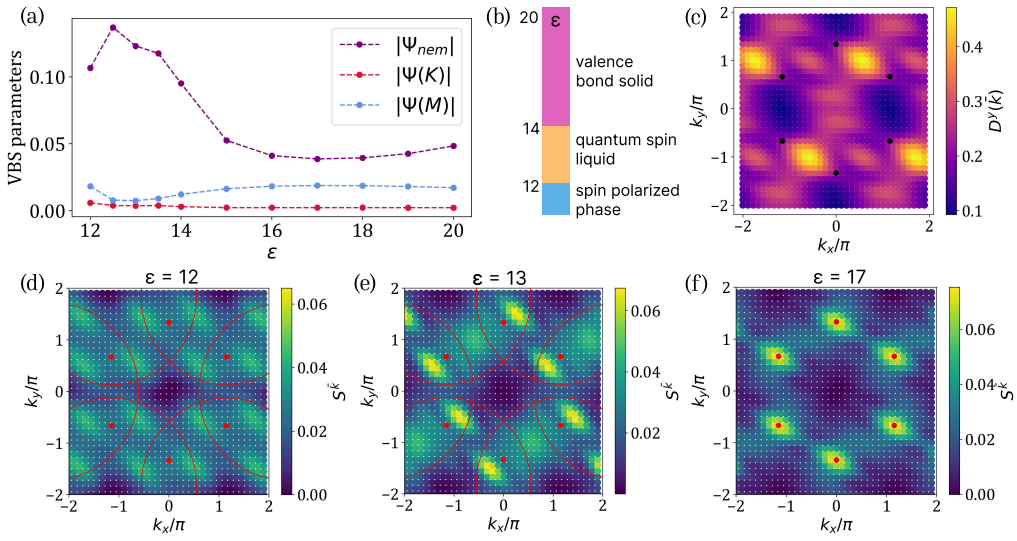

Figure 5.4: (a) Nematic parameter and dimer structure factor in high-symmetry points K and M as a function of the dielectric constant for a cylinder with length $L_x = 12$ (b) Proposed phase diagram for the moiré TMD heterostructure depending on the dielectric constant ϵ. (c) Dimer structure factor for $\epsilon = 17$. (d-f) Spin structure factor for $\epsilon = 12, 13, 17$, red circles denote spinon Fermi surface.

Analogously to the nematic parameter, we average over directions of the triangular lattice,

$$\Psi(\mathbf{Q}) = \Phi_1(\mathbf{Q}) + e^{2\pi i/3}\Phi_2(\mathbf{Q}) + e^{4\pi i/3}\Phi_3(\mathbf{Q}). \tag{5.8}$$

This quantity serves as the bond analogue of the spin structure factor and allows us to directly detect translational symmetry breaking in the bond sector.

Ordering patterns are characterized by nonzero values at distinct high-symmetry points $\mathbf{Q}$ of the Brillouin zone. In Fig. 5.4 (a) we look at $\Psi(\mathbf{K})$ and $\Psi(\mathbf{M})$. The non-zero value of the dimer field at the $\mathbf{K}$ point signals plaquette ordering and remains close to zero for all values of the dielectric constant. In contrast, the $\Psi(\mathbf{M})$ parameter increases for $\epsilon > 14$, suggesting the emergence of a VBS state with columnar ordering. Such a pattern breaks C_3 symmetry, which is consistent with the nonzero nematic parameter observed in this parameter range. Fig. 5.4 (c) shows the dimer structure factor calculated for the whole Brillouin zone, defined as:

$$D^{\alpha}(\mathbf{k}) = \sum_{i,j} \left(\langle \mathbf{D}_i^{\alpha} \mathbf{D}_j^{\alpha} \rangle - \langle \mathbf{D}_i^{\alpha} \rangle \langle \mathbf{D}_j^{\alpha} \rangle \right) e^{i\mathbf{k}\cdot(\mathbf{r}_i - \mathbf{r}_j)}. \tag{5.9}$$

For the lattice direction $\alpha = \hat{y} = \left(1/2, \sqrt{3}/2\right)$, the obtained map has a peak at the M point, which agrees with the columnar VBS. To further explore the nature of these ground states, we compute the static spin structure factor $S(\mathbf{k})$, which we introduce in the next section. Proposition of the phase diagram is presented in Fig.5.4 (b), where the VBS phase occupy range $14 < \epsilon < 20$.

5.2.2 Quantum Spin Liquid

From Anderson's idea of the RVB state comes also a concept of quantum spin liquid (QSL), which is a wider class of highly entangled ground states. Strong quantum fluctuations in these states suppress conventional Neél ordering down to absolute zero. Instead of aligning in a regular pattern, the spins remain disordered and fluctuate in a highly entangled manner. This QSL preserves all lattice symmetries and is often characterized by fractionalization of the spin degrees of freedom [133].

Building on these foundations, theoretical work in the 1980s and 1990s provided concrete examples of QSL in frustrated spin models. One of the

earliest proposed realizations was an anisotropic Heisenberg model on the triangular lattice [278]. The RVB ansatz was also used for the ground state of frustrated and doped square lattices, Heisenberg ladders, and square-planar lattices [279–283]. In 1987, the idea was revisited in the context of high-T_c superconductivity, where Anderson suggested that doping an RVB state could lead to unconventional superconductivity, which further intensified research into the nature of QSLs [284]. Over time, the QSL concept was developed by theoretical classification and more extensive numerical analyses. Spin liquids can be broadly classified into two main subclasses [285]: rigid spin liquids, which exhibit gapped excitations and are characterized by topological order (such as Z2-gapped and chiral spin liquids) [286, 287], and gapless spin liquids, such as U(1) Dirac or spinon Fermi surface phases [288, 289]. Critical behaviour of the gapless QSL phases can be analyzed within conformal field theory (CFT) framework [290]. On the numerical side, the development of the DMRG and tensor network methods accelerated research about QSL phases in realistic lattice models. Examples include the spin-1/2 $J_1 - J_2$ Heisenberg model on the square lattice [291], the triangular lattice [292,293], and kagome systems where the ground state appears consistent with a gapped Z_2 spin liquid [294]. These computational developments established QSLs as phases competing with Neél order and the VBS in strongly frustrated magnets. Some theoretical works [295, 296] suggest that the gapless spin liquid occurs at the critical point between Neél and VBS phases. The transition, as was mentioned in the previous section, is described in the framework of deconfined quantum criticality, where low-energy degrees of freedom are fractionalized spinons coupled to an emergent gauge field, which are also ingredients that define the spin liquid. When spinons condense, it leads to Neél order, and when they confine, the VBS phase arises. In this sense, DQCP not only describes a route between two different symmetry-breaking states, but also explains the occurrence of the gapless spin liquid between them.

From the plots of real-space bond energies and the increased entanglement entropy, we identify a candidate QSL state emerging in the dielectric constant range $12 \leq \epsilon \leq 14$. To further explore the nature of these ground states, we compute the static spin structure factor $S(\mathbf{k})$, defined as

$$S(\mathbf{k}) = \sum_{i,j} \left(\langle \mathbf{S}_i \cdot \mathbf{S}_j \rangle - \langle \mathbf{S}_i \rangle \langle \mathbf{S}_j \rangle \right) e^{i\mathbf{k}\cdot(\mathbf{r}_i - \mathbf{r}_j)}. \tag{5.10}$$

Figure ... shows $S(\mathbf{k})$ maps for $\epsilon = 12$ (c) and $\epsilon = 13$ (d). For stronger interactions ($\epsilon = 12$), the spin structure factor exhibits multiple broad peaks

distributed along a "$2k_F$" surface, indicated by the dashed red lines as a visual guide. The positions of these peaks correspond to scattering processes of spinons between opposite points of the Fermi surface. From the peak locations, the estimated Fermi surface radius is $k_F = \sqrt{4\pi/\sqrt{3}}$, consistent with the presence of a spinon Fermi surface, which is characteristic of a gapless quantum spin liquid phase. Moreover, for $\epsilon = 12$, the nematic parameter Ψ_{nem} is finite, suggesting that the QSL phase spontaneously breaks lattice rotational symmetry, thereby realizing a nematic spin liquid. Such coexistence of gapless fractionalized excitations with broken point-group symmetry has been reported in other frustrated models [297–299], and may reflect the strong competition between spin-liquid and valence-bond ordering tendencies on the triangular lattice. For $\epsilon = 13$, the overall $2k_F$ structure remains visible, but the distribution of spectral weight becomes anisotropic: while some peaks weaken, others are enhanced. This selective strengthening of particular scattering channels indicates a deformation of the spinon Fermi surface. Combined with the enhanced nematicity observed in the bond-energy patterns, this suggests that the gapless QSL develops competing correlations, with signatures of an instability toward valence-bond solid ordering.

5.3 Influence of the ring exchange interaction term

An important feature of the effective spin model for moiré TMD flakes is the strong ring exchange interaction. Usually, spin models are considered only with Heisenberg-like two-spin coupling between nearest and next-nearest neighbors. In order to better understand the influence of the four-spin ring exchange on the ground state of the system, we calculate spin $S(\mathbf{k})$ and dimer $D^{\hat{x}}(\mathbf{k})$ structure factors along the Γ-K-M-Γ path, while fixing parameters $J_4^1 = J_4^2 = 0$. When the ring exchange term is absent, the spin structure factor has two peaks at the K and M point, while the dimer structure factor reaches a maximum at the Γ point (Fig. 5.5(a,b)). These signatures are consistent with an antiferromagnetic stripe phase, in which spins form collinear patterns with alternating ferromagnetic rows [300]. By contrast, including ring exchange suppresses these features, and correlations are now nearly uniform along the whole path, which is in agreement with a symmetry-preserving QSL state. The difference between these phases is also evident when plotting

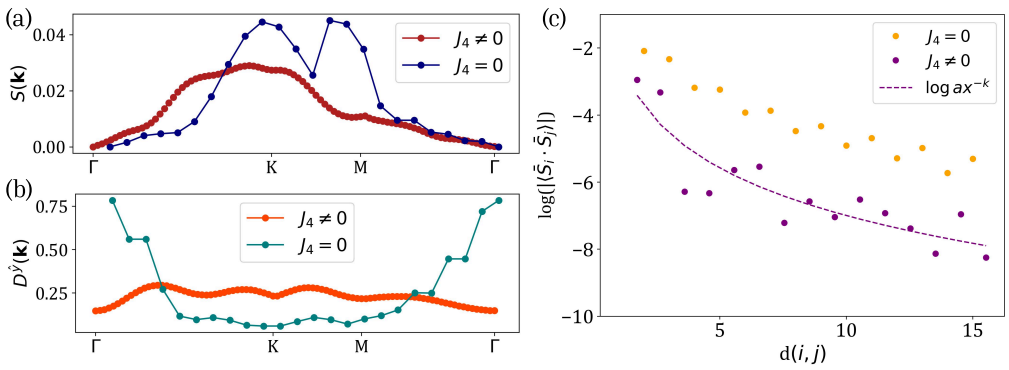

Figure 5.5: (a) Spin and (b) dimer structure factors of the moiré TMD flake with dimensions $L_y = 4$ $L_x = 8$ for $\epsilon = 12$. (c) Real space correlations as a function of the distance $d(i, j)$ between points i and j. Results are obtained for two models: with included ring exchange interaction ($J_4 \neq 0$) and only with two-spin terms ($J_4 = 0$).

real-space correlations. Figure 5.5(c) shows spin-spin correlations calculated between site $(x, y)_0 = (0, 0)$ and other sites along one direction on the cylinder of length $L_x = 16$ with dielectric constant $\epsilon = 12$. Without ring exchange, the correlations decay exponentially with distance while oscillating due to the stripe order. When the ring exchange is included in the model, the decay instead follows a power law with oscillations, characteristic of a gapless quantum spin liquid phase.

5.4 Entanglement analysis

To further characterize the gapless QSL state, we are using entanglement entropy, which is a useful tool for probing correlations and critical behavior in quantum many-body systems. For a bipartition of a system into subsystems A and B, the von Neumann entanglement entropy of subsystem A is defined as:

$$S^E(A, B) = -\mathrm{Tr}\rho_A \ln \rho_A, \tag{5.11}$$

where $\rho_A = \mathrm{Tr}_B \rho_{AB}$ is the reduced density matrix obtained by tracing out subsystem B.

We consider a cylinder with $N = L_x \cdot L_y$ sites and divide it into subsys-

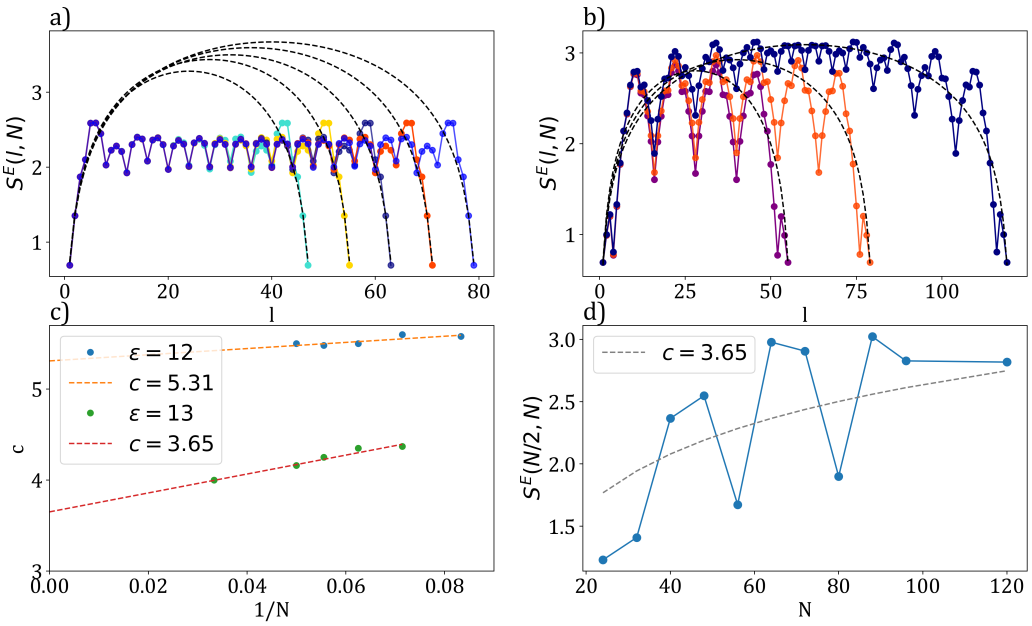

Figure 5.6: Entanglement entropy of cylinders with width $L_y = 4$. (a) Subsystem entropy $S^E(l, N)$ for $\epsilon = 12$, showing logarithmic growth consistent with CFT scaling. (b) Subsystem entropy for $\epsilon = 13$, with reduced slope indicating a smaller central charge. (c) Finite-size extrapolation of fitted central charges in thermodynamic limit, yielding $c^T = 5.31$ at $\epsilon = 12$ and $c^T = 3.65$ at $\epsilon = 13$. (d) Bipartite entropy $S^E(N/2, N)$ at $\epsilon = 13$, dashed line shows analytic formula for central charge obtained from subsystem analysis.

tems of length l and $N - l$ along a zigzag path connecting all sites. The entanglement entropy of a subsystem of length l is computed using the von Neumann definition and fitted to the conformal field theory (CFT) scaling form [301, 302]:

$$S^E(l, N) = \frac{c}{6} \ln \left[\frac{2N}{\pi} \sin \left(\frac{l\pi}{N} \right) \right] + A, \tag{5.12}$$

where c is the central chargem and A is a non-universal constant. While a conventional central charge c is not defined in 2+1D, each patch of the Fermi surface contributes effectively as a 1+1D gapless mode associated with the number of gapless modes [290, 303]. Fig. 5.6(a) shows results for $\epsilon = 12$ for cylinders with lengths $L_x = 12, 14, 16, 18, 20$. In gapless systems such

as the QSL, entanglement entropy converges more slowly near the center of the system due to long-range correlations, even when the DMRG bond dimension is as large as $\chi_{BD} = 3000$, which is otherwise sufficient to achieve well-converged ground-state energies. Nevertheless, focusing on data near the edges, we can fit Eq. 5.12 and extract a central charge $c \approx 5.4$. To assess finite-size effects, the central charges obtained for different system sizes are plotted against $1/N$. The thermodynamic limit value obtained from a linear extrapolation equals $c^T \approx 5.31$, which indicates the presence of five gapless modes in the system. For a cylinder with width $L_y = 4$, one would theoretically expect six gapless modes corresponding to three bands crossing the spinon Fermi surface. The reduction to five modes is consistent with the partial gapping of one mode due to coupling to the emergent U(1) gauge field, as predicted by spinon–gauge theory descriptions of U(1) QSLs. A similar analysis for $\epsilon = 13$ shows a significant reduction in central charge (Fig 5.6(b)). Here, results are presented for $L_x = 12, 20, 30$ for clarity. Linear extrapolation of the fitted central charge gives $c^T \approx 3.65$, indicating a decrease in the number of effective gapless modes. This is consistent with the system approaching the VBS phase, and suggests the continuous nature of the QSL-VBS transition. We also consider the bipartite entanglement entropy for cylinders of length L_x and total number of sites N, which scales for a gapless system like:

$$S^E(N/2, N) = S_0 + \frac{c}{6} \ln\left(\frac{2N}{\pi}\right), \tag{5.13}$$

where S_0 is a constant capturing non-universal contributions. Figure 5.6(d) shows the bipartite entanglement entropy for $\epsilon = 13$ as a function of system size. While finite-size oscillations are occurring, the overall logarithmic increase is captured by Eq. 5.13 using the fitted central charge $c \approx 3.65$.

Chapter 6

Haldane phase in mixed-size nanographene chains

Among various graphene nanostructures, chains of triangular graphene quantum dots (TGQDs) attracts attention as possible quantum simulators for one-dimensional spin chains. TGQDs with zigzag edges act as localized spin sites due to the sublattice imbalance, producing zero-energy modes at the half-filling [215, 218]. The spin-polarized ground state is then stabilized by strong on-site Coulomb interactions. The number of those zero-modes depends on the size of TGQD.

Early work treated TGQDs mainly as theoretical models because atomic-precision synthesis was challenging. The situation changed with advances in bottom-up and on-surface synthesis techniques, which made it possible to fabricate atomically precise triangular nanographenes with controlled edge terminations. The smallest triangular fragment, phenalenyl (C_{13}) is a spin-1/2 radical [304], and the second smallest, triangulene, is a spin-1 (triplet) nanographene. First successful on-surface synthesis of unsubstituted triangulene was done in 2017 by Pavliček et al. [305], and the experimental evidence of localized edge states was provided with noncontact atomic force microscopy. The unsubstituted phenalenyl was realized on the surface in later works, and its $S = 1/2$ ground state was demonstrated with Kondo spectroscopy [306].

When TGQDs are coupled into chains, inter-dot tunneling mediates effective exchange interaction between the localized zero-modes, mapping the system onto effective Heisenberg (or bilinear–biquadratic) spin chains. On-surface approaches have been used to build 1D arrays of TGQDs, scanning

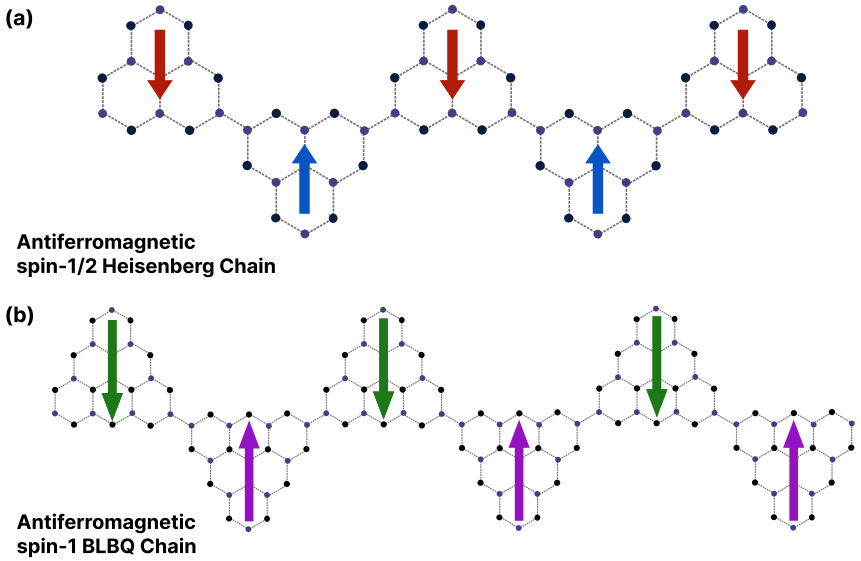

Figure 6.1: Nanographene chains consisting of (a) 13-atom TGQDs (phenalenyls) and (b) 22-atom TGQDs (triangulenes).

tunneling spectroscopy, and non-contact AFM provide direct access to bulk gaps, and fractionalized edge states. Chains built from spin-1/2 units realize the antiferromagnetic Heisenberg model with a gapless or small-gap spectra due to finite chain length (Fig. 6.1 (a)) [307]. Probing spin excitations with inelastic electron tunneling spectroscopy shows a power-law decay of the spin gap with increasing chain length [65]. Also, on-surface synthesis allows the construction of spin-1/2 Heisenberg chains with alternating-exchange couplings between sites. Such a model has a non-trivial topological ground state in the thermodynamic limit and in-gap spin-1/2 edge excitations [308]. This experimental setting allows for an effectively one-dimensional model with tunable topological phases.

Chains of triangulenes (Fig. 6.1 (b)) are also realized with on-surface synthesis, and they provide a platform to simulate a one-dimensional spin-1 model. Theory and experiment indicate a superexchange interaction as the origin of their effective antiferromagnetic coupling [3], and that the low-energy physics is well captured by bilinear–biquadratic spin-1 models [309]. In recent realization, gapped bulk excitation was observed, as well as fraction-

alized spin-1/2 edge states, which reflect the symmetry-protected, topological Haldane phase [310].

6.1 Triangulene chains

The theoretical description of the triangulene chains begins with the properties of its fundamental building block: the dimer, consisting of two connected triangular quantum dots. This system contains $N_c = 44$ carbon atoms and, as in other graphene nanostructures, its single-particle properties are described within the tight-binding model restricted to p_z orbitals:

$$H_{tb} = \sum_{i,l,\sigma} t_{il} c^\dagger_{i\sigma} c_{l\sigma}, \tag{6.1}$$

where $c^\dagger_{i\sigma}$ and $c_{i\sigma}$ are creation and annihilation operators of a p_z electron on site i and with spin σ.

We want to include electron-electron interactions, however the system size exceeds computational resources. Solving Eq. 6.5 exactly for $N_e = 44$ electrons occupying $N_{st} = 44$ states is impossible due to the exponential Hilbert-space growth. Thus we will divide Hilbert space into two parts, one that will describe frozen electron within Hartree-Fock method and the second one within completely active space (CAS) treated within exact diagonalization method [311, 312]. The Hartree-Fock (HF) equation takes the form:

$$\begin{aligned} H_{HF} &= \sum_{i,l,\sigma} t_{il\sigma} c^\dagger_{i\sigma} c_{l\sigma} + \sum_{i,l,\sigma} \sum_{j,k,\sigma'} \left(\langle ij| V |kl\rangle - \langle ij| V |lk\rangle \delta_{\sigma\sigma'} \right) \left(\rho_{jk\sigma'} - \rho^0_{jk\sigma'} \right) c^\dagger_{i\sigma} c_{l\sigma} \\ &= \sum_{i,l,\sigma} \tilde{t}_{il\sigma} c^\dagger_{i\sigma} c_{l\sigma}, \end{aligned} \tag{6.2}$$

where the hopping parameters $t_{il\sigma}$ without corrections are taken as $t_1 = -2.8$ eV, $t_2 = -0.1$ eV, and $t_3 = -0.07$ eV for the first, second, and third nearest neighbors, respectively. Here $\rho^0_{jk\sigma'}$ are the density-matrix elements of infinite graphene (Ref. [311]), while $\rho_{jk\sigma'}$ are those of the finite system.

The Coulomb matrix elements $\langle ij| V |kl\rangle$ are defined in the basis of p_z Slater orbitals $\phi_i(\mathbf{r})$:

$$\phi_i(\mathbf{r}) = \sqrt{\left(\frac{\xi^5}{32\pi} \right)} z e^{-\frac{\xi}{2}|\mathbf{r}-\mathbf{r}_i|}, \tag{6.3}$$

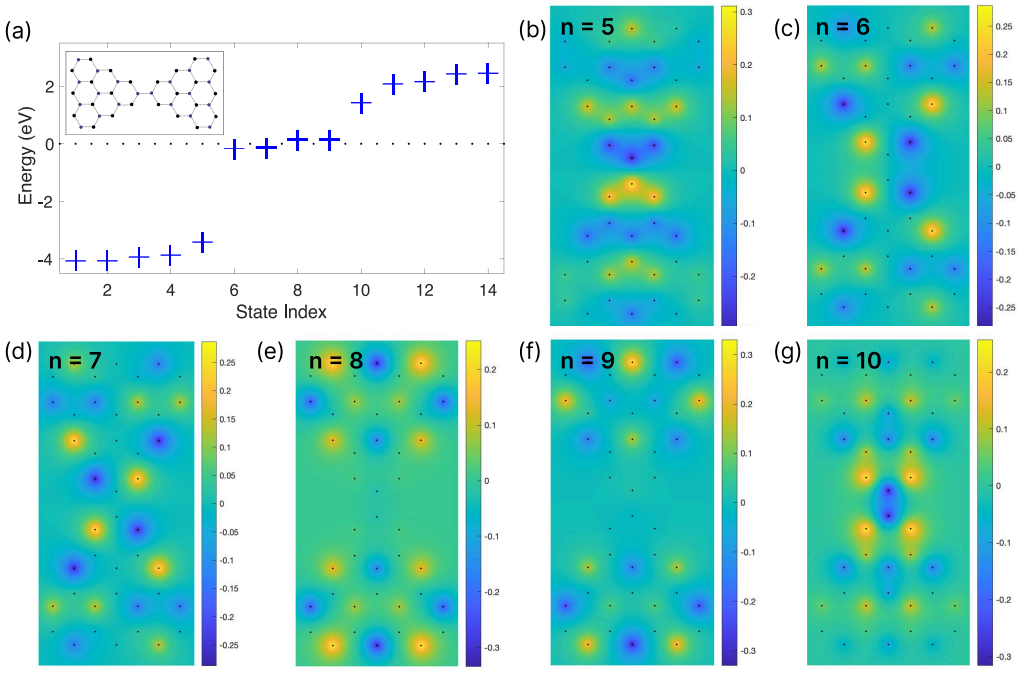

Figure 6.2: (a) Single-particle spectrum obtained from Hartree-Fock calculations for the triangulene dimer. (b-g) Hartree-Fock wavefunctions of six states with indices $n = 5 \ldots 10$.

with $\xi = 3.25$, and $\mathbf{r}_i$ denoting the position of the carbon atom. The Coulomb interaction reads

$$\langle ij| V |kl\rangle = \int\int d\mathbf{r}_1 d\mathbf{r}_2 \phi_i^*(\mathbf{r}_1)\phi_j^*(\mathbf{r}_2)\frac{2R_y}{\kappa|\mathbf{r}_1 - \mathbf{r}_2|}\phi_k(\mathbf{r}_2)\phi_l(\mathbf{r}_1), \tag{6.4}$$

where the dielectric constant $\kappa = 3$ corresponds to screening from the gold substrate, and R_y is the Rydberg constant.

The single-particle energy spectrum obtained from self-consistent HF calculations is shown in Fig. 6.2 (a). Four states lie near the Fermi level and are separated from the rest by finite gaps. These are dispersed zero-energy states obtained before within nearest neighbor tight-binding model. The dispersion is due to farther hoppings and electron-electron interactions included within a mean-field approximation. Their wavefunctions, together with one state above and one below the degenerate shell, are plotted in Fig. 6.2(b–g). Two states with indices $n = 8, 9$ (Fig. 6.2(e, f)) are localized at the two sepa-

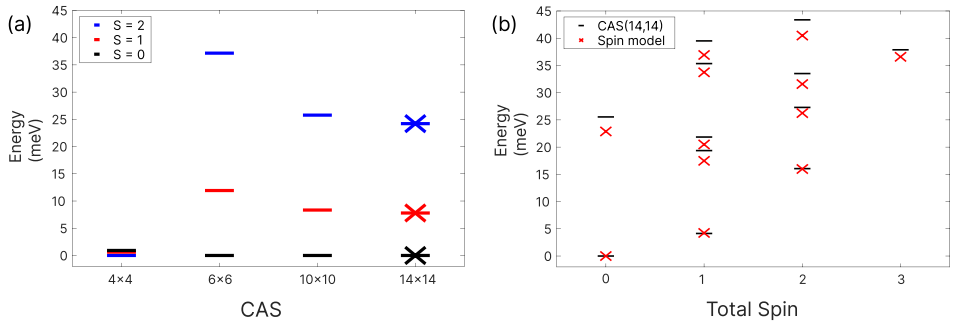

Figure 6.3: (a) Many-body spectrum of the triangulene dimer as a function of CAS size. Crosses denote the three lowest-energy states of the spin-1 BLBQ Hamiltonian with $J = 8.21$ meV and $\beta = 0.016$. The inset shows triangulene dimer structure. (b) Many-body spectrum of a four-triangulene chain compared with the corresponding BLBQ model of four spin-1 sites. Figure adapted from Ref. [3].

.

rated ends of the dimer, but the other two states from the shell with indices $n = 6, 7$ (Fig. 6.2(c, d)) strongly hybridize with the inter-triangulene region.

We transform the many-body Hamiltonian to the basis of HF orbitals, it becomes:

$$H = \sum_{p,\sigma} \epsilon^{HF}_{p\sigma} b^{\dagger}_{p\sigma} b_{p\sigma} - \sum_{p,q,\sigma} \tau_{pq\sigma} b^{\dagger}_{p\sigma} b_{q\sigma} + \frac{1}{2} \sum_{p,q,r,s,\sigma,\sigma'} \langle pq| V |rs\rangle \, b^{\dagger}_{p\sigma} b^{\dagger}_{q\sigma'} b_{r\sigma'} b_{s\sigma}, \tag{6.5}$$

where $\epsilon^{HF}_{p\sigma}$ are Hartree-Fock energies, and $b^{\dagger}_{p\sigma}/b_{p\sigma}$ are creation/annihilation operators of the electron with spin σ on the HF orbital p. To avoid double counting of interaction already included at the mean-field level, the Hamiltonian contains the $\tau_{pq\sigma}$ term [312]. We consider four different active-space sizes: CAS(4,4), CAS(6,6), CAS(10,10), and CAS(14,14), where CAS(N_{st}, N_e) denotes the number of orbitals and electrons retained, where $N_{st}/2$ taken above and $N_{st}/2$ taken below the dotted line shown in Fig. 6.2 (a). For CAS(4,4), the ground state is spin-polarized with total spin $S = 2$, consistent with Hund's rule for four electrons occupying four degenerate orbitals (Fig. 6.3 (a)), but violating Lieb's theorem [217]. We didn't obtain the expected order of states characteristic for a two-spin Heisenberg model, with $S = 0$ (singlet) as the ground state, $S = 1$ (triplet) the first excited state, and with the highest energy $S = 2$ (quintuplet). Only when additional states

outside the degenerate shell are included for CAS(6,6), the antiferromagnetic ground state with $S = 0$ occurs. which shows that inter-triangulene states are required for correctness of the calculations. These states enable superexchange processes, allowing electrons to virtually hop between triangulenes via intermediate orbitals [3]. The resulting low-energy spectrum finally resembles that of a spin-1 chain, with the antiferromagnetic superexchange being crucial for its emergence.

The CAS(14,14) energy spectrum obtained from the CI procedure can be fitted to the spin-1 bilinear-biquadratic (BLBQ) Hamiltonian:

$$H_{BLBQ} = J \sum_i \left[\mathbf{S}_i \cdot \mathbf{S}_{i+1} + \beta \left(\mathbf{S}_i \cdot \mathbf{S}_{i+1} \right)^2 \right], \tag{6.6}$$

with J and β denoting bilinear and biquadratic exchange couplings between neighboring spin sites. From the fit we obtain $J = 8.21$ meV and $\beta = 0.016$. In Fig. 6.3 (b), we compare the CI spectrum of a four-triangulene chain with that of the spin-1 BLBQ Hamiltonian using these parameters. For CAS(14,14), the basis includes eight degenerate-shell states and six inter-triangulene states. The agreement between our two models and experimental results [313] in the ordering of ground and excited states, as well as in the gap between the first two excited states, demonstrates the validity of the spin-1 description. Minor discrepancies in higher excited states can be attributed to the finite CAS truncation.

6.2 Mixed-size TGQDs model

Motivated by the possibility of combining triangular graphene quantum dots (TGQDs) of different sizes within a single nanostructure, we study chains with mixed spin sites. In particular, a chain with alternating spin-1 and spin-$\frac{1}{2}$ sites carries a finite magnetic moment, since ferromagnetic coupling between spin-1 sites dominates over the coupling between spin-$\frac{1}{2}$ sites with opposite sign. The resulting ground state is ferrimagnetic, characterized by partial spin polarization. By contrast, we propose the chain geometry, where spin-1 sites are separated by an even number of spin-$\frac{1}{2}$ sites, and the ground state is expected to have the lowest total spin. Such structures can be experimentally realized in TGQD chains where triangulenes are separated by at least one pair of phenalenyls. In what follows, we analyze the ground-state properties of this system and compare them with other well-established

one-dimensional phases.

As discussed in the previous section, capturing the correct exchange coupling between connected triangulenes requires including additional intermediate states. This significantly increases the numerical cost. An alternative approach, proposed in Ref. [314], introduces an effective direct coupling between adjacent triangulenes by enhancing the third-neighbor hopping to $t_3 = -0.33$ eV. This approximation allows one to use only degenerate-shell states and reduce the size of the many-body Hilbert space. We want to formulate the effective model for mixed-size nanographene chains to reduce the size of the Hilbert space by restricting it to the zero-energy state subspace. For this purpose, we rotate the many-body Hamiltonian to the basis of C_3-symmetric modes. The considered many-body Hamiltonian is the effective t_3 model mentioned above, which is given in real-space basis as:

$$H_{t_3} = \sum_{i,l,\sigma} t_{il\sigma} c^\dagger_{i\sigma} c_{i\sigma} + \frac{1}{2} U \sum_{i,\sigma\neq\sigma'} c^\dagger_{i\sigma} c^\dagger_{i\sigma'} c_{i\sigma'} c_{i\sigma}, \tag{6.7}$$

where $t_{il\sigma}$ hopping parameters are nonzero for the first, second, and third nearest-neighbors with values $t_1 = -2.8$ eV, $t_2 = -0.1$ eV, $t_3 = -0.33$ eV, respectively. We rewrite the Hamiltonian as a sum of contributions from individual TGQDs and their couplings:

$$H_{t_3} = H_1 + H_2 + H_3 + V_{12} + V_{23} \tag{6.8}$$

where index $\triangle = 1$ denotes a triangulene and $\triangle = 2, 3$ the two 13-atom TGQDs in the unit cell. The Hamiltonian of a single nanographene is:

$$H_\triangle = \sum_{i,l\in\triangle,\sigma} t_{il\sigma} c^\dagger_{i\sigma} c_{i\sigma} + \frac{1}{2} U \sum_{i\in\triangle,\sigma\neq\sigma'} c^\dagger_{i,\sigma} c^\dagger_{i,\sigma'} c_{i,\sigma'} c_{i,\sigma}, \tag{6.9}$$

and the inter-TGQD coupling is

$$V_{\triangle\triangle'} = t_3 \sum_{i\in\triangle,l\in\triangle',\sigma} c^\dagger_{i\sigma} c_{i\sigma} + h.c.. \tag{6.10}$$

We now express H_{t_3} Hamiltonian in the eigenbasis of a single triangle $H_\triangle$, which respects C_3 symmetry. The triangulene sites can be grouped into three subsets, A, B, and C, related by C_3 rotations (Fig. 6.4(a)). A single-particle wavefunction can be written in the basis of p_z Slater orbitals $\phi_i(r)$ as:

$$\psi_l(r) = \sum_i A^l_i \phi_i(r), \tag{6.11}$$

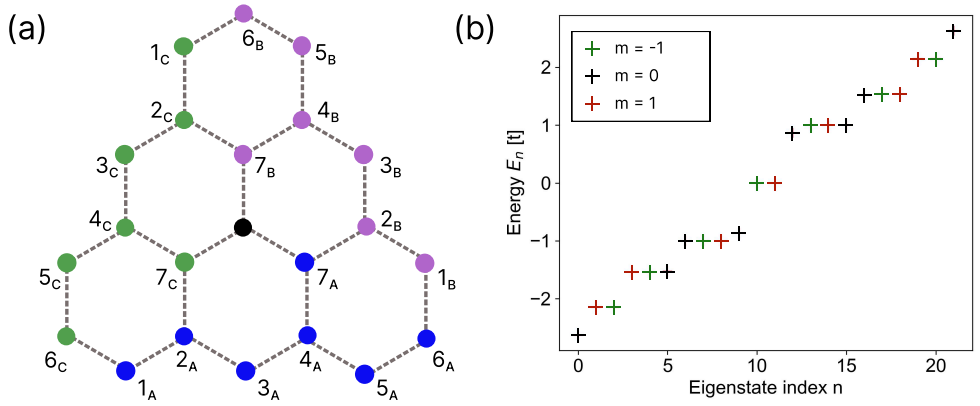

Figure 6.4: (a) Division of triangulene sites into three subgroups, which transforms into itself under C_3 rotations. (b) Single-particle energy states of triangulene labeled by angular momentum m.

where l denotes single-particle states and i is the index of carbon atom. Now, we can divide the p_z orbitals into three groups:

$$\psi_l(r) = \sum_{i\in A} A_i^l \phi_i(r) + \sum_{i\in B} A_i^l \phi_i(r) + \sum_{i\in C} A_i^l \phi_i(r) + A_0^l \phi_0(r). \tag{6.12}$$

Each sector can be indexed by the angular momentum $m = 1, 2, 3$. The position of the central carbon atom is invariant under rotation and must be treated separately. Then, we construct a new, rotated basis, consisting of Wannier-like orbitals:

$$|j\rangle = \frac{1}{\sqrt{3}} \left(|j_A\rangle + \exp\left(i\frac{2\pi}{3}m\right) |j_B\rangle + \exp\left(i\frac{4\pi}{3}m\right) |j_C\rangle \right), \tag{6.13}$$

where $m = 1, 2, 3$ labels angular momentum sectors. The new basis states are a linear combination of three sites from three subspaces related to each other by a phase factor. The Hamiltonian H_1 matrix elements in this basis are:

$$\langle i| H |j\rangle = \frac{1}{3} \sum_{l,k=A,B,C} e^{i\frac{2\pi}{3}(l-k)m} \langle i_k| H_1 |j_l\rangle , \tag{6.14}$$

where indices l, k in the exponential maps to integers: $A = 1$, $B = 2$, and $C = 3$. And for the central site it is:

$$\langle 0| H_1 |j\rangle = \frac{1}{\sqrt{3}} \sum_{l=A,B,C} e^{i\frac{2\pi}{3}lm} \langle 0| H_1 |j_l\rangle . \tag{6.15}$$

Restricting to zero-energy modes, we rotate the Hamiltonian H_{t_3} (Eq. 6.7) into the C_3-symmetric basis. The effective Hamiltonian of the full chain becomes

$$H_{eff} = \sum_{\triangle,\triangle',\alpha,\alpha'} \tau_{\triangle\alpha,\triangle'\alpha'} b^\dagger_{\triangle\alpha\sigma} b_{\triangle'\alpha'\sigma} + \frac{1}{2} \sum_{\substack{\triangle,\alpha_1,\alpha_2,\alpha_3,\alpha_4 \\ \sigma,\sigma\neq\sigma'}} U_\triangle b^\dagger_{\triangle\alpha_1\sigma} b^\dagger_{\triangle\alpha_2\sigma'} b_{\triangle\alpha_3\sigma'} b_{\triangle\alpha_4\sigma}, \tag{6.16}$$

where α labels zero-energy modes within each triangle $\triangle$. The kinetic and interaction terms are:

$$\tau_{\triangle\alpha,\triangle'\alpha'} = \langle \triangle\alpha | \, t_3 \sum_{\langle\langle i,l\rangle\rangle,\sigma} c^\dagger_{i\sigma} c_{l\sigma} \, | \triangle'\alpha' \rangle \tag{6.17}$$

and

$$U_\triangle(\alpha_1,\alpha_2,\alpha_3,\alpha_4) = \langle \triangle_1\alpha_1, \triangle_2\alpha_2 | \, \frac{1}{2} U \sum_{i,\sigma\neq\sigma'} c^\dagger_{i\sigma} c^\dagger_{i\sigma'} c_{i\sigma'} c_{i\sigma} \, | \triangle_3\alpha_3, \triangle_4\alpha_4 \rangle \, . \tag{6.18}$$

The Hubbard term acts locally, thus we can assume $\triangle_1 = \triangle_2 = \triangle_3 = \triangle_4 = \triangle$, so we can simplify our notation to:

$$U_\triangle = \frac{1}{2} U \, \langle \alpha_1,\alpha_2 | \sum_{i,\sigma\neq\sigma'} c^\dagger_{i\sigma} c^\dagger_{i\sigma'} c_{i\sigma'} c_{i\sigma} \, | \alpha_3,\alpha_4 \rangle \, . \tag{6.19}$$

Using Eq.6.12 and Eq.6.13, the wavefunction of state $|\triangle,\alpha\rangle$ is:

$$|\triangle,\alpha\rangle = \sum_j C_j^{\triangle\alpha} \, |j\rangle = \frac{1}{\sqrt{3}} \sum_j \sum_{l=A,B,C} C_j^{\triangle\alpha} e^{i\frac{2\pi}{3} l\alpha} \, |j_l\rangle \, , \tag{6.20}$$

where $C_j^{\triangle\alpha}$ are coefficients obtained from single-particle calculations in each angular momentum sector. The resulting on-site interaction reads

$$U_\triangle = \frac{1}{9} \sum_j (C_j^{\alpha_1})^* (C_j^{\alpha_2})^* C_j^{\alpha_3} C_j^{\alpha_4} \sum_{l=A,B,C} e^{i\frac{2\pi}{3} l(-\alpha_1-\alpha_2+\alpha_3+\alpha_4)}. \tag{6.21}$$

Mixed-size nanographene chains contain two types of TGQDs with different numbers of zero-energy modes. The smaller TGQD (phenalenyl radical) has a single mode α, corresponding to spin-$\frac{1}{2}$, while triangulene has two

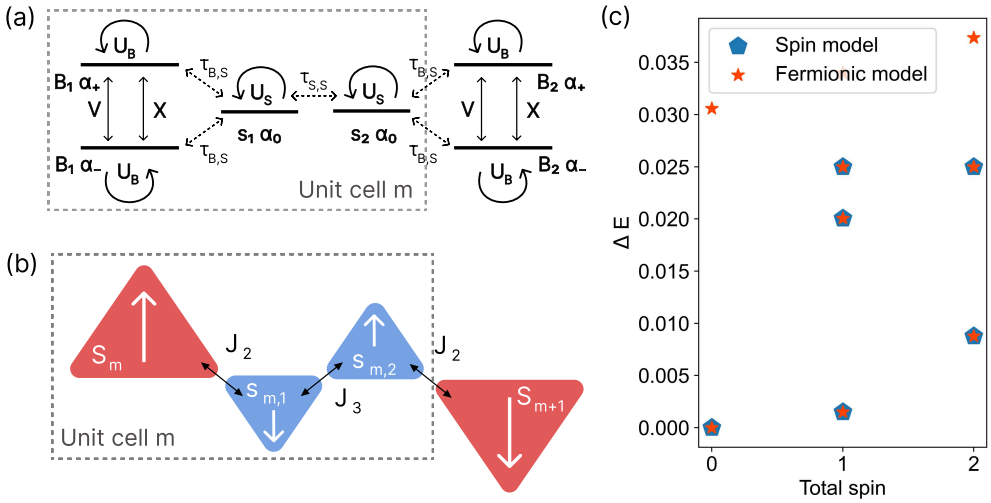

Figure 6.5: (a) Fermionic model of a mixed-size nanographene chain. (b) Effective spin-1/spin-$\frac{1}{2}$ representation. (c) Comparison between the lowest-energy spectra of the two models for one unit cell terminated with a triangulene (BSSB).

modes $\alpha = \pm 1$, corresponding to spin-1. The Coulomb terms obey the selection rule $\alpha_1 + \alpha_2 = \alpha_3 + \alpha_4$, ensuring momentum conservation. For the small TGQD, the only solution is $\alpha_1 = \alpha_2 = \alpha_3 = \alpha_4$, yielding an on-site interaction $U_S = 0.824$ eV. For triangulene, we have:

$$U_{\triangle} = \frac{1}{3}\sum_{j}(C_j^{\alpha_1})^*(C_j^{\alpha_2})^* C_j^{\alpha_3} C_j^{\alpha_4}(\delta_{\alpha_1+\alpha_2,\alpha_3+\alpha_4}), \tag{6.22}$$

which gives equal amplitudes for on-site U_B, direct $V = U_{\triangle}(\alpha_i, \alpha_j, \alpha_j, \alpha_i)$, and exchange $X = U_{\triangle}(\alpha_i, \alpha_j, \alpha_i, \alpha_j)$ interactions between the α_+ and α_- modes: $U_B = V = X = 0.459$ eV [315].

Next, we calculate the inter-TGQD hopping term:

$$\tau_{\triangle\alpha,\triangle'\alpha'} = \frac{t_3}{3}\sum_{\langle\langle i\in\triangle, j\in\triangle'\rangle\rangle}\sum_{\sigma}(C_i^{\alpha})^* C_j^{\alpha'}\sum_{k,l} e^{-i\frac{2\pi}{3}k\alpha} e^{i\frac{2\pi}{3}l\alpha'} \tag{6.23}$$

There are two kinds of hopping: between two smaller TGQDs and between big and small TGQDs. In the first case, the hopping does not depend on the

α since each small triangle has only one zero-energy mode, and has amplitude $\tau_{S,S} = 0.11$ eV. The electron hopping between mixed-size triangles obtains a complex phase depending on the mode $\alpha = +1, -1$, and has amplitude $\tau_{B\pm,S} = -0.0712 \pm 0.0411$ eV. A schematic representation of the fermionic model is shown in Fig. 6.5 (a)

Derivation of the effective Hubbard Hamiltonian enables us to study magnetic properties of chains. Due to the fact, that we are interested in charge neutral system with one electron per site and $U \gg \tau$, we can reduce Hamitonian to effective spin model. Using second-order perturbation theory, we obtain the effective exchange couplings: between two spin-$\frac{1}{2}$ sites, $J_3 = \frac{4|\tau_{S,S}|^2}{U_S} = 58.7$ meV, and between a spin-1 and a spin-$\frac{1}{2}$ site

$$J_2 = \frac{2|\tau_{B\pm,S}|^2}{U_S} + \frac{2|\tau_{B\pm,S}|^2}{U_B} = 31.2\,\text{meV}. \tag{6.24}$$

To analyze topological properties of longer mixed-size chains, we map the fermionic model to a spin model with one spin-1 and an even number of spin-$\frac{1}{2}$ sites per unit cell. The effective spin Hamiltonian is

$$H = H_{J_2} + H_{J_3}, \tag{6.25}$$

with

$$H_{J_2} = J_2 \sum_{m=1}^{L-1} \left[\mathbf{S}_m \cdot \mathbf{s}_{m,1} + \mathbf{s}_{m,N_s} \cdot \mathbf{S}_{m+1}\right], \tag{6.26}$$

and

$$H_{J_3} = J_3 \sum_{m=1}^{L-1} \sum_{i=1}^{N_s-1} \mathbf{s}_{m,i} \cdot \mathbf{s}_{m,i+1}. \tag{6.27}$$

Here N_S denotes the number of 13-atom TGQDs in the unit cell, $\mathbf{S}_m$ is the spin-1 operator of the m-th unit cell, and $\mathbf{s}_{m,i}$ the spin-$\frac{1}{2}$ operator of site i in unit cell m (Fig. 6.5(b)). For open chains, the system is terminated by a triangulene, so the number of spin-1 sites equals L.

In Fig. 6.5 (c), we compare the energy spectra of the fermionic and spin models for a dimer consisting of two triangulenes separated by two small TGQDs. The spectra are in good agreement, reproducing the spin ordering of the ground and excited states characteristic of a spin-1 chain.

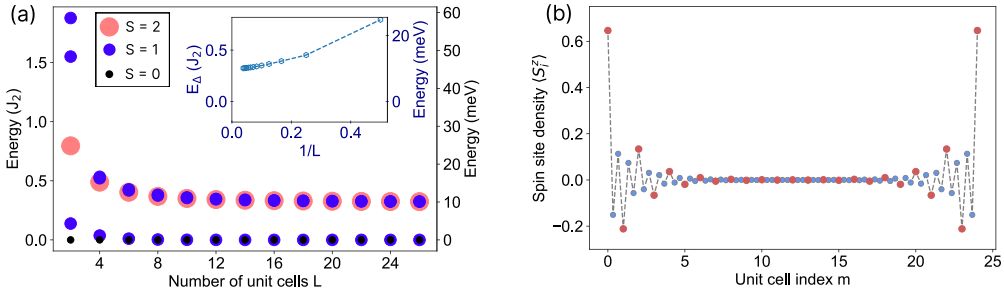

Figure 6.6: (a) Low-energy spectrum of the mixed-size nanographene chain as a function of the number of unit cells L. The inset shows the scaling of the Haldane gap with the inverse system size. (b) Local spin densities for the structure with $L = 24$. Red circles denote spin-1 sites (triangulenes), while blue circles correspond to spin-$\frac{1}{2}$ sites (phenalenyls).

6.3 Length analysis and topological properties

We now turn to the analysis of extended mixed-size nanographene chains with the unit cell indicated by a dashed line in Fig.6.5 (b). Each unit cell contains one triangulene and two phenalenyls. In order to investigate the properties of these systems in the thermodynamic limit, we employ the effective spin chain Hamiltonian derived in Eq. 6.26. Numerical calculations are carried out using the finite-size DMRG algorithm implemented in the `TeNPy` package [269]. Throughout our simulations, we set the maximum bond dimension of the MPS representation to $\chi_{\max} = 3000$, which we verified to be sufficient for converged results.

Figure 6.6 (a) shows the low-energy spectrum of chains with open boundary conditions, terminated at both ends by triangulenes. For all considered system sizes, the two lowest states are a singlet and a triplet. With increasing chain length L, these states become quasi-degenerate, and in the thermodynamic limit, they merge into the ground state manifold. Above these, the spectrum is gapped: the next excitations are separated by a finite energy gap, which extrapolates to $E_\Delta \approx 0.32 J_2$ in the large-L limit (see the inset of Fig. 6.6(a)). The resulting excitation spectrum strongly resembles that of the spin-1 Heisenberg chain with the Haldane gap, which is characteristic of a topological phase. The structure of higher excitations follows the same

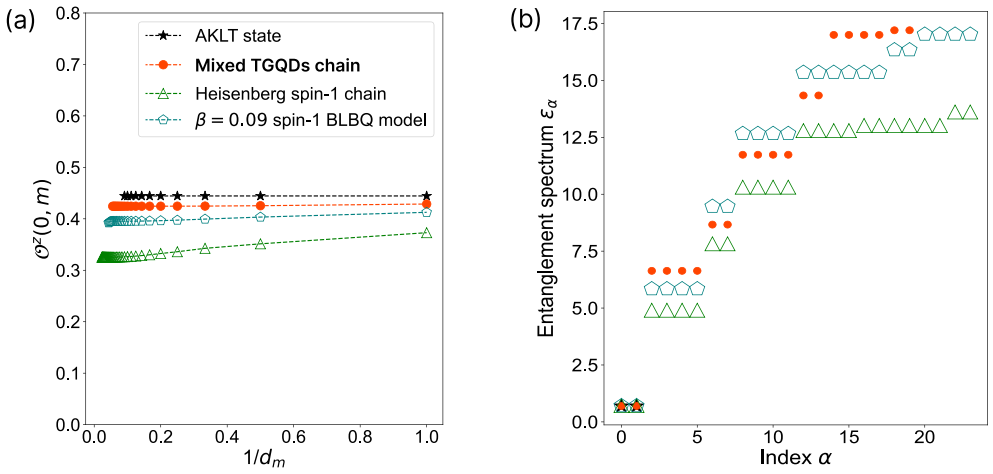

Figure 6.7: (a) String order parameter and (b) entanglement spectrum compared across four models: the mixed-size nanographene chain with length L=14, and the BLBQ Hamiltonian for $\beta = 0$ (Heisenberg model), $\beta = -0.09$ (triangulene chain), and $\beta = -\frac{1}{3}$ (AKLT state).

pattern: a quintuplet, two triplets, and a singlet above the gap.

Besides the finite gap in the thermodynamic limit, the topological Haldane phase in spin chains is characterized also by the emergence of fractionalized edge states. They are visible in spin densities shown in Fig. 6.6 (b), which are obtained for triplet state with $S = 1$. The spin density at first and last triangulene (red dots) is $\langle S_0^z \rangle = \langle S_L^z \rangle > 0.6$, similar to the value obtained for the AKLT state in Ref. [316].

To further characterize the topological order of the ground state, we next analyze the non-local string order parameter (SOP) as well as the entanglement spectrum, and compare them to other spin-1 models.

6.3.1 String order parameter

In one-dimensional quantum spin systems, conventional local order parameters often fail to distinguish between different quantum phases. The topological Haldane phase is a good example of such a state. However, it contains hidden antiferromagnetic order, which can be detected by the non-local string order parameter (SOP). For the mixed-size nanographene chain, it is defined

along the z-axis as [317]:

$$O^z = -\lim_{|m-m'|\to\infty} \langle S^z_m \exp\left(i\pi \sum_{m<n<m'} S^z_n\right) S^z_{m'} \rangle, \tag{6.28}$$

where S^z_m is the z-component of the spin-1 operator, and m, n, m' run over the unit cells of the chain.

In Fig. 6.7 (a), we compare the SOP of a mixed-size nanographene chain with the BLBQ model for four values of the β parameter. To extract the asymptotic value of the SOP, we compute it as a function of the inverse distance $1/d_m$, where d_m is the separation between the first and m-th unit cell, and then extrapolate to large distances. As expected, the AKLT state ($\beta = -\frac{1}{3}$) converges to $O^z_{\text{AKLT}} \approx 0.444$, in agreement with the exact analytical result. The Heisenberg spin-1 chain ($\beta = 0$) also exhibits a nonzero string order, but with a smaller value, $O^z_{\text{Heis}} \approx 0.32$. The third BLBQ model is the effective spin-1 Hamiltonian for the triangulene chain ($\beta = 0.09$). Its SOP parameter has a value between the AKLT state and the Heisenberg spin-1 chain, below 0.4.

Most importantly, the mixed-size TGQD chain exhibits a string order parameter of $O^z \approx 0.422$, remarkably close to the AKLT limit and larger than that of the Heisenberg model. This result indicates that the hidden antiferromagnetic order in mixed-size nanographene chains is among the strongest realized in this class of systems.

6.3.2 Entanglement spectrum

The entanglement spectrum is obtained from the Schimdt values $\{\lambda_\alpha\}$ form the Schmidt decomposition of the reduced density matrix ρ_A:

$$|\psi\rangle = \sum_i \lambda_i \, |i_A\rangle \, |i_B\rangle \,, \tag{6.29}$$

where λ_i are non-negative real numbers satisfying $\sum_i \lambda_i^2 = 1$. The entanglement spectrum "energies" ϵ_α are connected to Schimdt values by the relation $\lambda_i^2 = e^{-\epsilon_i}$.

In the Haldane phase, the entanglement spectrum displays an even-fold degeneracy [79]. This structure originates from fractionalized spin-$\frac{1}{2}$ edge states and is protected by the symmetries: time-reversal, spin rotation, and inversion. The even degeneracy is absent in a trivial phase, when protecting

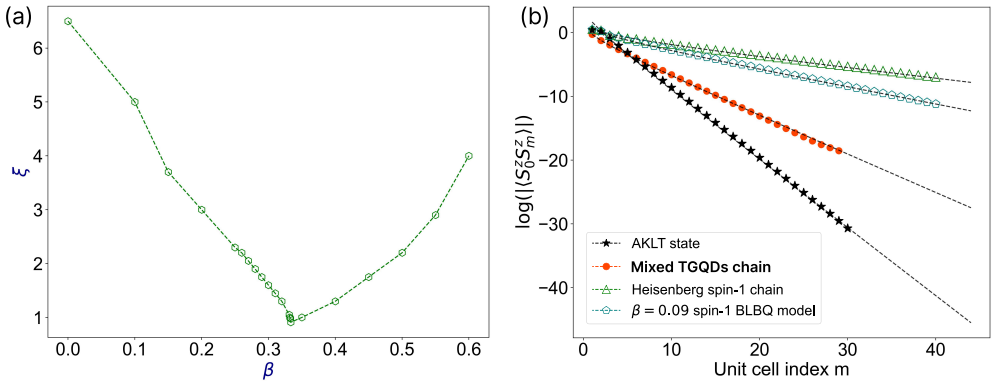

Figure 6.8: (a) Correlation length ξ of ground states in the Haldane phase as a function of the β parameter of the BLBQ Hamiltonian. (b) Spin–spin correlations between spin-1 sites in the first and m-th unit cells for mixed-size nanographene chains, compared with four BLBQ ground states. Dashed lines represent fits to the Ornstein–Zernike form.

symmetries are absent. We use this property of the entanglement spectrum as a direct indicator of symmetry-protected topological order. In Fig. 6.7 (b), we again compare the mixed-size nanographene chain with four BLBQ models. The entanglement spectra are obtained for sufficiently long chains to exclude the non-zero overlap between fractionalized spins at the edges, which can influence degeneracies. In all five cases, we observe even-fold degeneracies in the low-lying levels of the entanglement spectrum, consistent with the structure of the Haldane phase.

6.4 Correlation lengths

The results presented in the previous sections establish that the ground state of the mixed-size nanographene chain belongs to the topological Haldane phase, alongside the AKLT state and the BLBQ spin-1 models with $-1 < \beta < 1$. Within this phase, the main distinction between different ground states is their correlation lengths. In gapped one-dimensional quantum systems, spin–spin correlations are well described by the Orn-

stein–Zernike form,

$$\langle S_i^z S_j^z \rangle \sim \exp\left(-|j-i|/\xi\right)/\sqrt{|j-i|}, \tag{6.30}$$

where ξ is the correlation length. For the spin-1 Heisenberg chain, the ground state has the longest correlations within the BLBQ model and within the Haldane phase with $\xi_{Heis} \approx 6.5$. In contrast, the AKLT state realizes the shortest possible correlations within the Haldane phase, with an exactly known value of $\xi_{AKLT} = 1/\ln(3) \approx 0.91$. This trend is reproduced in Fig. 6.8(a), where the correlation length is shown as a function of the β parameter of the BLBQ Hamiltonian given by 6.6.

Figure 6.8(b) presents a direct comparison of spin–spin correlations in the mixed-size TGQD chain with those in representative BLBQ ground states. As expected, fitting the numerical data to Eq. 6.30 gives extreme values of the correlation length: $\xi_{AKLT} \approx 0.91$ and $\xi_{Heis} \approx 6.55$ for the AKLT state and Heisenberg chain, respectively. For effective triangulene chain, results for BLBQ model with $\beta = 0.09$, we obtain an intermediate value of $\xi_{\mathrm{tr}} \approx 3.9$. However, after adding smaller TGQDs, spin-$\frac{1}{2}$ radicals, between triangulenes, the correlation length is significantly reduced to $\xi \approx 1.7$. This suppression of correlations indicates that the additional spin-$\frac{1}{2}$ sites act as effective buffers, weakening the direct coupling between spin-1 TGQDs. As a result, the mixed-size nanographene chain realizes a short-correlation-length version of the Haldane phase, closer in character to the AKLT limit than to the Heisenberg chain.

6.5 Increasing the number of spin-$\frac{1}{2}$ buffers

In the previous section we showed that inserting 13-atom TGQDs between triangulene units reduces the correlation length of the nanographene chain. This suppression of correlations opens a route to designing one-dimensional topological states with well-localized edge excitations. In particular, an AKLT-like state with short correlation length is of interest for potential quantum information applications, where robust and spatially separated edge states are advantageous.

To further develop this concept, we now introduce a larger number N_S of spin-$\frac{1}{2}$ buffers per unit cell. Figure 6.9 (a) presents spin-spin correlations for chains with $N_S = 2, 4, 6, 8$, fitted using the Ornstein-Zernike formula. The correlation length systematically decreases from $\xi \approx 1.7$ for $N_S = 2$ to

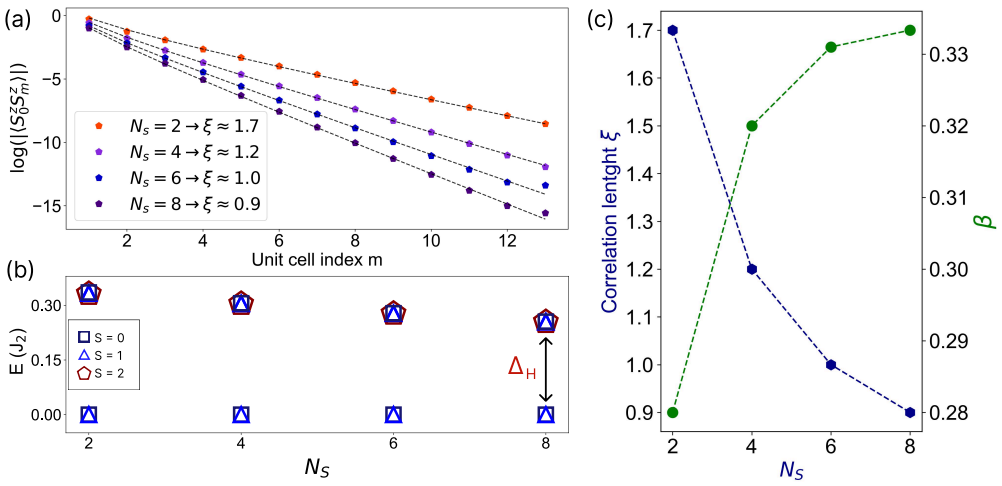

Figure 6.9: (a) Spin-spin correlations of mixed-size nanographene chains with different number of spin-$\frac{1}{2}$ buffers N_S. (b) Corresponding energy spectra showing a finite Haldane gap Δ_H. (c) Dependence of the correlation length ξ on N_S, compared to the BLBQ model parameter β.

$\xi \approx 0.9$ for $N_S = 8$, reaching the AKLT limit. At the same time, introducing the additional buffers also results in a slight decrease of the Haldane gap Δ_H, which yet remains finite for all studied cases (Fig. 6.9 (b)).

From the comparison between the correlation length obtained for the BLBQ ground state with different β parameters (Fig. 6.8 (a)) and for nanographene chains with different N_S, we can assign an effective β to N_S chains. The biquadratic term in the BLBQ Hamiltonian, obtained from higher orders of the perturbation theory, is responsible for coupling between spin-1 states that are not directly connected. They interact via intermediate configurations, the number of these virtual paths is reflected by the magnitude of the β parameter. Figure 6.9 (c) shows how $\beta(N_S)$ approches value $\frac{1}{3}$ for $\xi = 0.91$.

These results show how combining different sizes of TGQDs allows us to design topological states and manipulate their correlation length effectively tuning the β parameter of the BLBQ Hamiltonian.

Chapter 7

Conclusions

Understanding strongly correlated quantum matter remains one of the central challenges in condensed matter physics. Many of the most intriguing states, including unconventional superconductors, spin liquids, and symmetry-protected topological phases, emerge from interactions beyond the scope of perturbative approaches. In most cases, exact solutions are not available, and numerical methods face limitations due to the exponential growth of Hilbert space. Quantum simulators provide an alternative route by realizing controlled, tunable systems in which emergent many-body physics can be directly explored.

Most quantum simulation platforms are based on ultracold atoms in optical lattices, where tunneling, interactions, and dimensionality can be precisely controlled. Solid-state simulators built from electronic nanostructures offer a complementary route. They provide access to strong correlations, allow geometric control at the nanoscale, and enable the design of effective spin Hamiltonians through local electronic structure. Such systems enable studying correlated phases in regimes that are difficult to reach in other approaches.

In this thesis, we have shown that quantum-solid simulators can host a range of correlated and topological phases. In moiré TMD heterostructures, we demonstrated that strongly interacting electronic states can be localized into an array of quantum dots with controllable exchange couplings. Depending on filling, dielectric screening, and twist angle, the ground states include ferromagnetic phases stabilized by Nagaoka physics as well as antiferromagnetic states and generalized Wigner crystals. This establishes moiré quantum dot arrays as a natural extension of Hubbard physics into regimes with strong long-range interactions and finite-size effects.

We then focus on projecting the moiré Hubbard model onto the low-energy spin subspace at the half-filling. Analyzing its effective spin model shows that the system favors a quantum spin liquid for moderate dielectric screening. Such a phase is characterized by nearly uniform correlations and the absence of symmetry breaking. At stronger screening, the ground state evolves into a nematic valence bond solid, marked by alternating bond strengths and broken lattice symmetry. We further showed that ring-exchange interactions strongly influence the stability of these phases and that entanglement-based diagnostics provide consistent evidence for a continuous transition between them.

Finally, we investigated chains of mixed-size triangular graphene quantum dots. By combining spin-1 triangulenes with spin-1/2 phenalenyls, we obtained an effective one-dimensional chain with short correlation lengths. Using density matrix renormalization group calculations, we demonstrated the presence of a finite Haldane gap, localized edge states, non-local string order, and an entanglement spectrum with symmetry-protected even degeneracy. By varying the number of spin-$\frac{1}{2}$ buffer sites, we showed that the correlation length can be tuned closer to the AKLT limit. These results confirm that mixed-size nanographene chains realize the Haldane phase on minimal length scales and offer a controllable route to designing topological spin states.

The approaches presented here complement existing methods of quantum simulation. Cold atoms in optical lattices remain the most flexible platform for realizing Hubbard-type models, but they operate at weaker energy scales and require extremely low temperatures. Solid-state nanostructures provide access to strong interactions at much higher scales and are naturally suited for spin Hamiltonians and topological phases. An additional perspective is offered by quantum computing. Variational algorithms and approaches inspired by tensor networks can approximate ground states of correlated Hamiltonians and provide access to their entanglement properties. Applying these methods to models relevant for moiré heterostructures and nanographene assemblies could extend the analysis beyond classical computational limits. In this context, solid-state simulators and quantum computers can be considered complementary, with the former realizing correlated phases in experiment and the latter enabling controlled exploration of larger or more complex models. Overall, this work contributes to developing solid-state quantum simulators as a tool for studying correlated phases, which complements optical lattices and emerging quantum computing approaches.

Appendices

Appendix A

The t/U expansion of the Hubbard model

The Hubbard Hamiltonian describes electrons on a lattice with on-site repulsion:

$$\hat{H} = -t \sum_{\langle i,j\rangle,\sigma} \left(c^{\dagger}_{i\sigma} c_{j\sigma} + \text{h.c.} \right) + U \sum_{i} n_{i\uparrow} n_{i\downarrow} = T + V \tag{A.1}$$

At the half-filling and in the limit $U \gg t$, double occupancies are energetically suppressed. Weak t-hopping allows only virtual processes in which an electron visits a neighboring site, creating a doubly occupied site, but such processes cost energy U. These virtual fluctuations lift the degeneracy of singly occupied states and generate an effective spin interaction.

The Hilbert space is split into two sectors:

- P: no double occupancies,
- Q = 1 − P: states with at least one doubly occupied site.

A systematic way to derive the low-energy effective Hamiltonian of the Hubbard model in the large-U limit is to perform a Schrieffer–Wolff (SW) transformation [271, 318]. The idea is to eliminate matrix elements of the Hamiltonian that couple the low-energy subspace P with the high-energy subspace Q.

The kinetic part of the Hamiltonian T is split into three parts by how the hopping affects the number of doublons N_d, i.e. pairs of electrons on a single

site:

$$T = T_{+1} + T_0 + T_{-1}. \tag{A.2}$$

Here T_0 conserves the number of doublons, and at half-filling $\mathrm{P}T_0\mathrm{P} = 0$.

The SW transformation is unitary:

$$\hat{H}_{\text{eff}} = e^S \hat{H} e^{-S}, \tag{A.3}$$

with an anti-Hermitian generator $S = -S^\dagger$ chosen such that it cancels the off-diagonal parts connecting low- and high-energy subspaces:

$$iS = \frac{1}{U}\left(T_{+1} - T_{-1}\right). \tag{A.4}$$

The effective Hamiltonian has the form:

$$H_{\text{eff}} = e^{iS} H e^{-iS} = H + \frac{[iS, H]}{1!} + \frac{[iS, [iS, H]]}{2!} + \dots \tag{A.5}$$

By limiting the expansion to second-order perturbation theory, we obtain:

$$H_{\text{eff}} = P\left(V + T + \frac{1}{2}\left[S, T\right]\right)P + O(t^3/U^2). \tag{A.6}$$

The terms $PVP = PT_0P = 0$ vanish. Then

$$H_{\text{eff}} = \frac{1}{2} P\left[S, T_{+1} + T_{-1}\right] P \tag{A.7}$$

$$= \frac{1}{2U} P[T_{+1} - T_{-1}, T_{+1} + T_{-1}]P \tag{A.8}$$

$$= \frac{1}{U} P[T_{+1}, T_{-1}]P. \tag{A.9}$$

Now, we write explicit forms of the T operators. Hopping between i and j sites changes occupancies:

$$\Delta N_d = n_{i\sigma} - n_{j\sigma}. \tag{A.10}$$

For $\Delta N_d = +1$, the hopping operator has the form:

$$T_{+1} = -\sum_{\langle i,j\rangle,\sigma} t_{ij}\, n_{i\bar{\sigma}}\, c^\dagger_{i\sigma} c_{j\sigma}\,(1 - n_{j\bar{\sigma}}), \tag{A.11}$$

where $\bar{\sigma}$ denotes spin opposite to σ. In the case $\Delta N_d = -1$, we have:

$$T_{-1} = -\sum_{\langle i,j\rangle,\sigma} t_{ij}\,(1-n_{i\bar{\sigma}})\,c^\dagger_{i\sigma}c_{j\sigma}\,n_{j\bar{\sigma}}. \tag{A.12}$$

Lastly, for $\Delta N_d = 0$:

$$T_0 = -\sum_{\langle i,j\rangle,\sigma} t_{ij}\Big[(1-n_{i\bar{\sigma}})c^\dagger_{i\sigma}c_{j\sigma}(1-n_{j\bar{\sigma}}) + n_{i\bar{\sigma}}c^\dagger_{i\sigma}c_{j\sigma}n_{j\bar{\sigma}}\Big]. \tag{A.13}$$

We notice that

$$[V, T_m] = mUT_m, \tag{A.14}$$

which means that the interaction energy in the system changes by mU after hopping T_m.

Using definitions of T_{+1} and T_{-1}, we can then calculate the effective Hamiltonian:

$$H_{\text{eff}} = \frac{1}{U}P[T_{+1}, T_{-1}]P = \frac{1}{U}P(T_{+1}T_{-1} - T_{-1}T_{+1})P. \tag{A.15}$$

Considering a single nearest-neighbor pair $\langle i,j\rangle$, we have:

$$T^{(ij)}_{+1}T^{(ij)}_{-1} = t^2\sum_{\sigma,\sigma'}\Big[n_{i\bar{\sigma}}c^\dagger_{i\sigma}c_{j\sigma}(1-n_{j\bar{\sigma}})\Big]\Big[(1-n_{j\bar{\sigma'}})c^\dagger_{j\sigma'}c_{i\sigma'}n_{i\bar{\sigma'}}\Big]. \tag{A.16}$$

After calculating the contribution from $T_{-1}T_{+1}$ and summing them up, we obtain:

$$P(T_{+1}T_{-1} - T_{-1}T_{+1})P = -t^2\sum_{\sigma,\sigma'} P\left(c^\dagger_{i\sigma}c_{j\sigma}c^\dagger_{j\sigma'}c_{i\sigma'}\right)P. \tag{A.17}$$

So the effective Hamiltonian is:

$$H_{\text{eff}} = -\frac{t^2}{U}\sum_{\langle i,j\rangle}\sum_{\sigma,\sigma'} P\left(c^\dagger_{i\sigma}c_{j\sigma}c^\dagger_{j\sigma'}c_{i\sigma'}\right)P. \tag{A.18}$$

To convert the fermionic form $A = \sum_{\sigma,\sigma'} c^\dagger_{i\sigma}c_{j\sigma}c^\dagger_{j\sigma'}c_{i\sigma'}$ to spin ladder operators, we write it out as the sum of four possible spin combinations:

$$A = c^\dagger_{i\uparrow}c_{j\uparrow}c^\dagger_{j\uparrow}c_{i\uparrow} + c^\dagger_{i\uparrow}c_{j\uparrow}c^\dagger_{j\downarrow}c_{i\downarrow} \tag{A.19}$$

$$+ c^\dagger_{i\downarrow}c_{j\downarrow}c^\dagger_{j\uparrow}c_{i\uparrow} + c^\dagger_{i\downarrow}c_{j\downarrow}c^\dagger_{j\downarrow}c_{i\downarrow}. \tag{A.20}$$

From the fermionic relation $c_{i\sigma}c_{i\sigma}^{\dagger} = 1 - n_{i\sigma}$, we have

$$c_{i\uparrow}^{\dagger}c_{j\uparrow}c_{j\uparrow}^{\dagger}c_{i\uparrow} = n_{i\uparrow} - n_{i\uparrow}n_{j\uparrow}, \tag{A.21}$$

$$c_{i\downarrow}^{\dagger}c_{j\downarrow}c_{j\downarrow}^{\dagger}c_{i\downarrow} = n_{i\downarrow} - n_{i\downarrow}n_{j\downarrow}. \tag{A.22}$$

Terms with $\sigma \neq \sigma'$ map directly to spin ladder operators $S_i^{+} = c_{i\uparrow}^{\dagger}c_{i\downarrow}$ and $S_i^{-} = c_{i\downarrow}^{\dagger}c_{i\uparrow}$. Thus

$$c_{i\uparrow}^{\dagger}c_{j\uparrow}c_{j\downarrow}^{\dagger}c_{i\downarrow} = -S_i^{+}S_j^{-}, \tag{A.23}$$

$$c_{i\downarrow}^{\dagger}c_{j\downarrow}c_{j\uparrow}^{\dagger}c_{i\uparrow} = -S_i^{-}S_j^{+}. \tag{A.24}$$

After summing the above results, the operator A takes the form:

$$A = n_i - \frac{1}{2}n_i n_j - \Big(2S_i^z S_j^z + S_i^{+}S_j^{-} + S_i^{-}S_j^{+}\Big). \tag{A.25}$$

By definition $\mathbf{S}_i \cdot \mathbf{S}_j = S_i^z S_j^z + \frac{1}{2}(S_i^{+}S_j^{-} + S_i^{-}S_j^{+})$, thus

$$A = n_i - \frac{1}{2}n_i n_j - 2\mathbf{S}_i \cdot \mathbf{S}_j. \tag{A.26}$$

By projecting the A operator onto the subspace with one electron per site, we obtain the effective Hamiltonian:

$$H_{\text{eff}} = -\frac{t^2}{U}\sum_{\langle i,j\rangle}\left(-2\mathbf{S}_i \cdot \mathbf{S}_j + \tfrac{1}{2}n_i n_j\right) = \frac{4t^2}{U}\sum_{\langle i,j\rangle}\left(\mathbf{S}_i \cdot \mathbf{S}_j - \tfrac{1}{4}n_i n_j\right). \tag{A.27}$$

The ring exchange interaction term can be obtained in an analogous way from the fourth-order contribution to the effective Hamiltonian in the low-energy subspace:

$$\hat{H}_{\text{eff}}^{(4)} = -\,P\,\hat{T}\,\hat{Q}\frac{1}{\hat{H}_0}\hat{Q}\,\hat{T}\,\hat{Q}\frac{1}{\hat{H}_0}\hat{Q}\,\hat{T}\,\hat{Q}\frac{1}{\hat{H}_0}\hat{Q}\,\hat{T}\,P, \tag{A.28}$$

where $\hat{T}$ is the hopping part of the Hubbard model, $\hat{H}_0 = U\sum_i n_{i\uparrow}n_{i\downarrow}$, and $Q = 1 - P$. Each resolvent $1/\hat{H}_0$ contributes an energy denominator of order $1/U$, so the overall scale of $\hat{H}_{\text{eff}}^{(4)}$ is $\mathcal{O}(t^4/U^3)$.

Focus on an oriented four-site loop $i \to j \to k \to l \to i$. One sequence of four hoppings produces the fermionic cyclic operator:

$$\mathcal{O}^{(ijkl)} = \sum_{\{\sigma\}}\left(c_{j\sigma_1}^{\dagger}c_{i\sigma_1}\right)\left(c_{k\sigma_2}^{\dagger}c_{j\sigma_2}\right)\left(c_{l\sigma_3}^{\dagger}c_{k\sigma_3}\right)\left(c_{i\sigma_4}^{\dagger}c_{l\sigma_4}\right), \tag{A.29}$$

which cyclically moves an electron around the plaquette. The full fourth-order projector (A.28) sums such operators over all such ordered sequences and over spin indices. Collecting all contributions for the plaquette yields the compact permutation form

$$\hat{H}_{\text{ring}}^{(ijk\ell)} \;=\; K\left(\hat{P}_{i\to j\to k\to \ell} + \hat{P}_{i\leftarrow j\leftarrow k\leftarrow \ell}\right) \tag{A.30}$$

To connect this to spin operators, it is convenient to use the two-site permutation operator. The following operator identity holds:

$$\hat{P}_{ab} = \sum_{\sigma,\sigma'} c_{a\sigma}^{\dagger} c_{b\sigma'}^{\dagger} c_{a\sigma'} c_{b\sigma} = 2\,\mathbf{S}_a\cdot\mathbf{S}_b + \tfrac{1}{2} n_a n_b. \tag{A.31}$$

In particular, on the singly-occupied subspace P (where $n_a n_b = 1$) this reduces to the familiar form $\hat{P}_{ab} = 2\mathbf{S}_a \cdot \mathbf{S}_b + \frac{1}{2}$.

Using $\hat{P}_{1234} = \hat{P}_{14}\hat{P}_{13}\hat{P}_{12}$ (and the analogous expression for the opposite orientation) and expanding the products, the permutation sum can be written as a sum of a constant, pairwise Heisenberg terms, and four-spin terms. One convenient projected form is

$$\hat{P}_{1234}+\hat{P}_{1432} = \tfrac{1}{4}+\sum_{\langle ab\rangle} \mathbf{S}_a\mathbf{S}_b+4\Big[(\mathbf{S}_1\mathbf{S}_2)(\mathbf{S}_3\mathbf{S}_4)+(\mathbf{S}_2\mathbf{S}_3)(\mathbf{S}_4\mathbf{S}_1)-(\mathbf{S}_1\mathbf{S}_3)(\mathbf{S}_2\mathbf{S}_4)\Big], \tag{A.32}$$

where the sum $\sum_{\langle ab\rangle}$ runs over nearest-neighbour pairs around the plaquette $(1,2,3,4)$. Combining this expansion with the amplitude K gives the fourth-order contribution to the effective spin Hamiltonian on the plaquette,

$$\hat{H}_{\text{ring}}^{(1234)} = K\Big[\tfrac{1}{4} + \sum_{\langle ab\rangle} \mathbf{S}_a\cdot\mathbf{S}_b + 4\big((\mathbf{S}_1\cdot\mathbf{S}_2)(\mathbf{S}_3\cdot\mathbf{S}_4)\big)\Big]. \tag{A.33}$$

Appendix B

Configuration Interaction

In the Hartree–Fock (HF) approximation, the many-body wavefunction is represented by a single Slater determinant,

$$|\Psi_{\mathrm{HF}}\rangle = \frac{1}{\sqrt{N!}} \det[\phi_1(1), \phi_2(2), \ldots, \phi_N(N)], \tag{B.1}$$

where ϕ_i are spin–orbitals. While this approximation accounts for exchange interactions exactly, it neglects electron–electron correlations beyond mean field.

The configuration interaction (CI) [319,320] method improves upon Hartree–Fock by constructing the wavefunction as a linear combination of Slater determinants: the reference Hartree–Fock determinant plus determinants obtained by exciting one or more electrons from occupied orbitals into virtual (unoccupied) orbitals. The CI wavefunction takes the form

$$|\Psi_{\mathrm{CI}}\rangle = c_0 \, |\Phi_0\rangle + \sum_{i,a} c_i^a \, |\Phi_i^a\rangle + \sum_{i<j,a<b} c_{ij}^{ab} \, |\Phi_{ij}^{ab}\rangle + \ldots, \tag{B.2}$$

where $|\Phi_0\rangle$ is the HF determinant, $|\Phi_i^a\rangle$ denotes a single excitation from occupied orbital i to virtual orbital a, and $|\Phi_{ij}^{ab}\rangle$ is a double excitation, etc. The expansion coefficients $c_0, c_i^a, c_{ij}^{ab}, \ldots$ are obtained by diagonalizing the electronic Hamiltonian in the CI basis.

To illustrate the procedure step by step, consider a minimal example with two electrons distributed among four spin–orbitals: two occupied (i, j) and two virtual (a, b). At the HF level, both electrons occupy the lowest-energy orbitals i and j, giving

$$|\Phi_0\rangle = |ij|, \tag{B.3}$$

where the notation $|pq|$ denotes the Slater determinant with electrons in orbitals p and q.

With respect to this state, single excitations are created by promoting one electron from an occupied to a virtual orbital:

$$|\Phi_i^a\rangle = |aj|, \qquad |\Phi_i^b\rangle = |bj|, \tag{B.4}$$

$$|\Phi_j^a\rangle = |ia|, \qquad |\Phi_j^b\rangle = |ib|. \tag{B.5}$$

Each determinant differs from $|\Phi_0\rangle$ by one orbital substitution. Double excitations involve substituting both occupied orbitals simultaneously:

$$|\Phi_{ij}^{ab}\rangle = |ab|. \tag{B.6}$$

Together, the reference, singles, and doubles span the so-called CISD basis:

$$\mathcal{B}_{\text{CISD}} = \{|ij|, |aj|, |bj|, |ia|, |ib|, |ab|\}. \tag{B.7}$$

The correlated CI wavefunction is then expanded as

$$|\Psi_{\text{CISD}}\rangle = c_0|ij| + c_i^a|aj| + c_i^b|bj| + c_j^a|ia| + c_j^b|ib| + c_{ij}^{ab}|ab|, \tag{B.8}$$

with coefficients $\{c\}$ determined by diagonalization of the Hamiltonian in the basis $\mathcal{B}_{\text{CISD}}$.

The accuracy of CI systematically improves with the inclusion of higher excitation levels, but the computational cost grows factorially, making full CI feasible only for very small systems. Moreover, truncated CI may fail when multiple electronic configurations contribute nearly equally to the ground state. In such cases, one must restrict the CI expansion in a way that properly accounts for strong static correlations.

A widely used approach is the complete active space (CAS) method [321], which treats strongly correlated orbitals exactly while freezing less important ones. The orbitals are divided into three groups:

1. Inactive orbitals – always doubly occupied,
2. Active orbitals – partially filled with all possible occupations included,
3. Virtual orbitals – always unoccupied.

This partition reflects the physical intuition that static correlation arises mainly in a limited set of orbitals near the Fermi level, while core and high-energy virtual orbitals can be frozen.

In a CAS(n, m) calculation, n active electrons are distributed among m active orbitals. The CAS wavefunction is then a linear combination of all determinants generated within this active space:

$$|\Psi_{\mathrm{CAS}(n,m)}\rangle = \sum_{I \in \mathcal{B}_{\mathrm{CAS}(n,m)}} c_I \, |\Phi_I\rangle \,, \tag{B.9}$$

where $\mathcal{B}_{\mathrm{CAS}(n,m)}$ is the full configuration space within the active orbitals. This guarantees an exact treatment of static correlations in the chosen active subspace.

Bibliography

[1] Kevin P. Nuckolls, Ryan L. Lee, Myungchul Oh, Dillon Wong, Tomohiro Soejima, Jung Pyo Hong, Dumitru Călugăru, Jonah Herzog-Arbeitman, B. Andrei Bernevig, Kenji Watanabe, Takashi Taniguchi, Nicolas Regnault, Michael P. Zaletel, and Ali Yazdani. Quantum textures of the many-body wavefunctions in magic-angle graphene. *arXiv (Cornell University)*, 2 2023.

[2] Weronika Pasek, Michal Kupczynski, and Pawel Potasz. Magnetic properties of moiré quantum dot arrays. *Physical review. B./Physical review. B*, 108(16), 10 2023.

[3] Yasser Saleem, Torben Steenbock, Emha Riyadhul Jinan Alhadi, Weronika Pasek, Gabriel Bester, and Pawel Potasz. Superexchange mechanism in coupled triangulenes forming spin-1 chains. *Nano Letters*, 24(24):7417–7423, 6 2024.

[4] E. Wigner. On the Interaction of Electrons in Metals. *Physical Review*, 46(11):1002–1011, 12 1934.

[5] Robert W Shaw, Jr. Effective masses and perturbation theory in the theory of simple metals. *Journal of Physics C Solid State Physics*, 2(12):2350–2365, 12 1969.

[6] Peter Fulde, Peter Thalmeier, and Gertrud Zwicknagl. *Strongly correlated electrons*. 1 2006.

[7] Emilia Morosan, Douglas Natelson, Andriy H. Nevidomskyy, and Qimiao Si. Strongly correlated materials. *Advanced Materials*, 24(36):4896–4923, 8 2012.

[8] Silke Paschen and Qimiao Si. Quantum phases driven by strong correlations. *Nature Reviews Physics*, 3(1):9–26, 12 2020.

[9] J H De Boer and E J W Verwey. Semi-conductors with partially and with completely filled3d-lattice bands. *Proceedings of the Physical Society*, 49(4S):59–71, 8 1937.

[10] N F Mott and R Peierls. Discussion of the paper by de Boer and Verwey. *Proceedings of the Physical Society*, 49(4S):72–73, 8 1937.

[11] N F Mott. The Basis of the Electron Theory of Metals, with Special Reference to the Transition Metals. *Proceedings of the Physical Society Section A*, 62(7):416–422, 7 1949.

[12] J. Hubbard. Electron correlations in narrow energy bands. *Proceedings of the Royal Society of London A Mathematical and Physical Sciences*, 276(1365):238–257, 11 1963.

[13] P. W. Anderson. Localized magnetic states in metals. *Physical Review*, 124(1):41–53, 10 1961.

[14] A. C. Hewson. Theory of localized magnetic states in metals. *Physical Review*, 144(2):420–427, 4 1966.

[15] Patrick A. Lee and Daniel S. Fisher. Anderson Localization in two dimensions. *Physical Review Letters*, 47(12):882–885, 9 1981.

[16] Y. M. Vilk, Liang Chen, and A.-m. S. Tremblay. Theory of spin and charge fluctuations in the Hubbard model. *Physical review. B, Condensed matter*, 49(18):13267–13270, 5 1994.

[17] J. Kondo. Resistance minimum in dilute magnetic alloys. *Progress of Theoretical Physics*, 32(1):37–49, 7 1964.

[18] Alexander Cyril Hewson. *The kondo problem to heavy fermions*. 1 1993.

[19] F. Steglich, J. Aarts, C. D. Bredl, W. Lieke, D. Meschede, W. Franz, and H. Sch"afer. Superconductivity in the presence of strong pauli paramagnetism: Cecu2si2. *Physical Review Letters*, 43(25):1892–1896, 12 1979.

[20] H. R. Ott, H. Rudigier, Z. Fisk, and J. L. Smith. UBE13: an unconventional actinide superconductor. *Physical Review Letters*, 50(20):1595–1598, 5 1983.

[21] Patrick A. Lee, Naoto Nagaosa, and Xiao-Gang Wen. Doping a Mott insulator: Physics of high-temperature superconductivity. *Reviews of Modern Physics*, 78(1):17–85, 1 2006.

[22] J.E. Hirsch, M.B. Maple, and F. Marsiglio. Superconducting materials classes: Introduction and overview. *Physica C Superconductivity*, 514:1–8, 5 2015.

[23] Alexei Kitaev. Anyons in an exactly solved model and beyond. *Annals of Physics*, 321(1):2–111, 1 2006.

[24] Leon Balents. Spin liquids in frustrated magnets. *Nature*, 464(7286):199–208, 3 2010.

[25] Vasily R. Shaginyan, Alfred Z. Msezane, George S. Japaridze, Stanislav A. Artamonov, and Yulya S. Leevik. Strongly Correlated Quantum Spin Liquids versus Heavy Fermion Metals: A Review. *Materials*, 15(11):3901, 5 2022.

[26] R. B. Laughlin. Anomalous Quantum Hall Effect: An Incompressible Quantum Fluid with Fractionally Charged Excitations. *Physical Review Letters*, 50(18):1395–1398, 5 1983.

[27] F.D.M. Haldane. Continuum dynamics of the 1-D Heisenberg antiferromagnet: Identification with the O(3) nonlinear sigma model. *Physics Letters A*, 93(9):464–468, 2 1983.

[28] Immanuel Bloch, Jean Dalibard, and Wilhelm Zwerger. Many-body physics with ultracold gases. *Reviews of Modern Physics*, 80(3):885–964, 7 2008.

[29] Eva Y. Andrei, Dmitri K. Efetov, Pablo Jarillo-Herrero, Allan H. MacDonald, Kin Fai Mak, T. Senthil, Emanuel Tutuc, Ali Yazdani, and Andrea F. Young. The marvels of moiré materials. *Nature Reviews Materials*, 6(3):201–206, 3 2021.

[30] N F Mott. The Basis of the Electron Theory of Metals, with Special Reference to the Transition Metals. *Proceedings of the Physical Society Section A*, 62(7):416–422, 7 1949.

[31] B.H. Brandow. Electronic structure of Mott insulators. *Advances In Physics*, 26(5):651–808, 9 1977.

[32] Yuki Nakata, Katsuaki Sugawara, Ryota Shimizu, Yoshinori Okada, Patrick Han, Taro Hitosugi, Keiji Ueno, Takafumi Sato, and Takashi Takahashi. Monolayer 1T-NbSe2 as a Mott insulator. *NPG Asia Materials*, 8(11):e321, 11 2016.

[33] Y. D. Wang, W. L. Yao, Z. M. Xin, T. T. Han, Z. G. Wang, L. Chen, C. Cai, Yuan Li, and Y. Zhang. Band insulator to Mott insulator transition in 1T-TaS2. *Nature Communications*, 11(1), 8 2020.

[34] Ying Fei, Zongxiu Wu, Wenhao Zhang, and Yi Yin. Understanding the Mott insulating state in 1T-TaS2 and 1T-TaSe2. *AAPPS bulletin*, 32(1), 7 2022.

[35] Hoi Chun Po, Liujun Zou, Ashvin Vishwanath, and T. Senthil. Origin of Mott insulating behavior and superconductivity in twisted bilayer graphene. *Physical Review X*, 8(3), 9 2018.

[36] Bin-Bin Chen, Yuan Da Liao, Ziyu Chen, Oskar Vafek, Jian Kang, Wei Li, and Zi Yang Meng. Realization of topological Mott insulator in a twisted bilayer graphene lattice model. *Nature Communications*, 12(1), 9 2021.

[37] S. Lefebvre, P. Wzietek, S. Brown, C. Bourbonnais, D. Jérome, C. Mézière, M. Fourmigué, and P. Batail. Mott transition, antiferromagnetism, and unconventional superconductivity in layered organic superconductors. *Physical Review Letters*, 85(25):5420–5423, 12 2000.

[38] *ON THE THEORY OF PHASE TRANSITIONS.* 1 1965.

[39] Roderich Moessner and Joel E. Moore. *Topological phases of matter.* 4 2021.

[40] Xiao-Gang Wen. Colloquium : Zoo of quantum-topological phases of matter. *Reviews of Modern Physics*, 89(4), 12 2017.

[41] S M Girvin and Daniel P Arovas. Hidden topological order in integer quantum spin chains. *Physica Scripta*, T27:156–159, 1 1989.

[42] S. Raghu, Xiao-Liang Qi, C. Honerkamp, and Shou-Cheng Zhang. Topological mott insulators. *Physical Review Letters*, 100(15), 4 2008.

[43] T. Senthil. Symmetry-Protected topological phases of quantum matter. *Annual Review of Condensed Matter Physics*, 6(1):299–324, 1 2015.

[44] Charles Zhaoxi Xiong. Classification and construction of topological phases of quantum matter. *arXiv (Cornell University)*, 1 2019.

[45] Alexei Kitaev, Vladimir Lebedev, and Mikhail Feigel'man. Periodic table for topological insulators and superconductors. *AIP conference proceedings*, 1 2009.

[46] Xie Chen, Zheng-Cheng Gu, Zheng-Xin Liu, and Xiao-Gang Wen. Symmetry protected topological orders and the group cohomology of their symmetry group. *Physical Review B*, 87(15), 4 2013.

[47] Xie Chen, Zheng-Cheng Gu, and Xiao-Gang Wen. Complete classification of one-dimensional gapped quantum phases in interacting spin systems. *Physical Review B*, 84(23), 12 2011.

[48] Xiao-Gang Wen. Topological order: from Long-Range entangled quantum matter to a unified origin of light and electrons. *ISRN Condensed Matter Physics*, 2013:1–20, 3 2013.

[49] X. G. Wen. Vacuum degeneracy of chiral spin states in compactified space. *Physical review. B, Condensed matter*, 40(10):7387–7390, 10 1989.

[50] Meng Cheng, Seth Musser, Amir Raz, Nathan Seiberg, and T. Senthil. Ordering the topological order in the fractional quantum Hall effect, 5 2025.

[51] R. Nesbet. The Heisenberg exchange operator for ferromagnetic and antiferromagnetic systems, 1958.

[52] L.P. Levy. *Magnetism and Superconductivity*. Texts and monographs in physics. Springer, 2000.

[53] Thierry Giamarchi. *Quantum Physics in one dimension*. 12 2003.

[54] W. Heisenberg. Zur Theorie des Ferromagnetismus. *The European Physical Journal A*, 49(9-10):619–636, 9 1928.

[55] Antonio Sergio Teixeira Pires. *The Heisenberg model*. 4 2021.

[56] H. Bethe. Zur Theorie der Metalle. *The European Physical Journal A*, 71(3-4):205–226, 3 1931.

[57] Minoru Takahashi. *Thermodynamics of One-Dimensional solvable models*. 3 1999.

[58] I Affleck. Quantum spin chains and the Haldane gap. *Journal of Physics Condensed Matter*, 1(19):3047–3072, 5 1989.

[59] Hans-Jürgen Mikeska and Alexei K. Kolezhuk. *One-dimensional magnetism*. 1 2004.

[60] R. Vlijm and J.-s. Caux. Spinon dynamics in quantum integrable antiferromagnets. *Physical review. B./Physical review. B*, 93(17), 5 2016.

[61] L.D. Faddeev and L.A. Takhtajan. What is the spin of a spin wave? *Physics Letters A*, 85(6-7):375–377, 10 1981.

[62] Teresa Kulka, Miłosz Panfil, Mona Berciu, and Krzysztof Wohlfeld. Nature of spinons in 1D spin chains. *Physical Review Letters*, 134(23), 5 2025.

[63] Martin Mourigal, Mechthild Enderle, Axel Klöpperpieper, Jean-Sébastien Caux, Anne Stunault, and Henrik M. Rønnow. Fractional spinon excitations in the quantum Heisenberg antiferromagnetic chain. *Nature Physics*, 9(7):435–441, 6 2013.

[64] Xuelei Su, Zhihao Ding, Ye Hong, Nan Ke, KaKing Yan, Can Li, Yi-Fan Jiang, and Ping Yu. Fabrication of spin-1/2 Heisenberg antiferromagnetic chains via combined on-surface synthesis and reduction for spinon detection. *Nature Synthesis*, 2 2025.

[65] Zhangyu Yuan, Xin-Yu Zhang, Yashi Jiang, Xiangjian Qian, Ying Wang, Yufeng Liu, Liang Liu, Xiaoxue Liu, Dandan Guan, Yaoyi Li, Hao Zheng, Canhua Liu, Jinfeng Jia, Mingpu Qin, Pei-Nian Liu, Deng-Yuan Li, and Shiyong Wang. Fractional spinon quasiparticles in open-shell triangulene spin-1/2 chains. *Journal of the American Chemical Society*, 147(6):5004–5013, 2025. PMID: 39874540.

[66] David Emin. *Polarons*. Cambridge University Press, 1 2013.

[67] Cesare Franchini, Michele Reticcioli, Martin Setvin, and Ulrike Diebold. Polarons in materials. *Nature Reviews Materials*, 6(7):560–586, 3 2021.

[68] F. M. Peeters and M. A. Smondyrev. Exact and approximate results for the polaron in one dimension. *Physical review. B, Condensed matter*, 43(6):4920–4924, 2 1991.

[69] Chen Qinghu, Wang Kelin, and Wan Shaolong. An extensive calculation of the properties of a one-dimensional polaron. *Journal of Physics Condensed Matter*, 6(33):6599–6609, 8 1994.

[70] A. G. Volosniev and H.-w. Hammer. Analytical approach to the Bose-polaron problem in one dimension. *Physical review. A*, 96(3), 9 2017.

[71] Piotr Wrzosek, Adam Kłosiński, Yao Wang, Mona Berciu, Cliò Efthimia Agrapidis, and Krzysztof Wohlfeld. The fate of the spin polaron in the 1D antiferromagnets. *SciPost Physics*, 17(1), 7 2024.

[72] M. G. Zacher, E. Arrigoni, W. Hanke, and J. R. Schrieffer. Systematic numerical study of spin-charge separation in one dimension. *Physical review. B, Condensed matter*, 57(11):6370–6375, 3 1998.

[73] O. M. Auslaender, H. Steinberg, A. Yacoby, Y. Tserkovnyak, B. I. Halperin, K. W. Baldwin, L. N. Pfeiffer, and K. W. West. Spin-Charge separation and localization in one dimension. *Science*, 308(5718):88–92, 3 2005.

[74] F. D. M. Haldane. Nonlinear Field Theory of Large-Spin Heisenberg Antiferromagnets: semiclassically quantized solitons of the One-Dimensional Easy-Axis Néel State. *Physical Review Letters*, 50(15):1153–1156, 4 1983.

[75] Román Orús, Tzu-Chieh Wei, and Hong-Hao Tu. Phase diagram of the SO(n) bilinear-biquadratic chain from many-body entanglement. *Physical Review B*, 84(6), 8 2011.

[76] Mykhailo V. Rakov and Michael Weyrauch. Bilinear-biquadratic spin-1 model in the Haldane and dimerized phases. *Physical review. B./Physical review. B*, 105(2), 1 2022.

[77] Hal Tasaki. Ground state of the S=1 antiferromagnetic Heisenberg chain is topologically nontrivial if gapped. *Physical Review Letters*, 134(7), 2 2025.

[78] Zheng-Cheng Gu and Xiao-Gang Wen. Tensor-entanglement-filtering renormalization approach and symmetry-protected topological order. *Phys. Rev. B*, 80:155131, Oct 2009.

[79] Frank Pollmann, Ari M. Turner, Erez Berg, and Masaki Oshikawa. Entanglement spectrum of a topological phase in one dimension. *Phys. Rev. B*, 81:064439, Feb 2010.

[80] Ian Affleck, Tom Kennedy, Elliott H. Lieb, and Hal Tasaki. Rigorous results on valence-bond ground states in antiferromagnets. *Phys. Rev. Lett.*, 59:799–802, Aug 1987.

[81] Ian Affleck, Tom Kennedy, Elliott H. Lieb, and Hal Tasaki. Valence bond ground states in isotropic quantum antiferromagnets. *Communications in Mathematical Physics*, 115(3):477–528, 9 1988.

[82] M. P. Sarachik, E. Corenzwit, and L. D. Longinotti. Resistivity of MO-NB and MO-RE alloys containing 1 *Physical Review*, 135(4A):A1041–A1045, 8 1964.

[83] E. Grüneisen. Die Abhängigkeit des elektrischen Widerstandes reiner Metalle von der Temperatur. *Annalen der Physik*, 408(5):530–540, 1 1933.

[84] Leo Kouwenhoven and Leonid Glazman. Revival of the Kondo effect. *Physics World*, 14(1):33–38, 1 2001.

[85] B. Coqblin, M. D. Núñez-Regueiro, A. Theumann, J. R. Iglesias, and S. G Magalhães. Theory of the Kondo lattice: competition between Kondo effect and magnetic order. *The Philosophical Magazine A Journal of Theoretical Experimental and Applied Physics*, 86(17-18):2567–2580, 5 2006.

[86] Alex Hewson and Jun Kondo. Kondo effect. *Scholarpedia*, 4(3):7529, 1 2009.

[87] Alexander Cyril Hewson. *The kondo problem to heavy fermions*. 1 1993.

[88] Piers Coleman. Heavy Fermions and the Kondo Lattice: a 21st Century Perspective, 9 2015.

[89] Bruno Uchoa, T. G. Rappoport, and A. H. Castro Neto. Kondo Quantum criticality of magnetic adatoms in graphene. *Physical Review Letters*, 106(1), 1 2011.

[90] Z. Iftikhar, A. Anthore, A. K. Mitchell, F. D. Parmentier, U. Gennser, A. Ouerghi, A. Cavanna, C. Mora, P. Simon, and F. Pierre. Tunable quantum criticality and super-ballistic transport in a "charge" Kondo circuit. *Science*, 360(6395):1315–1320, 5 2018.

[91] Wesley T. Fuhrman, Andrey Sidorenko, Jonathan Hänel, Hannes Winkler, Andrey Prokofiev, Jose A. Rodriguez-Rivera, Yiming Qiu, Peter Blaha, Qimiao Si, Collin L. Broholm, and Silke Paschen. Pristine quantum criticality in a Kondo semimetal. *Science Advances*, 7(21), 5 2021.

[92] E Miranda, V Dobrosavljevic, and G Kotliar. Kondo disorder: a possible route towards non-Fermi-liquid behaviour. *Journal of Physics Condensed Matter*, 8(48):9871–9900, 11 1996.

[93] Ian Affleck. Non-Fermi liquid behavior in kondo models. *Journal of the Physical Society of Japan*, 74(1):59–66, 1 2005.

[94] S. Burdin, D. R. Grempel, and A. Georges. Heavy-fermion and spin-liquid behavior in a Kondo lattice with magnetic frustration. *Physical review. B, Condensed matter*, 66(4), 7 2002.

[95] Guang-Ming Zhang, Qiang Gu, and Lu Yu. Kondo spin liquid and magnetically long-range ordered states in the Kondo necklace model. *Physical review. B, Condensed matter*, 62(1):69–72, 7 2000.

[96] Lars Fritz and Matthias Vojta. The physics of Kondo impurities in graphene. *Reports on Progress in Physics*, 76(3):032501, 2 2013.

[97] Pedro L. S. Lopes, I. Affleck, and E. Sela. Anyons in multichannel Kondo systems. *Physical review. B./Physical review. B*, 101(8), 2 2020.

[98] Zhao Liu, Emil J. Bergholtz, Heng Fan, and Andreas M. Läuchli. Fractional Chern Insulators in Topological Flat Bands with Higher Chern Number. *Physical Review Letters*, 109(18), 11 2012.

[99] S. A. Parameswaran, R. Roy, and S. L. Sondhi. Fractional Chern insulators and the W_∞ algebra. *Physical Review B*, 85(24), 6 2012.

[100] Titus Neupert, Claudio Chamon, Thomas Iadecola, Luiz H Santos, and Christopher Mudry. Fractional (Chern and topological) insulators. *Physica Scripta*, T164:014005, 8 2015.

[101] Nobuyuki Okuma and Tomonari Mizoguchi. Topological two-body interaction obstructing trivial ground states: an indicator of fractional Chern insulators, 6 2025.

[102] D. C. Tsui, H. L. Stormer, and A. C. Gossard. Two-Dimensional magnetotransport in the extreme quantum limit. *Physical Review Letters*, 48(22):1559–1562, 5 1982.

[103] R. B. Laughlin. Anomalous Quantum Hall Effect: An Incompressible Quantum Fluid with Fractionally Charged Excitations. *Physical Review Letters*, 50(18):1395–1398, 5 1983.

[104] J. K. Jain. Theory of the fractional quantum Hall effect. *Physical review. B, Condensed matter*, 41(11):7653–7665, 4 1990.

[105] D.N. Sheng, Zheng-Cheng Gu, Kai Sun, and L. Sheng. Fractional quantum Hall effect in the absence of Landau levels. *Nature Communications*, 2(1), 7 2011.

[106] Fengcheng Wu, Timothy Lovorn, Emanuel Tutuc, Ivar Martin, and A. H. MacDonald. Topological insulators in twisted transition metal dichalcogenide homobilayers. *Physical Review Letters*, 122(8), 2 2019.

[107] Heqiu Li, Umesh Kumar, Kai Sun, and Shi-Zeng Lin. Spontaneous fractional Chern insulators in transition metal dichalcogenide moiré superlattices. *Physical Review Research*, 3(3), 9 2021.

[108] Kin Fai Mak, Yihang Zeng, Zhengchao Xia, Kaifei Kang, Jiacheng Zhu, Patrick Knuppel, Chirag Vaswani, Kenji Watanabe, Takashi Taniguchi, and Jie Shan. Integer and fractional Chern insulators in twisted bilayer MoTe2. *Research Square (Research Square)*, 5 2023.

[109] Chong Wang, Xiao-Wei Zhang, Xiaoyu Liu, Yuchi He, Xiaodong Xu, Ying Ran, Ting Cao, and Di Xiao. Fractional Chern Insulator in twisted bilayer MOTE2. *Physical Review Letters*, 132(3), 1 2024.

[110] Shota Kanasugi and Youichi Yanase. Multiple odd-parity superconducting phases in bilayer transition metal dichalcogenides. *Physical review. B./Physical review. B*, 102(9), 9 2020.

[111] Ammon Fischer, Zachary A. H. Goodwin, Arash A. Mostofi, Johannes Lischner, Dante M. Kennes, and Lennart Klebl. Unconventional superconductivity in magic-angle twisted trilayer graphene. *npj Quantum Materials*, 7(1), 1 2022.

[112] Jiaqi Cai, Eric Anderson, Chong Wang, Xiaowei Zhang, Xiaoyu Liu, William Holtzmann, Yinong Zhang, Fengren Fan, Takashi Taniguchi, Kenji Watanabe, Ying Ran, Ting Cao, Liang Fu, Di Xiao, Wang Yao, and Xiaodong Xu. Signatures of fractional quantum anomalous Hall states in twisted MoTe2. *Nature*, 622(7981):63–68, 6 2023.

[113] Johannes Motruk, Dario Rossi, Dmitry A. Abanin, and Louk Rademaker. Kagome chiral spin liquid in transition metal dichalcogenide moiré bilayers. *Physical Review Research*, 5(2), 6 2023.

[114] Yixuan Huang, D. N. Sheng, and Jian-Xin Zhu. Magnetic field induced partially polarized chiral spin liquid in a transition metal dichalcogenide moiré system. *Physical review. B./Physical review. B*, 109(16), 4 2024.

[115] Päivi Törmä. Essay: Where can Quantum geometry lead us? *Physical Review Letters*, 131(24), 12 2023.

[116] Alexander Kruchkov. Quantum geometry, flat Chern bands, and Wannier orbital quantization. *Physical review. B./Physical review. B*, 105(24), 6 2022.

[117] Bruno Mera and Johannes Mitscherling. Nontrivial quantum geometry of degenerate flat bands. *Physical review. B./Physical review. B*, 106(16), 10 2022.

[118] Haidong Tian, Xueshi Gao, Yuxin Zhang, Shi Che, Tianyi Xu, Patrick Cheung, Kenji Watanabe, Takashi Taniguchi, Mohit Randeria, Fan Zhang, Chun Ning Lau, and Marc W. Bockrath. Evidence for Dirac flat band superconductivity enabled by quantum geometry. *Nature*, 614(7948):440–444, 2 2023.

[119] Leon N. Cooper. Bound electron pairs in a degenerate fermi gas. *Physical Review*, 104(4):1189–1190, 11 1956.

[120] J. Bardeen, L. N. Cooper, and J. R. Schrieffer. Theory of superconductivity. *Physical Review*, 108(5):1175–1204, 12 1957.

[121] J. Bardeen, L. N. Cooper, and J. R. Schrieffer. Microscopic Theory of superconductivity. *Physical Review*, 106(1):162–164, 4 1957.

[122] Andreas Komnik and Michael Thorwart. BCS theory of driven superconductivity. *The European Physical Journal B*, 89(11), 11 2016.

[123] Christian Hainzl and Robert Seiringer. Critical temperature and energy gap for the BCS equation. *Physical Review B*, 77(18), 5 2008.

[124] Michael R. Norman. The challenge of unconventional superconductivity. *Science*, 332(6026):196–200, 4 2011.

[125] G. R. Stewart. Unconventional superconductivity. *Advances In Physics*, 66(2):75–196, 4 2017.

[126] Patrick A. Lee and Xiao-Gang Wen. Unusual superconducting state of underdoped cuprates. *Physical Review Letters*, 78(21):4111–4114, 5 1997.

[127] M R Norman and C Pépin. The electronic nature of high temperature cuprate superconductors. *Reports on Progress in Physics*, 66(10):1547–1610, 9 2003.

[128] P. W. Anderson. *The theory of superconductivity in the High-TC cuprates*. 2 2017.

[129] A. S. Moskvin and Yu. D. Panov. Topological structures in unconventional scenario for 2D cuprates. *Journal of Superconductivity and Novel Magnetism*, 32(1):61–84, 10 2018.

[130] C. W. Chu, L. Gao, F. Chen, Z. J. Huang, R. L. Meng, and Y. Y. Xue. Superconductivity above 150 K in HgBa2Ca2Cu3O8+δ at high pressures. *Nature*, 365(6444):323–325, 9 1993.

[131] Takao Morinari. Mechanism of unconventional superconductivity induced by skyrmion excitations in two-dimensional strongly correlated electron systems. *Physical review. B, Condensed matter*, 65(6), 1 2002.

[132] Tetsuaki Aida, Karin Matsumoto, Daisuke Ogura, Masayuki Ochi, and Kazuhiko Kuroki. Theoretical study of spin-fluctuation-mediated superconductivity in two-dimensional Hubbard models with an incipient flat band. *Physical review. B./Physical review. B*, 110(5), 8 2024.

[133] Lucile Savary and Leon Balents. Quantum spin liquids: a review. *Reports on Progress in Physics*, 80(1):016502, November 2016. Publisher: IOP Publishing.

[134] Hong-Chen Jiang. Superconductivity in the doped quantum spin liquid on the triangular lattice. *npj Quantum Materials*, 6(1), 8 2021.

[135] S. Imajo, S. Sugiura, H. Akutsu, Y. Kohama, T. Isono, T. Terashima, K. Kindo, S. Uji, and Y. Nakazawa. Extraordinary π-electron superconductivity emerging from a quantum spin liquid. *Physical Review Research*, 3(3), 7 2021.

[136] Ali H Nayfeh. *Perturbation methods*. John Wiley & Sons, 2024.

[137] Vladimir E. Korepin and Fabian H. L. Eßler. *THE ONE-DIMENSIONAL HUBBARD MODEL*. 5 1994.

[138] C. Lanczos. An iteration method for the solution of the eigenvalue problem of linear differential and integral operators. *Journal of research of the National Bureau of Standards*, 45(4):255, 10 1950.

[139] Ernest R. Davidson. The iterative calculation of a few of the lowest eigenvalues and corresponding eigenvectors of large real-symmetric matrices. *Journal of Computational Physics*, 17(1):87–94, 1 1975.

[140] Artur Baumgärtner, AN Burkitt, DM Ceperley, H De Raedt, AM Ferrenberg, DW Heermann, HJ Herrmann, DP Landau, D Levesque, W von der Linden, et al. *The Monte Carlo method in condensed matter physics*, volume 71. Springer Science & Business Media, 2012.

[141] Gaopei Pan and Zi Yang Meng. *The sign problem in quantum Monte Carlo simulations*. 3 2023.

[142] David Jeffery Griffiths. *Introduction to Quantum Mechanics*. 1 1995.

[143] G.W.F. Drake and Zong-Chao Van. Variational eigenvalues for the S states of helium. *Chemical Physics Letters*, 229(4-5):486–490, 11 1994.

[144] Steven R. White. Density matrix formulation for quantum renormalization groups. *Physical Review Letters*, 69(19):2863–2866, 11 1992.

[145] Ulrich Schollwöck. The density-matrix renormalization group in the age of matrix product states. *Annals of Physics*, 326(1):96–192, 10 2010.

[146] Richard P. Feynman. Simulating physics with computers. *International Journal of Theoretical Physics*, 21(6-7):467–488, 6 1982.

[147] Iulia Buluta and Franco Nori. Quantum simulators. *Science*, 326(5949):108–111, 10 2009.

[148] Andreas Trabesinger. Quantum simulation. *Nature Physics*, 8(4):263, 4 2012.

[149] Immanuel Bloch, Jean Dalibard, and Sylvain Nascimbène. Quantum simulations with ultracold quantum gases. *Nature Physics*, 8(4):267–276, 4 2012.

[150] Dante M. Kennes, Martin Claassen, Lede Xian, Antoine Georges, Andrew J. Millis, James Hone, Cory R. Dean, D. N. Basov, Abhay N. Pasupathy, and Angel Rubio. Moiré heterostructures as a condensed-matter quantum simulator. *Nature Physics*, 17(2):155–163, 2 2021.

[151] Moyu Chen, Fanqiang Chen, Bin Cheng, Shi Jun Liang, Feng Miao, et al. Moiré heterostructures: highly tunable platforms for quantum simulation and future computing. *J. Semicond*, 44(010301.2023), 2023.

[152] A. K. Geim and I. V. Grigorieva. Van der Waals heterostructures. *Nature*, 499(7459):419–425, 7 2013.

[153] Yuan Liu, Nathan O. Weiss, Xidong Duan, Hung-Chieh Cheng, Yu Huang, and Xiangfeng Duan. Van der Waals heterostructures and devices. *Nature Reviews Materials*, 1(9), 7 2016.

[154] K. S. Novoselov, A. Mishchenko, A. Carvalho, and A. H. Castro Neto. 2D materials and van der Waals heterostructures. *Science*, 353(6298), 7 2016.

[155] K. S. Novoselov, A. K. Geim, S. V. Morozov, D. Jiang, Y. Zhang, S. V. Dubonos, I. V. Grigorieva, and A. A. Firsov. Electric field effect in atomically thin carbon films. *Science*, 306(5696):666–669, 10 2004.

[156] A. H. Castro Neto, F. Guinea, N. M. R. Peres, K. S. Novoselov, and A. K. Geim. The electronic properties of graphene. *Reviews of Modern Physics*, 81(1):109–162, 1 2009.

[157] R. Coehoorn, C. Haas, J. Dijkstra, C. J. F. Flipse, R. A. De Groot, and A. Wold. Electronic structure ofMoSe2,MoS2, and. *Physical review. B, Condensed matter*, 35(12):6195–6202, 4 1987.

[158] Ruitao Lv, Joshua A. Robinson, Raymond E. Schaak, Du Sun, Yifan Sun, Thomas E. Mallouk, and Mauricio Terrones. Transition Metal Dichalcogenides and Beyond: Synthesis, properties, and applications of Single- and Few-Layer nanosheets. *Accounts of Chemical Research*, 48(1):56–64, 12 2014.

[159] Qing Hua Wang, Kourosh Kalantar-Zadeh, Andras Kis, Jonathan N. Coleman, and Michael S. Strano. Electronics and optoelectronics of two-dimensional transition metal dichalcogenides. *Nature Nanotechnology*, 7(11):699–712, 11 2012.

[160] Damien Voiry, Aditya Mohite, and Manish Chhowalla. Phase engineering of transition metal dichalcogenides. *Chemical Society Reviews*, 44(9):2702–2712, 2015.

[161] Sajedeh Manzeli, Dmitry Ovchinnikov, Diego Pasquier, Oleg V. Yazyev, and Andras Kis. 2D transition metal dichalcogenides. *Nature Reviews Materials*, 2(8), 6 2017.

[162] Gang Hee Han, Dinh Loc Duong, Dong Hoon Keum, Seok Joon Yun, and Young Hee Lee. van der Waals Metallic Transition Metal Dichalcogenides. *Chemical Reviews*, 118(13):6297–6336, 6 2018.

[163] Min Yi and Zhigang Shen. A review on mechanical exfoliation for the scalable production of graphene. *Journal of Materials Chemistry A*, 3(22):11700–11715, 1 2015.

[164] Enlai Gao, Shao-Zhen Lin, Zhao Qin, Markus J. Buehler, Xi-Qiao Feng, and Zhiping Xu. Mechanical exfoliation of two-dimensional materials. *Journal of the Mechanics and Physics of Solids*, 115:248–262, 3 2018.

[165] Hyun Kum, Doeon Lee, Wei Kong, Hyunseok Kim, Yongmo Park, Yunjo Kim, Yongmin Baek, Sang-Hoon Bae, Kyusang Lee, and Jeehwan Kim. Epitaxial growth and layer-transfer techniques for heterogeneous integration of materials for electronic and photonic devices. *Nature Electronics*, 2(10):439–450, 10 2019.

[166] Sanjay K. Behura, Alexis Miranda, Sasmita Nayak, Kayleigh Johnson, Priyanka Das, and Nihar R. Pradhan. Moiré physics in twisted van der Waals heterostructures of 2D materials. *Emergent Materials*, 4(4):813–826, 8 2021.

[167] Tawfiqur Rakib, Pascal Pochet, Elif Ertekin, and Harley T. Johnson. Moiré engineering in van der Waals heterostructures. *Journal of Applied Physics*, 132(12), 9 2022.

[168] Feng He, Yongjian Zhou, Zefang Ye, Sang-Hyeok Cho, Jihoon Jeong, Xiang-hai Meng, and Yaguo Wang. Moiré Patterns in 2D materials: a review. *ACS Nano*, 15(4):5944–5958, 3 2021.

[169] E. J. Mele. Commensuration and interlayer coherence in twisted bilayer graphene. *Physical Review B*, 81(16), 4 2010.

[170] J. M. B. Lopes Dos Santos, N. M. R. Peres, and A. H. Castro Neto. Graphene Bilayer with a Twist: Electronic Structure. *Physical Review Letters*, 99(25), 12 2007.

[171] J. M. B. Lopes Dos Santos, N. M. R. Peres, and A. H. Castro Neto. Continuum model of the twisted graphene bilayer. *Physical Review B*, 86(15), 10 2012.

[172] Zhiming Zhang, Yimeng Wang, Kenji Watanabe, Takashi Taniguchi, Keiji Ueno, Emanuel Tutuc, and Brian J. LeRoy. Flat bands in twisted bilayer transition metal dichalcogenides. *Nature Physics*, 16(11):1093–1096, 7 2020.

[173] Mattia Angeli and Allan H. MacDonald. Γ-valley transition metal dichalcogenide moiré bands. *Proceedings of the National Academy of Sciences*, 118(10), 3 2021.

[174] Rafi Bistritzer and Allan H. MacDonald. Moiré bands in twisted double-layer graphene. *Proceedings of the National Academy of Sciences*, 108(30):12233–12237, 7 2011.

[175] Yuan Cao, Valla Fatemi, Ahmet Demir, Shiang Fang, Spencer L. Tomarken, Jason Y. Luo, Javier D. Sanchez-Yamagishi, Kenji Watanabe, Takashi Taniguchi, Efthimios Kaxiras, Ray C. Ashoori, and Pablo Jarillo-Herrero. Correlated insulator behaviour at half-filling in magic-angle graphene superlattices. *Nature*, 556(7699):80–84, 3 2018.

[176] Yuan Cao, Daniel Rodan-Legrain, Oriol Rubies-Bigorda, Jeong Min Park, Kenji Watanabe, Takashi Taniguchi, and Pablo Jarillo-Herrero. Tunable correlated states and spin-polarized phases in twisted bilayer–bilayer graphene. *Nature*, 583(7815):215–220, 5 2020.

[177] Kevin P. Nuckolls, Myungchul Oh, Dillon Wong, Biao Lian, Kenji Watanabe, Takashi Taniguchi, B. Andrei Bernevig, and Ali Yazdani. Strongly correlated Chern insulators in magic-angle twisted bilayer graphene. *Nature*, 588(7839):610–615, 12 2020.

[178] Jianpeng Liu and Xi Dai. Theories for the correlated insulating states and quantum anomalous Hall effect phenomena in twisted bilayer graphene. *Physical review. B./Physical review. B*, 103(3), 1 2021.

[179] Myungchul Oh, Kevin P. Nuckolls, Dillon Wong, Ryan L. Lee, Xiaomeng Liu, Kenji Watanabe, Takashi Taniguchi, and Ali Yazdani. Evidence for unconventional superconductivity in twisted bilayer graphene. *Nature*, 600(7888):240–245, 10 2021.

[180] Andrew T. Pierce, Yonglong Xie, Jeong Min Park, Eslam Khalaf, Seung Hwan Lee, Yuan Cao, Daniel E. Parker, Patrick R. Forrester, Shaowen Chen, Kenji Watanabe, Takashi Taniguchi, Ashvin Vishwanath, Pablo Jarillo-Herrero, and Amir Yacoby. Unconventional sequence of correlated Chern insulators in magic-angle twisted bilayer graphene. *Nature Physics*, 17(11):1210–1215, 9 2021.

[181] Dante M. Kennes, Martin Claassen, Lede Xian, Antoine Georges, Andrew J. Millis, James Hone, Cory R. Dean, D. N. Basov, Abhay N. Pasupathy, and Angel Rubio. Moiré heterostructures as a condensed-matter quantum simulator. *Nature Physics*, 17(2):155–163, 2 2021.

[182] Guodong Yu, Zewen Wu, Zhen Zhan, Mikhail I. Katsnelson, and Shengjun Yuan. Dodecagonal bilayer graphene quasicrystal and its approximants. *npj Computational Materials*, 5(1), 12 2019.

[183] Lede Xian, Martin Claassen, Dominik Kiese, Michael M. Scherer, Simon Trebst, Dante M. Kennes, and Angel Rubio. Realization of nearly dispersionless bands with strong orbital anisotropy from destructive interference in twisted bilayer MoS2. *Nature Communications*, 12(1), 9 2021.

[184] Soumyabrata Roy, Xiang Zhang, Anand B. Puthirath, Ashokkumar Meiyazhagan, Sohini Bhattacharyya, Muhammad M. Rahman, Ganguli Babu, Sandhya Susarla, Sreehari K. Saju, Mai Kim Tran, Lucas M. Sassi, M. A. S. R. Saadi, Jiawei Lai, Onur Sahin, Seyed Mohammad Sajadi, Bhuvaneswari Dharmarajan, Devashish Salpekar, Nithya Chakingal, Abhijit Baburaj, Xinting Shuai, Aparna Adumbumkulath, Kristen A. Miller, Jessica M. Gayle, Alec Ajnsztajn, Thibeorchews Prasankumar, Vijay Vedhan Jayanthi Harikrishnan, Ved Ojha, Harikishan Kannan, Ali Zein Khater, Zhenwei Zhu, Sathvik Ajay Iyengar, Pedro Alves Da Silva Autreto, Eliezer Fernando Oliveira, Guanhui Gao, A. Glen Birdwell, Mahesh R. Neupane, Tony G. Ivanov, Jaime Taha-Tijerina, Ram Manohar Yadav, Sivaram Arepalli, Robert Vajtai, and Pulickel M. Ajayan. Structure, Properties and applications of Two-Dimensional Hexagonal Boron Nitride. *Advanced Materials*, 33(44), 9 2021.

[185] Lede Xian, Dante M. Kennes, Nicolas Tancogne-Dejean, Massimo Altarelli, and Angel Rubio. Multiflat bands and strong correlations in twisted bi-

layer boron nitride: Doping-Induced correlated insulator and superconductor. *Nano Letters*, 19(8):4934–4940, 7 2019.

[186] Lei Wang, En-Min Shih, Augusto Ghiotto, Lede Xian, Daniel A. Rhodes, Cheng Tan, Martin Claassen, Dante M. Kennes, Yusong Bai, Bumho Kim, Kenji Watanabe, Takashi Taniguchi, Xiaoyang Zhu, James Hone, Angel Rubio, Abhay N. Pasupathy, and Cory R. Dean. Correlated electronic phases in twisted bilayer transition metal dichalcogenides. *Nature Materials*, 19(8):861–866, 6 2020.

[187] Patrick Knüppel, Jiacheng Zhu, Yiyu Xia, Zhengchao Xia, Zhongdong Han, Yihang Zeng, Kenji Watanabe, Takashi Taniguchi, Jie Shan, and Kin Fai Mak. Correlated states controlled by a tunable van Hove singularity in moiré WSe2 bilayers. *Nature Communications*, 16(1), 2 2025.

[188] Nicolás Morales-Durán, Nemin Wei, Jingtian Shi, and Allan H. MacDonald. Magic angles and fractional Chern insulators in twisted homobilayer transition metal dichalcogenides. *Physical Review Letters*, 132(9), 3 2024.

[189] Yanhao Tang, Lizhong Li, Tingxin Li, Yang Xu, Song Liu, Katayun Barmak, Kenji Watanabe, Takashi Taniguchi, Allan H. MacDonald, Jie Shan, and Kin Fai Mak. Simulation of Hubbard model physics in WSe2/WS2 moiré superlattices. *Nature*, 579(7799):353–358, 3 2020.

[190] Emma C. Regan, Danqing Wang, Chenhao Jin, M. Iqbal Bakti Utama, Beini Gao, Xin Wei, Sihan Zhao, Wenyu Zhao, Zuocheng Zhang, Kentaro Yumigeta, Mark Blei, Johan D. Carlström, Kenji Watanabe, Takashi Taniguchi, Sefaattin Tongay, Michael Crommie, Alex Zettl, and Feng Wang. Mott and generalized Wigner crystal states in WSe2/WS2 moiré superlattices. *Nature*, 579(7799):359–363, 3 2020.

[191] Yang Xu, Song Liu, Daniel A. Rhodes, Kenji Watanabe, Takashi Taniguchi, James Hone, Veit Elser, Kin Fai Mak, and Jie Shan. Correlated insulating states at fractional fillings of moiré superlattices. *Nature*, 587(7833):214–218, 11 2020.

[192] Dominik Kiese, Finn Lasse Buessen, Ciarán Hickey, Simon Trebst, and Michael M. Scherer. Emergence and stability of spin-valley entangled quantum liquids in moiré heterostructures. *Physical Review Research*, 2(1), 3 2020.

[193] Johannes Motruk, Dario Rossi, Dmitry A. Abanin, and Louk Rademaker. Kagome chiral spin liquid in transition metal dichalcogenide moiré bilayers. *Physical Review Research*, 5(2), 6 2023.

[194] Bikash Padhi, R. Chitra, and Philip W. Phillips. Generalized Wigner crystallization in moiré materials. *Physical review. B./Physical review. B*, 103(12), 3 2021.

[195] Ming-Hui Chiu, Chendong Zhang, Hung-Wei Shiu, Chih-Piao Chuu, Chang-Hsiao Chen, Chih-Yuan S. Chang, Chia-Hao Chen, Mei-Yin Chou, Chih-Kang Shih, and Lain-Jong Li. Determination of band alignment in the single-layer MoS2/WSe2 heterojunction. *Nature Communications*, 6(1), 7 2015.

[196] Hui Fang, Corsin Battaglia, Carlo Carraro, Slavomir Nemsak, Burak Ozdol, Jeong Seuk Kang, Hans A. Bechtel, Sujay B. Desai, Florian Kronast, Ahmet A. Unal, Giuseppina Conti, Catherine Conlon, Gunnar K. Palsson, Michael C. Martin, Andrew M. Minor, Charles S. Fadley, Eli Yablonovitch, Roya Maboudian, and Ali Javey. Strong interlayer coupling in van der Waals heterostructures built from single-layer chalcogenides. *Proceedings of the National Academy of Sciences*, 111(17):6198–6202, 4 2014.

[197] Chenjing Quan, Chunhui Lu, Chuan He, Xiang Xu, Yuanyuan Huang, Qiyi Zhao, and Xinlong Xu. Band alignment of MOTE2/MOS2 nanocomposite films for enhanced nonlinear optical performance. *Advanced Materials Interfaces*, 6(5), 1 2019.

[198] Chenxi Zhang, Cheng Gong, Yifan Nie, Kyung-Ah Min, Chaoping Liang, Young Jun Oh, Hengji Zhang, Weihua Wang, Suklyun Hong, Luigi Colombo, Robert M Wallace, and Kyeongjae Cho. Systematic study of electronic structure and band alignment of monolayer transition metal dichalcogenides in Van der Waals heterostructures. *2D Materials*, 4(1):015026, 11 2016.

[199] Yang Zhang, Tongtong Liu, and Liang Fu. Electronic structures, charge transfer, and charge order in twisted transition metal dichalcogenide bilayers. *Physical review. B./Physical review. B*, 103(15), 4 2021.

[200] Pasqual Rivera, John R. Schaibley, Aaron M. Jones, Jason S. Ross, Sanfeng Wu, Grant Aivazian, Philip Klement, Kyle Seyler, Genevieve Clark, Nirmal J. Ghimire, Jiaqiang Yan, D. G. Mandrus, Wang Yao, and Xiaodong Xu. Observation of long-lived interlayer excitons in monolayer MoSe2–WSe2 heterostructures. *Nature Communications*, 6(1), 2 2015.

[201] Bastian Miller, Alexander Steinhoff, Borja Pano, Julian Klein, Frank Jahnke, Alexander Holleitner, and Ursula Wurstbauer. Long-Lived Direct and Indirect Interlayer Excitons in van der Waals Heterostructures. *Nano Letters*, 17(9):5229–5237, 7 2017.

[202] Yuya Shimazaki, Ido Schwartz, Kenji Watanabe, Takashi Taniguchi, Martin Kroner, and Ataç Imamoğlu. Strongly correlated electrons and hybrid excitons in a moiré heterostructure. *Nature*, 580(7804):472–477, 4 2020.

[203] Haining Pan, Fengcheng Wu, and Sankar Das Sarma. Band topology, Hubbard model, Heisenberg model, and Dzyaloshinskii-Moriya interaction in twisted bilayer WSe2. *Physical Review Research*, 2(3), 7 2020.

[204] Chenhao Jin, Zui Tao, Tingxin Li, Yang Xu, Yanhao Tang, Jiacheng Zhu, Song Liu, Kenji Watanabe, Takashi Taniguchi, James C. Hone, Liang Fu, Jie Shan, and Kin Fai Mak. Stripe phases in WSe2/WS2 moiré superlattices. *Nature Materials*, 20(7):940–944, 3 2021.

[205] Qiao Li, Bin Cheng, Moyu Chen, Bo Xie, Yongqin Xie, Pengfei Wang, Fanqiang Chen, Zenglin Liu, Kenji Watanabe, Takashi Taniguchi, Shi-Jun Liang, Da Wang, Chenjie Wang, Qiang-Hua Wang, Jianpeng Liu, and Feng Miao. Tunable quantum criticalities in an isospin extended Hubbard model simulator. *Nature*, 609(7927):479–484, 9 2022.

[206] Hongyuan Li, Shaowei Li, Mit H. Naik, Jingxu Xie, Xinyu Li, Emma Regan, Danqing Wang, Wenyu Zhao, Kentaro Yumigeta, Mark Blei, Takashi Taniguchi, Kenji Watanabe, Sefaattin Tongay, Alex Zettl, Steven G. Louie, Michael F. Crommie, and Feng Wang. Imaging local discharge cascades for correlated electrons in WS2/WSe2 moiré superlattices. *Nature Physics*, 17(10):1114–1119, 8 2021.

[207] You Zhou, Jiho Sung, Elise Brutschea, Ilya Esterlis, Yao Wang, Giovanni Scuri, Ryan J. Gelly, Hoseok Heo, Takashi Taniguchi, Kenji Watanabe, Gergely Zaránd, Mikhail D. Lukin, Philip Kim, Eugene Demler, and Hongkun Park. Bilayer Wigner crystals in a transition metal dichalcogenide heterostructure. *Nature*, 595(7865):48–52, 6 2021.

[208] Hongzhen Zhong, Zhixin Su, and Jun Kang. Trilayer Moiré superlattices of MOS2 as a simulator for the ionic Hubbard model on Honeycomb lattice. *Advanced Functional Materials*, 34(11), 12 2023.

[209] Qiang Wan, Chunlong Wu, Xun-Jiang Luo, Shenghao Dai, Cao Peng, Renzhe Li, Shangkun Mo, Keming Zhao, Wen-Xuan Qiu, Hao Zhong, Yiwei Li, Chendong Zhang, Fengcheng Wu, and Nan Xu. Quantum simulation of a honeycomb lattice model by high-order moiré pattern. *Physical review. B./Physical review. B*, 109(16), 4 2024.

[210] D. M. Kennes, L. Xian, M. Claassen, and A. Rubio. One-dimensional flat bands in twisted bilayer germanium selenide. *Nature Communications*, 11(1), 2 2020.

[211] Manato Fujimoto and Toshikaze Kariyado. Effective continuum model of twisted bilayer GeSe and origin of the emerging one-dimensional mode. *Physical review. B./Physical review. B*, 104(12), 9 2021.

[212] Ma Luo. Topological edge states of a graphene zigzag nanoribbon with spontaneous edge magnetism. *Physical review. B./Physical review. B*, 102(7), 8 2020.

[213] Jens Brede, Nestor Merino-Díez, Alejandro Berdonces-Layunta, Sofía Sanz, Amelia Domínguez-Celorrio, Jorge Lobo-Checa, Manuel Vilas-Varela, Diego Peña, Thomas Frederiksen, José I. Pascual, Dimas G. De Oteyza, and David Serrate. Detecting the spin-polarization of edge states in graphene nanoribbons. *Nature Communications*, 14(1), 10 2023.

[214] Thomas G. Pedersen, Christian Flindt, Jesper Pedersen, Niels Asger Mortensen, Antti-Pekka Jauho, and Kjeld Pedersen. Graphene Antidot lattices: designed defects and spin qubits. *Physical Review Letters*, 100(13), 4 2008.

[215] Alev Devrim Güçlü, Pawel Potasz, Marek Korkusinski, and Pawel Hawrylak. *Graphene Quantum dots*. 1 2014.

[216] P. Potasz, A. D. Güçlü, and P. Hawrylak. Zero-energy states in triangular and trapezoidal graphene structures. *Physical Review B*, 81(3), 1 2010.

[217] Elliott H. Lieb. Two theorems on the Hubbard model. *Physical Review Letters*, 62(10):1201–1204, 3 1989.

[218] J. Fernández-Rossier and J. J. Palacios. Magnetism in graphene nanoislands. *Physical Review Letters*, 99(17), 10 2007.

[219] A. D. Güçlü, P. Potasz, O. Voznyy, M. Korkusinski, and P. Hawrylak. Magnetism and correlations in fractionally filled degenerate shells of graphene quantum dots. *Physical Review Letters*, 103(24), 12 2009.

[220] P. Tian, L. Tang, K.S. Teng, and S.P. Lau. Graphene quantum dots from chemistry to applications. *Materials Today Chemistry*, 10:221–258, 11 2018.

[221] Linlin Shi, Boyang Wang, and Siyu Lu. Efficient bottom-up synthesis of graphene quantum dots at an atomically precise level. *Matter*, 6(3):728–760, 1 2023.

[222] Chenxiao Zhao, Lin Yang, João C. G. Henriques, Mar Ferri-Cortés, Gonçalo Catarina, Carlo A. Pignedoli, Ji Ma, Xinliang Feng, Pascal Ruffieux, Joaquín Fernández-Rossier, and Roman Fasel. Spin excitations in nanographene-based antiferromagnetic spin-1/2 Heisenberg chains. *Nature Materials*, 3 2025.

[223] Qingrui Dong, Jiaqi Lou, Wenjun Xu, and Chunxiang Liu. Coherent spin manipulation in triangulene by a tip-induced electric field. *Physical review. B./Physical review. B*, 111(16), 4 2025.

[224] Saoirsé E. Freeney, Marlou R. Slot, Thomas S. Gardenier, Ingmar Swart, and Daniel Vanmaekelbergh. Electronic Quantum Materials Simulated with Artificial Model Lattices. *ACS Nanoscience Au*, 2(3):198–224, 2 2022.

[225] D. M. Eigler and E. K. Schweizer. Positioning single atoms with a scanning tunnelling microscope. *Nature*, 344(6266):524–526, 4 1990.

[226] Robert Drost, Teemu Ojanen, Ari Harju, and Peter Liljeroth. Topological states in engineered atomic lattices. *Nature Physics*, 13(7):668–671, 3 2017.

[227] Marlou R. Slot, Thomas S. Gardenier, Peter H. Jacobse, Guido C. P. Van Miert, Sander N. Kempkes, Stephan J. M. Zevenhuizen, Cristiane Morais Smith, Daniel Vanmaekelbergh, and Ingmar Swart. Experimental realization and characterization of an electronic Lieb lattice. *Nature Physics*, 13(7):672–676, 4 2017.

[228] Thomas S. Gardenier, Jette J. Van Den Broeke, Jesper R. Moes, Ingmar Swart, Christophe Delerue, Marlou R. Slot, C. Morais Smith, and Daniel Vanmaekelbergh. p Orbital Flat Band and Dirac Cone in the Electronic Honeycomb Lattice. *ACS Nano*, 14(10):13638–13644, 9 2020.

[229] Laura C. Collins, Thomas G. Witte, Rochelle Silverman, David B. Green, and Kenjiro K. Gomes. Imaging quasiperiodic electronic states in a synthetic Penrose tiling. *Nature Communications*, 8(1), 6 2017.

[230] S. N. Kempkes, M. R. Slot, S. E. Freeney, S. J. M. Zevenhuizen, D. Vanmaekelbergh, I. Swart, and C. Morais Smith. Design and characterization of electrons in a fractal geometry. *Nature Physics*, 15(2):127–131, 10 2018.

[231] Linghao Yan and Peter Liljeroth. Engineered electronic states in atomically precise artificial lattices and graphene nanoribbons. *Advances in Physics X*, 4(1):1651672, 1 2019.

[232] M. F. Crommie, C. P. Lutz, and D. M. Eigler. Confinement of electrons to quantum corrals on a metal surface. *Science*, 262(5131):218–220, 10 1993.

[233] A. Eiguren, B. Hellsing, F. Reinert, G. Nicolay, E. V. Chulkov, V. M. Silkin, S. Hüfner, and P. M. Echenique. Role of bulk and surface phonons in the decay of metal surface states. *Physical Review Letters*, 88(6), 1 2002.

[234] Kenjiro K. Gomes, Warren Mar, Wonhee Ko, Francisco Guinea, and Hari C. Manoharan. Designer Dirac fermions and topological phases in molecular graphene. *Nature*, 483(7389):306–310, 3 2012.

[235] Conan Weeks, Jun Hu, Jason Alicea, Marcel Franz, and Ruqian Wu. Engineering a robust quantum spin hall state in graphene via Adatom deposition. *Physical Review X*, 1(2), 10 2011.

[236] N. B. Kopnin and A. S. Melnikov. Proximity-induced superconductivity in two-dimensional electronic systems. *Physical Review B*, 84(6), 8 2011.

[237] Wenqing Dai, Anthony Richardella, Renzhong Du, Weiwei Zhao, Xin Liu, C. X. Liu, Song-Hsun Huang, Raman Sankar, Fangcheng Chou, Nitin Samarth, and Qi Li. Proximity-effect-induced superconducting gap in topological surface states – A point contact spectroscopy study of NBSE2/BI2SE3 Superconductor-Topological insulator heterostructures. *Scientific Reports*, 7(1), 8 2017.

[238] H.Q. Lin, J.E. Gubernatis, Harvey Gould, and Jan Tobochnik. Exact diagonalization methods for quantum systems. *Computers in Physics*, 7(4):400–407, 7 1993.

[239] Jürgen Schnack. *Exact diagonalization techniques for quantum spin systems.* 1 2023.

[240] H. Fehske, R. Schneider, and A. Weiße. *Computational Many-Particle Physics.* 12 2007.

[241] Jung-Hoon Jung and Jae Dong Noh. Guide to Exact Diagonalization Study of Quantum Thermalization. *Journal of the Korean Physical Society*, 76(8):670–683, 4 2020.

[242] Eva Pavarini, Piers Coleman, and Erik Koch. Many-Body Physics: From Kondo to Hubbard, 2015.

[243] Leo P. Kadanoff. Scaling laws for ising models near Tc. *Physics Physique Fizika*, 2(6):263–272, 6 1966.

[244] Kenneth G. Wilson. Renormalization Group and Critical phenomena. i. Renormalization Group and the Kadanoff Scaling Picture. *Physical review. B, Solid state*, 4(9):3174–3183, 11 1971.

[245] Nigel Goldenfeld. *Lectures on phase transitions and the Renormalization Group*. Addison-Wesley Longman, 8 1992.

[246] U. Schollwöck. The density-matrix renormalization group. *Reviews of Modern Physics*, 77(1):259–315, 4 2005.

[247] Johannes Hauschild and Frank Pollmann. Efficient numerical simulations with Tensor Networks: Tensor Network Python (TeNPy). *SciPost Physics Lecture Notes*, 10 2018.

[248] M Fannes, B Nachtergaele, and R. F Werner. Exact antiferromagnetic ground states of quantum spin chains. *EPL (Europhysics Letters)*, 10(7):633–637, 12 1989.

[249] J. Ignacio Cirac, David Pérez-García, Norbert Schuch, and Frank Verstraete. Matrix product states and projected entangled pair states: Concepts, symmetries, theorems. *Reviews of Modern Physics*, 93(4), 12 2021.

[250] Hal Tasaki. *Physics and Mathematics of Quantum Many-Body Systems*. 1 2020.

[251] A J Daley, C Kollath, U Schollwöck, and G Vidal. Time-dependent density-matrix renormalization-group using adaptive effective Hilbert spaces. *Journal of Statistical Mechanics Theory and Experiment*, 2004(04):P04005, 4 2004.

[252] Xiqiao Wang, Ehsan Khatami, Fan Fei, Jonathan Wyrick, Pradeep Namboodiri, Ranjit Kashid, Albert F Rigosi, Garnett Bryant, and Richard Silver. Experimental realization of an extended Fermi-Hubbard model using a 2D lattice of dopant-based quantum dots. *Nature Communications*, 13(1), 11 2022.

[253] Tim Byrnes, Na Young Kim, Kenichiro Kusudo, and Yoshihisa Yamamoto. Quantum simulation of Fermi-Hubbard models in semiconductor quantum-dot arrays. *Physical Review B*, 78(7), 8 2008.

[254] Pierre-Luc Dallaire-Demers and Frank K. Wilhelm. Quantum gates and architecture for the quantum simulation of the Fermi-Hubbard model. *Physical review. A/Physical review, A*, 94(6), 12 2016.

[255] J. Salfi, J. A. Mol, R. Rahman, G. Klimeck, M. Y. Simmons, L. C. L. Hollenberg, and S. Rogge. Quantum simulation of the Hubbard model with dopant atoms in silicon. *Nature Communications*, 7(1), 4 2016.

[256] Nicolás Morales-Durán, Nai Chao Hu, Pawel Potasz, and Allan H. MacDonald. Nonlocal interactions in Moiré Hubbard systems. *Physical Review Letters*, 128(21), 5 2022.

[257] Kevin Slagle and Liang Fu. Charge transfer excitations, pair density waves, and superconductivity in moiré materials. *Physical review. B./Physical review. B*, 102(23), 12 2020.

[258] V Vitale, K Atalar, A A Mostofi, and J Lischner. Flat band properties of twisted transition metal dichalcogenide homo- and heterobilayers of MoS2, MoSe2, WS2 and WSe2. *2D Materials*, 8(4):045010, 7 2021.

[259] Fengcheng Wu, Timothy Lovorn, Emanuel Tutuc, and A. H. MacDonald. Hubbard Model Physics in Transition Metal Dichalcogenide Moiré Bands. *Physical Review Letters*, 121(2), 7 2018.

[260] Nai Chao Hu and Allan H. MacDonald. Competing magnetic states in transition metal dichalcogenide moiré materials. *Physical review. B./Physical review. B*, 104(21), 12 2021.

[261] Nicolás Morales-Durán, Allan H. MacDonald, and Pawel Potasz. Metal-insulator transition in transition metal dichalcogenide heterobilayer moiré superlattices. *Physical review. B./Physical review. B*, 103(24), 6 2021.

[262] Jacques Des Cloizeaux. Energy bands and projection operators in a crystal: analytic and asymptotic properties. *Physical Review*, 135(3A):A685–A697, 8 1964.

[263] Nicola Marzari and David Vanderbilt. Maximally localized generalized Wannier functions for composite energy bands. *Physical review. B, Condensed matter*, 56(20):12847–12865, 11 1997.

[264] Andreas V Stier, Nathan P Wilson, Genevieve Clark, Xiaodong Xu, and Scott A Crooker. Probing the influence of dielectric environment on excitons in monolayer wse2: insight from high magnetic fields. *Nano letters*, 16(11):7054–7060, 2016.

[265] Yosuke Nagaoka. Ferromagnetism in a narrow, almost Half-FilledsBand. *Physical Review*, 147(1):392–405, 7 1966.

[266] Hal Tasaki. Extension of Nagaoka's theorem on the large-UHubbard model. *Physical review. B, Condensed matter*, 40(13):9192–9193, 11 1989.

[267] H. Tasaki. From Nagaoka's Ferromagnetism to Flat-Band Ferromagnetism and Beyond: An Introduction to Ferromagnetism in the Hubbard model. *Progress of Theoretical Physics*, 99(4):489–548, 4 1998.

[268] Hong-Yu Yang, Andreas M. Läuchli, Frédéric Mila, and Kai Phillip Schmidt. Effective spin model for the spin-liquid phase of the hubbard model on the triangular lattice. *Phys. Rev. Lett.*, 105:267204, 2010.

[269] Johannes Hauschild and Frank Pollmann. Efficient numerical simulations with Tensor Networks: Tensor Network Python (TeNPy). *SciPost Phys. Lect. Notes*, page 5, 2018.

[270] P.W. Anderson. Resonating valence bonds: A new kind of insulator? *Materials Research Bulletin*, 8(2):153–160, 2 1973.

[271] Assa Auerbach. *Interacting electrons and quantum magnetism*. 1 1994.

[272] N. Read and Subir Sachdev. Valence-bond and spin-Peierls ground states of low-dimensional quantum antiferromagnets. *Physical Review Letters*, 62(14):1694–1697, 4 1989.

[273] T. Senthil, Ashvin Vishwanath, Leon Balents, Subir Sachdev, and Matthew P. A. Fisher. Deconfined quantum critical points. *Science*, 303(5663):1490–1494, 3 2004.

[274] T. Senthil, Leon Balents, Subir Sachdev, Ashvin Vishwanath, and Matthew P. A. Fisher. Quantum criticality beyond the Landau-Ginzburg-Wilson paradigm. *Physical Review B*, 70(14), 10 2004.

[275] Subir Sachdev. *Quantum Phase Transitions*. 4 2011.

[276] Chong Wang, Adam Nahum, Max A. Metlitski, Cenke Xu, and T. Senthil. Deconfined Quantum Critical Points: Symmetries and Dualities. *Physical Review X*, 7(3):031051, September 2017.

[277] Kevin Slagle and Cenke Xu. Quantum phase transition between theZ2spin liquid and valence bond crystals on a triangular lattice. *Physical Review B*, 89(10), 3 2014.

[278] P. Fazekas and P. W. Anderson. On the ground state properties of the anisotropic triangular antiferromagnet. *Philosophical magazine*, 30(2):423–440, 8 1974.

[279] J. Richter. Resonating valence bond states in square lattice antiferromagnets with disorder and frustration. *Physics Letters A*, 140(1-2):81–83, 9 1989.

[280] J. Richter. Resonating valence bond states in doped square-lattice antiferromagnets: finite cluster calculations. *Zeitschrift für Physik B Condensed Matter*, 79(3):403–408, 10 1990.

[281] S. R. White, R. M. Noack, and D. J. Scalapino. Resonating Valence Bond Theory of coupled Heisenberg chains. *Physical Review Letters*, 73(6):886–889, 8 1994.

[282] N Flocke. Fully variational resonance-valence-bond results on two-, three- and four-legged spin-1/2 Heisenberg ladders. *Journal of Physics Condensed Matter*, 11(36):6945–6957, 8 1999.

[283] D. J. Klein, T. G. Schmalz, M. A. Garcriaaa-Bach, R. Valenti, and T. P. Živković. Resonating-valence-bond theory for the square-planar lattice. *Physical review. B, Condensed matter*, 43(1):719–722, 1 1991.

[284] P. W. Anderson. The resonating Valence Bond State in LA 2 CUO 4 and superconductivity. *Science*, 235(4793):1196–1198, 3 1987.

[285] Xiao-Gang Wen. Quantum orders and symmetric spin liquids. *Physical Review B*, 65(16):165113, April 2002. Publisher: American Physical Society.

[286] Bin-Bin Chen, Ziyu Chen, Shou-Shu Gong, D. N. Sheng, Wei Li, and Andreas Weichselbaum. Quantum Spin Liquid with Emergent Chiral Order in the Triangular-lattice Hubbard Model. *Physical Review B*, 106(9):094420, September 2022. arXiv:2102.05560 [cond-mat].

[287] Yuan-Ming Lu. Symmetric Z 2 spin liquids and their neighboring phases on triangular lattice. *Physical Review B*, 93(16):165113, April 2016.

[288] Wen-Yu He. Spinon Fermi Surface in a Cluster Mott Insulator Model on a Triangular Lattice. *Physical Review Letters*, 121(4), 2018.

[289] Yao Shen, Yao-Dong Li, Hongliang Wo, Yuesheng Li, Shoudong Shen, Bingying Pan, Qisi Wang, H. C. Walker, P. Steffens, M. Boehm, Yiqing Hao, D. L. Quintero-Castro, L. W. Harriger, M. D. Frontzek, Lijie Hao, Siqin Meng, Qingming Zhang, Gang Chen, and Jun Zhao. Evidence for a spinon Fermi surface in a triangular-lattice quantum-spin-liquid candidate. *Nature*, 540(7634):559–562, December 2016. Publisher: Nature Publishing Group.

[290] Michael Pretko and T. Senthil. Entanglement entropy of U(1) quantum spin liquids. *Physical review. B./Physical review. B*, 94(12), 9 2016.

[291] Wen-Yuan Liu, Shaojun Dong, Chao Wang, Yongjian Han, Hong An, Guang-Can Guo, and Lixin He. Gapless spin liquid ground state of the spin-1/2 j1 - j2 heisenberg model on square lattices. *Physical Review B*, 98(24):241109, December 2018.

[292] Tomonori Shirakawa, Takami Tohyama, Jure Kokalj, Sigetoshi Sota, and Seiji Yunoki. Ground-state phase diagram of the triangular lattice Hubbard model by the density-matrix renormalization group method. *Physical Review B*, 96(20):205130, November 2017. Publisher: American Physical Society.

[293] Ta Tang, Brian Moritz, and Thomas P. Devereaux. Spectra of a gapped quantum spin liquid with a strong chiral excitation on the triangular lattice. *Physical Review B*, 106(6):064428, August 2022. Publisher: American Physical Society.

[294] Simeng Yan, David A. Huse, and Steven R. White. Spin-Liquid ground state of the S = 1/2 Kagome Heisenberg Antiferromagnet. *Science*, 332(6034):1173–1176, 4 2011.

[295] Wen-Yuan Liu, Juraj Hasik, Shou-Shu Gong, Didier Poilblanc, Wei-Qiang Chen, and Zheng-Cheng Gu. Emergence of Gapless Quantum Spin Liquid from Deconfined Quantum Critical Point. *Physical Review X*, 12(3), 9 2022.

[296] Yunchao Zhang, Xue-Yang Song, and Todadri Senthil. Dirac spin liquid as an "unnecessary" quantum critical point on square lattice antiferromagnets. *SciPost Physics Core*, 8(1), 2 2025.

[297] Tarun Grover, N. Trivedi, T. Senthil, and Patrick A. Lee. Weak Mott insulators on the triangular lattice: Possibility of a gapless nematic quantum spin liquid. *Physical Review B*, 81(24), 6 2010.

[298] Shou-Shu Gong, W. Zhu, D. N. Sheng, and Kun Yang. Possible nematic spin liquid in spin-1 antiferromagnetic system on the square lattice: Implications for the nematic paramagnetic state of FeSe. *Physical review. B./Physical review. B*, 95(20), 5 2017.

[299] Wen-Jun Hu, Shou-Shu Gong, Hsin-Hua Lai, Haoyu Hu, Qimiao Si, and Andriy H. Nevidomskyy. Nematic spin liquid phase in a frustrated spin-1 system on the square lattice. *Physical review. B./Physical review. B*, 100(16), 10 2019.

[300] Chenhao Jin, Zui Tao, Tingxin Li, Yang Xu, Yanhao Tang, Jiacheng Zhu, Song Liu, Kenji Watanabe, Takashi Taniguchi, James C. Hone, Liang Fu, Jie

Shan, and Kin Fai Mak. Stripe phases in WSe2/WS2 moiré superlattices. *Nature Materials*, 20(7):940–944, 3 2021.

[301] None Pasquale Calabrese and None John Cardy. Entanglement entropy and quantum field theory. *Journal of Statistical Mechanics Theory and Experiment*, 2004(06):P06002, 6 2004.

[302] Wen-Yu He, Xiao Yan Xu, Gang Chen, K. T. Law, and Patrick A. Lee. Spinon fermi surface in a cluster mott insulator model on a triangular lattice and possible application to 1T−TAS2. *Physical Review Letters*, 121(4), 7 2018.

[303] Brian Swingle. Entanglement entropy and the fermi surface. *Physical Review Letters*, 105(5), 7 2010.

[304] Jasimuddin Ahmed and Swadhin K. Mandal. Phenalenyl radical: smallest polycyclic odd alternant hydrocarbon present in the graphene sheet. *Chemical Reviews*, 122(13):11369–11431, 5 2022.

[305] Niko Pavliček, Anish Mistry, Zsolt Majzik, Nikolaj Moll, Gerhard Meyer, David J. Fox, and Leo Gross. Synthesis and characterization of triangulene. *Nature Nanotechnology*, 12(4):308–311, 2 2017.

[306] Elia Turco, Annika Bernhardt, Nils Krane, Leoš Valenta, Roman Fasel, Michal Juríček, and Pascal Ruffieux. Observation of the magnetic ground state of the two smallest triangular nanographenes. *JACS Au*, 3(5):1358–1364, 3 2023.

[307] N. Krane, E. Turco, A. Bernhardt, D. Jacob, G. Gandus, D. Passerone, M. Luisier, M. Juríček, R. Fasel, J. Fernández-Rossier, and P. Ruffieux. Exchange interactions and intermolecular hybridization in a spin-1/2 nanographene dimer. *Nano Letters*, 23(20):9353–9359, 10 2023.

[308] Chenxiao Zhao, Gonçalo Catarina, Jin-Jiang Zhang, João C. G. Henriques, Lin Yang, Ji Ma, Xinliang Feng, Oliver Gröning, Pascal Ruffieux, Joaquín Fernández-Rossier, and Roman Fasel. Tunable topological phases in nanographene-based spin-1/2 alternating-exchange Heisenberg chains. *Nature Nanotechnology*, 10 2024.

[309] J. C. G. Henriques and J. Fernández-Rossier. Anatomy of linear and nonlinear intermolecular exchange in S=1 nanographene. *Physical review. B./Physical review. B*, 108(15), 10 2023.

[310] Shantanu Mishra, Gonçalo Catarina, Fupeng Wu, Ricardo Ortiz, David Jacob, Kristjan Eimre, Ji Ma, Carlo A. Pignedoli, Xinliang Feng, Pascal Ruffieux, Joaquín Fernández-Rossier, and Roman Fasel. Observation of fractional edge excitations in nanographene spin chains. *Nature*, 598(7880):287–292, 10 2021.

[311] P. Potasz, A. D. Güçlü, A. Wójs, and P. Hawrylak. Electronic properties of gated triangular graphene quantum dots: Magnetism, correlations, and geometrical effects. *Physical Review B*, 85(7), 2 2012.

[312] Yasser Saleem, Amintor Dusko, Moritz Cygorek, Marek Korkusinski, and Pawel Hawrylak. Quantum simulator of extended bipartite hubbard model with broken sublattice symmetry: Magnetism, correlations, and phase transitions. *Phys. Rev. B*, 105:205105, May 2022.

[313] Shantanu Mishra, Gonçalo Catarina, Fupeng Wu, Ricardo Ortiz, David Jacob, Kristjan Eimre, Ji Ma, Carlo A. Pignedoli, Xinliang Feng, Pascal Ruffieux, Joaquín Fernández-Rossier, and Roman Fasel. Observation of fractional edge excitations in nanographene spin chains. *Nature*, 598(7880):287–292, 10 2021.

[314] J. C. G. Henriques and J. Fernández-Rossier. Anatomy of linear and nonlinear intermolecular exchange in $s = 1$ nanographene. *Phys. Rev. B*, 108:155423, Oct 2023.

[315] Motohiko Ezawa. Coulomb blockade in graphene nanodisks. *Physical Review B*, 77(15), 4 2008.

[316] E. Polizzi, F. Mila, and E. S. Sørensen. $s = \frac{1}{2}$ chain-boundary excitations in the haldane phase of one-dimensional $s = 1$ systems. *Phys. Rev. B*, 58:2407–2410, Aug 1998.

[317] Marcel Den Nijs and Koos Rommelse. Preroughening transitions in crystal surfaces and valence-bond phases in quantum spin chains. *Physical review. B, Condensed matter*, 40(7):4709–4734, 9 1989.

[318] Patrick Fazekas. *Lecture notes on Electron correlation and Magnetism*. 1 1999.

[319] Attila Szabo and Neil S. Ostlund. *Modern Quantum Chemistry*. Courier Corporation, 7 1996.

[320] C. David Sherrill and Henry F. Schaefer. *The configuration interaction method: advances in highly correlated approaches*. 1 1999.

[321] Stefano Battaglia, Max Rossmannek, Vladimir V. Rybkin, Ivano Tavernelli, and Jürg Hutter. A general framework for active space embedding methods with applications in quantum computing. *npj Computational Materials*, 10(1), 12 2024.